

Aus dem
Deutschen Herzzentrum Berlin
Klinik für Herz-, Thorax- und Gefäßchirurgie
Direktor: Prof. Dr. med. Volkmar Falk

Habilitationsschrift

Verwendung konventioneller bildgebender Verfahren zur patientenspezifischen Therapieplanung und Therapiesimulation bei der Behandlung von Erkrankungen der Mitralklappe und der Aortenklappe

zur Erlangung der Lehrbefähigung
für das Fach Herzchirurgie

vorgelegt dem Fakultätsrat der Medizinischen Fakultät
Charité – Universitätsmedizin Berlin
von

Dr. med. Simon H. Sündermann

Eingereicht: **Juli 2016**
Dekan: **Prof. Dr. med. Axel R. Pries**
1. Gutachter: **Prof. Dr. med. Raffaele De Simone** (Heidelberg)
2. Gutachter: **Prof. Dr. med. Holger Thiele** (Lübeck)

Inhaltsverzeichnis

Abkürzungsverzeichnis.....	3
1 Einleitung.....	4
1.1 Aortenklappenstenose und Mitralklappeninsuffizienz und Therapieformen	4
1.2 Computertomographie der Aortenklappe und Mitralklappe	5
1.3 Echokardiographie der Aortenklappe und Mitralklappe	7
1.4 Fusion bildgebender Verfahren.....	8
1.5 Patientenspezifische Therapieplanung und Simulation von Eingriffen an der Aorten- und der Mitralklappe.....	8
2 Eigene Arbeiten	10
2.1 Implantation individualisierter Mitralklappen-Annuloplastieringe im Tiermodell.....	10
2.2 Computertomographie zur Planung der Implantation eines kathetergestützten Mitralklappen- Annuloplastie-Bandes. Anwendungsstudie im Tiermodell.....	17
2.3 Simulation der Implantation von Transkatheter-Aortenklappenprothesen in CT-basierte Modelle der Aortenwurzel.....	26
2.4 Verwendung von Stent Maps zur Vorhersage von Komplikationen bei Transkatheter- Aortenklappenimplantationen	36
2.5 Bildgestützte mechanische Analyse der Deformation von Transkatheter-Aortenklappenprothesen- Stents.....	47
2.6 Fusion von echokardiographischen und fluoroskopischen Bildern während MitraClip- Interventionen	60
2.7 Zweidimensionale und dreidimensionale transösophageale Echokardiographie im Großtiermodell	68
3 Diskussion	76
3.1 Verwendung von CT-Bilddaten zur Simulation von kathetergestützten Aortenklappenimplantationen	79
3.2 Verwendung der transösophagealen Echokardiographie bei bildfusionierenden Techniken und zur Entwicklung neuer, patientenspezifischer Therapieverfahren	83
4 Zusammenfassung.....	86
5 Literatur.....	88
6 Danksagung	96
7 Erklärung.....	97

Abkürzungsverzeichnis

AQUA	Angewandte Qualitätsförderung und Forschung im Gesundheitswesen
CT	Computertomographie
FEM	Finite-Elemente-Methode
ICE	<i>Intracardial Echocardiography</i> = Intrakardiale Echokardiographie
MSCT	Multi-Slice Computertomographie
TEE	Transösophageale Echokardiographie
TAVI	<i>Transcatheter Aortic Valve Implantation</i> = Transkatheter-Aortenklappenimplantation
TMVI	<i>Transcatheter Mitral Valve Implantation</i> = Transkatheter-Mitralklappenimplantation

1 Einleitung

1.1 Aortenklappenstenose und Mitralklappeninsuffizienz und Therapieformen

Die Aortenklappenstenose und die Mitralklappeninsuffizienz sind die beiden häufigsten Herzklappenerkrankungen bei erwachsenen Patienten in westlichen Industrienationen. Die kalzifizierte Aortenklappenstenose weist in Europa und Nordamerika eine Prävalenz von 2–7% je nach Altersgruppe auf. Mit zunehmendem Alter steigt die Prävalenz deutlich an^{1,2}. Die Mitralklappeninsuffizienz folgt in der Häufigkeit mit einer jährlichen Inzidenz von ca. 2–3%³. Aufgrund der hohen Prävalenz und Inzidenz der Klappenvitien gehört die operative und zunehmend auch kathetergestützte Versorgung (Transkatheter-Aortenklappenimplantation, TAVI) zu den häufigsten Eingriffen nach der Bypass-Operation in der Herzchirurgie. Nach Angaben des AQUA-Instituts wurden im Jahr 2014 in Deutschland 23 217 Aortenklappenprothesen implantiert, 9 953 konventionell chirurgisch und 13 264 kathetergestützt. Im Jahr 2013 wurden erstmalig geringfügig mehr Aortenklappenprothesen kathetergestützt implantiert als konventionell chirurgisch. Die Fortsetzung des Trends im Jahr 2014 zeigt die Entwicklung hin zum Anstieg weniger invasiver Therapieformen. Aktuell sind die kathetergestützten Verfahren noch Hochrisikopatienten vorbehalten, da bisher Langzeitergebnisse fehlen⁴. Erste Studien zeigen ähnliche Ergebnisse für TAVI und den chirurgischen Aortenklappenersatz nach 5 Jahren bezogen auf die Mortalität⁵. Ebenso wurden erste Studien bei Patienten mit mittlerem Operationsrisiko durchgeführt. Auch hier zeigen sich ähnliche Ergebnisse bei beiden Verfahren⁶. Obwohl Langzeitergebnisse für diese Patientengruppe fehlen ist ein Anstieg des Einsatzes dieser Methoden zu erwarten. Auch für den chirurgischen Aortenklappenersatz sind minimalinvasive Therapieformen etabliert worden. Die Implantation einer Aortenklappenprothese kann über eine obere Hemisternotomie oder eine rechtslaterale Minithorakotomie erfolgen. Bei beiden Verfahren wird auf die Durchführung einer vollständigen medianen Sternotomie verzichtet. Der Einsatz der Herz-Lungen-Maschine ist allerdings trotzdem nötig.

Zur Behandlung der Mitralklappeninsuffizienz stehen ebenfalls verschiedene Therapieformen zur Verfügung. Der Goldstandard mit exzellenten Langzeitergebnissen ist nach wie vor die chirurgische Rekonstruktion der Klappe⁷. Nach Angaben des AQUA-Instituts wurden 2014 insgesamt 5 913 isolierte Mitralklappenoperationen durchgeführt. Bei 3 887 Patienten gelang die Rekonstruktion der Klappe. An vielen Zentren ist der minimalinvasive Zugang zur Mitralklappe über eine rechtslaterale Minithorakotomie der Goldstandard. Auch für dieses Verfahren sind

exzellente Ergebnisse beschrieben⁸. Ein interventionelles Verfahren zur Behandlung der Mitralklappeninsuffizienz bei Hochrisikopatienten, bei denen möglichst auf den Einsatz der Herz-Lungen-Maschine verzichtet werden sollte, ist die Implantation des sogenannten MitraClip. Bei diesem Eingriff werden kathetergestützt das vordere und hintere Mitalsegel aneinandergeheftet und somit die Undichtigkeit der Klappe reduziert. Das Verfahren ist sicher und weniger invasiv, allerdings ist die Rezidivrate der Mitralklappeninsuffizienz höher als bei der konventionellen Operation⁹. Aktuell befinden sich Mitralklappenprothesen, welche über einen Katheter implantiert werden können (Transkatheter-Mitralklappenimplantation, TMVI), in der präklinischen und frühen klinischen Erprobung¹⁰. Die Entwicklung dieser Technologien setzt die Evolution hin zur minimalinvasiven Therapie der strukturellen Herzerkrankung fort. Der größte Vorteil ist die nicht mehr notwendige Verwendung der Herz-Lungen-Maschine. Durch die Entwicklung hin zum Einsatz der kathetergestützten Verfahren auch bei Patienten, die keine Hochrisikokonstellation aufweisen, ist ein zunehmender Einsatz dieser Methoden zu erwarten. Für alle Verfahren, ob minimalinvasiv chirurgisch oder kathetergestützt, ist die bildbasierte Planung und die intraoperative Bildgebung von entscheidender Bedeutung für den Erfolg des Eingriffs. Grund hierfür ist die fehlende bzw. eingeschränkte direkte Sicht. In der vorgelegten Habilitationsschrift soll der Stellenwert konventioneller bildgebender Verfahren und insbesondere deren Nutzen in der patientenspezifischen Therapieplanung und Entwicklung sowie der Simulation von Eingriffen näher beleuchtet werden.

1.2 Computertomographie der Aortenklappe und Mitralklappe

Die Computertomographie (CT) (Tomographie von altgriechisch: *tome* (*τομή*): Schnitt; *graphein* (*γράφειν*): schreiben) ist ein Schnittbildverfahren, welches mit Röntgenstrahlung Daten generiert, die dann von einem Computer zu körperscheibenartigen Bildern zusammengesetzt werden. Im Gegensatz zum konventionellen Röntgenbild erfolgt dabei keine direkte Abbildung eines Volumens auf einem zweidimensionalen Bild, welches durch die kumulative Absorption der aus einer Richtung kommenden Röntgenstrahlung durch alle Gewebeschichten entsteht. Bei der CT erfolgt die Durchstrahlung aufgrund der Rotation der Strahlenquelle um den Patienten herum aus verschiedenen Richtungen. Dadurch wird die Überlagerung verschiedener Bildpunkte vermieden. Die ersten Grundlagen stammen aus den 1960er und 1970er Jahren. Der Physiker Allan M. Cormack entwickelte bis 1963 Algorithmen zur Absorption von Röntgenstrahlung in Gewebe. Der Elektrotechniker Godfrey Hounsfield verwendete ähnliche Algorithmen und entwickelte Ende der 1960er Jahre einen Prototypen, der es ermöglichte, mit Hilfe einer

Isotopenquelle computertomographische Bilder zu erstellen¹¹. 1971 erfolgte die erste CT an einem Menschen. 1979 erhielten Cormack und Hounsfield den Nobelpreis für Physiologie oder Medizin für ihre Arbeiten zur Entwicklung der CT. Die ersten Publikationen zur CT des Herzens erschienen erst Ende der 1970er Jahre¹²⁻¹⁴. Problematisch waren initial vor allem die Bewegungsartefakte, die durch die Herzaktion verursacht wurden. Diese Schwierigkeiten konnten aber schnell überwunden werden. Die rasante Entwicklung der Technologie führte dazu, dass heutzutage die CT zur Standarddiagnostik vor Eingriffen an den Herzkappen gehört. In der konventionellen Aortenklappen chirurgie wird eine Indikation vor allem für die Planung eines Eingriffs über einen minimalinvasiven Zugang gesehen¹⁵⁻¹⁷. Durch die CT wird eine präzise Darstellung der Anatomie möglich. Wichtige Informationen, welche gewonnen werden können, sind Lage und Angulation der Aorta bezogen auf das Sternum bzw. einen Interkostalraum. Diese Information kann bei der Entscheidungsfindung zur Durchführung des Eingriffs über eine rechtslaterale Minithorakotomie oder eine partielle Sternotomie genutzt werden. Außerdem kann die Morphologie von Aortenwurzel und Aortenklappe untersucht werden. Bei der Durchführung eines Aortenklappenersatzes über eine rechtslaterale Thorakotomie kann es hilfreich sein, eine sogenannte nahtfreie Prothese zu verwenden. Diese Prothese ist aber nur für trikuspidale Aortenklappen zugelassen. Außerdem ist es notwendig, dass der Durchmesser des Aortenklappenannulus nicht zu groß oder zu klein ist, damit eine Fixierung möglich ist. Diese Informationen können detailliert aus der CT gewonnen werden.

Vor der Durchführung einer TAVI ist die CT für die Therapieplanung der Goldstandard¹⁸. Da die Möglichkeit des Ausmessens der Annulusgröße der Aortenklappe unter direkter Sicht nicht gegeben ist, muss diese vorab genau bestimmt werden, um die passende Prothese zu wählen. Spezifische Software-Applikationen wie zum Beispiel 3mensio Structural Heart (Pie Medical Imaging BV, Maastricht, The Netherlands) ermöglichen eine exakte, von Perimeter und Diameter des im CT dargestellten Aortenannulus abgeleitete Bestimmung des relevanten Durchmessers für die Auswahl einer TAVI-Prothese¹⁹. Da die CT eine Darstellung und Ausmessung der kompletten Zirkumferenz des Aortenannulus ermöglicht, scheint sie der Echokardiographie für diese Anwendung überlegen, da dieser häufig nicht rund, sondern oval ist²⁰. Des Weiteren besteht bei der CT die Möglichkeit, nicht nur das Zielgebiet an sich darzustellen, sondern auch den Zugangsweg, nämlich die Femoralgefäß und die komplette Aorta²¹. Ist dieser Zugangsweg nicht möglich, beispielsweise aufgrund einer bestehenden ausgeprägten peripheren arteriellen Verschlusskrankheit, kann der Zugangsweg über die Herzspitze, also transapikal, geplant werden²².

Im Bereich der Mitralklappenchirurgie gehört die CT nicht zum diagnostischen Goldstandard²³. Im Falle eines minimalinvasiven Zugangs kann sie präoperativ durchgeführt werden, um die Femoralgefäße für den Anschluss der Herz-Lungen-Maschine darzustellen²⁴. Außerdem können ungünstige anatomische Gegebenheiten wie zum Beispiel bei Reoperation oder Zustand nach Bestrahlung besser evaluiert werden²⁵. Aktuell findet eine rasante Entwicklung im Bereich der kathetergestützten Mitralklappenimplantation statt. Mehrere Firmen haben Prothesen entwickelt, welche über Katheterverfahren in Mitralklappenposition verankert werden können. Für diese Verfahren spielt die CT eine übergeordnete Rolle. Mehrere Publikationen haben die Wichtigkeit der CT für diese Verfahren herausgestellt²⁶⁻²⁸. In der vorliegenden Habilitationsschrift werden in den Studien, auf welche unter 2.1 bis 2.3 verwiesen wird, CT-Bilddaten verwendet, um optimierte Therapieplanungen im Bereich der Mitralklappe zu untersuchen.

1.3 Echokardiographie der Aortenklappe und Mitralklappe

Im Vergleich zur CT ist die Echokardiographie die Standarduntersuchung zur Beurteilung aller Herzklappen²³. Die Echokardiographie ermöglicht eine genaue Untersuchung von Struktur und vor allem Funktion der Klappen. Im Vergleich zur CT ist die räumliche Auflösung aber weniger gut, daher sind Abmessungen anatomischer Strukturen wie zum Beispiel der Durchmesser des Aortenannulus weniger genau. In einer Arbeit von Hang und Kollegen konnte gezeigt werden, dass die transösophageale Echokardiographie (TEE) die Annulusgröße im Vergleich zur intraoperativen Messung unterschätzt. In dieser Arbeit wurde allerdings auch beschrieben, dass in der CT die Annulusgröße überschätzt wird²⁹. In der klinischen Routine wird die Echokardiographie zur Diagnosesicherung einer Aortenklappen- oder Mitralklappenerkrankung verwendet. Perioperativ dient sie der Diagnoseverifizierung und postoperativ vor allem der Überprüfung des Operationsergebnisses. Bei TAVI-Prozeduren ist vor allem der Ausschluss einer paravalvulären Insuffizienz durch die Echokardiographie zu erreichen. Zur eigentlichen Implantation bzw. Positionierung der Prothese spielt sie nur eine untergeordnete Rolle. Im Gegensatz dazu ist bei der kathetergestützten Therapie der Mitralklappe, der MitraClip-Implantation, die TEE die entscheidende bildgebende Modalität zur Positionierung des Clips³⁰. Der Nachteil hierbei ergibt sich aus der schwierigen Darstellung des Katheters an sich in der Echokardiographie bzw. seiner ganzheitlichen Darstellung, da er immer nur in einer Ebene dargestellt werden kann. Somit ist die Orientierung im dreidimensionalen Raum Herz schwierig. Trotzdem ist bei der MitraClip-Implantation immer auch eine Fluoroskopie notwendig. Der Operateur muss also zwei bildgebende Verfahren mental fusionieren, um die Prozedur

erfolgreich durchführen zu können. Um die Vorteile verschiedener bildgebender Formate zu kombinieren wurden Software-Anwendungen zur Bildfusion entwickelt. Dies soll im Abschnitt 1.4 näher beschrieben werden.

In der vorliegenden Habilitationsschrift wird außerdem in der unter 2.7 aufgeführten Studie die TEE im Tiermodell evaluiert, welches zur Entwicklung neuer Therapieformen und somit zur Weiterentwicklung der patientenspezifischen Therapie häufig verwendet wird.

1.4 Fusion bildgebender Verfahren

Der EchoNavigator der Firma Philips ist eine Software-Anwendung, die es ermöglicht, die Echokardiographie und die Fluoroskopie zu fusionieren, das heißt in einem Bild im gleichen Koordinatensystem mit der gleichen Orientierung beide Bilder live darzustellen. Als Referenzpunkt für die gleiche Orientierung der beiden Koordinatensysteme dient die dreidimensionale Form der Echokardiographiesonde im Fluoroskopiebild. Dies soll eine Erleichterung bei der Verwendung verschiedener bildgebender Modalitäten während eines Eingriffs ermöglichen. In dieser Habilitationsschrift ist unter 2.6. eine Studie aufgeführt, in welcher die Anwendbarkeit und Sicherheit der Software während MitraClip-Eingriffen untersucht wurde.

1.5 Patientenspezifische Therapieplanung und Simulation von Eingriffen an der Aorten- und der Mitralklappe

Wie oben angeführt ist eine hochqualitative prä- und postoperative Bildgebung insbesondere bei kathetergestützten Eingriffen an der Aorten- und der Mitralklappe essentiell. Außer den in der klinischen Routine angewendeten Modalitäten wie CT und Echokardiographie wurden in den letzten Jahren zahlreiche Projekte durchgeführt, in welchen computerbasierte Simulationen von TAVI-Eingriffen mit Hilfe von Finite-Elemente-Modellen (FEM) exploriert wurden³¹. Die Finite-Elemente-Methode unterteilt das interessierende Objekt in viele kleine Elemente (finite Elemente). Für jedes dieser Elemente, dessen Eigenschaften bekannt sind, können mechanische Veränderungen wie zum Beispiel die Bewegung bei einer Deformation berechnet werden. Dies geschieht dann für alle finiten Elemente, um wieder das gesamte Objekt zu betrachten. Als Grundlage dienen hierbei wegen der guten Auflösung CT-Bilddaten. Aus diesen werden dreidimensionale Modelle der Aortenwurzel rekonstruiert, welche dann als Basis für die Implantation von virtuellen Klappenprothesen dienen. Sowohl die Aortenwurzel als auch die

Klappenprothese wird in finite Elemente unterteilt, um die Prozedur zu simulieren. Verschiedene Parameter wie Stent-Deformation oder Interaktion von Stent und Verkalkung der Aortenwurzel können simuliert und daraus bestenfalls Vorhersagen zum Ergebnis der Intervention getroffen werden. Eine Optimierung der Therapieplanung ist das Ziel dieser Ansätze. Die in der vorliegenden Habilitationsschrift unter 2.3, 2.4 und 2.5 aufgeführten Arbeiten verwenden solche Simulationen zur patientenspezifischen Therapieplanung bei TAVI-Eingriffen.

2 Eigene Arbeiten

2.1 Implantation individualisierter Mitralklappen-Annuloplastieringe im Tiermodell

Sündermann SH, Gessat M, Cesarovic N, Frauenfelder T, Biaggi P, Bettex D, Falk V, Jacobs S. Implantation of Personalized, Biocompatible Mitral Annuloplasty Rings: Feasibility Study in an Animal Model.

Interact Cardiovasc Thorac Surg 2013 Apr;16(4):417-22.³²

[doi: 10.1093/icvts/ivs531](https://doi.org/10.1093/icvts/ivs531)

In dieser Studie im Tiermodell wurde die Machbarkeit des Einsatzes von individualisierten Mitralklappenringen untersucht. Von 6 gesunden Schweinen wurde eine EKG-getriggerte CT mit 400–500 Schichten und einer Auflösung von $0,3 \times 0,3 \times 0,3 \text{ mm}^3$ angefertigt. 80 ml Kontrastmittel wurden verwendet. Anhand der Bilddaten wurde ein Modell des Mitralklappenannulus generiert. Dazu wurden die Kommissuren und 22 weitere Punkte auf dem Mitralklappenannulus identifiziert, um dessen dreidimensionale Form zu rekonstruieren. Außerdem wurden Aussparungen in das Modell eingefügt, welche später der Befestigung am nativen Annulus mit Nahtmaterial dienten. Diese computergenerierten Modelle wurden dann exportiert und durch ein Laserdruckverfahren aus einer Titanlegierung hergestellt. Nach Fertigstellung der Ringe wurden diese operativ dem jeweiligen Schwein implantiert. Es konnte gezeigt werden, dass die Bildqualität der CT gut genug war, um genaue Modelle des Mitralklappenannulus zu erstellen und herzustellen. Alle Ringe konnten erfolgreich implantiert werden. Die Zeit für das Einnähen entsprach dem konventionellen Einnähen eines Standardrings, die Zeit für das intraoperative Ausmessen entfiel durch das Verfahren.

In dieser Studie ist es gelungen, aus CT-Bildern individualisierte Mitralklappenringe zu modellieren und anhand dieser Modelle patientenspezifische Annuloplastieringe herzustellen, welche dann erfolgreich implantiert wurden. Damit konnte zum ersten Mal gezeigt werden, dass das Konzept einer patientenspezifischen Therapie der Mitralklappe realisierbar ist.

Implantation of personalized, biocompatible mitral annuloplasty rings: feasibility study in an animal model

Simon H. Sündermann^{a,*†}, Michael Gessat^{a,b,†}, Nikola Cesarovic^c, Thomas Frauenfelder^d, Patric Biaggi^e, Dominique Bettex^f, Volkmar Falk^a and Stephan Jacobs^a

^a Division of Cardiovascular Surgery, University Hospital Zurich, Zurich, Switzerland

^b Computer Vision Laboratory, Swiss Federal Institute of Technology (ETH) Zurich, Zurich, Switzerland

^c Department of Surgical Research, University Hospital Zurich, Zurich, Switzerland

^d Institute of Diagnostic and Interventional Radiology, University Hospital Zurich, Zurich, Switzerland

^e Division of Cardiology, University Hospital Zurich, Zurich, Switzerland

^f Institute of Anaesthesiology, University Hospital Zurich, Zurich, Switzerland

* Corresponding author. University Hospital Zurich, Division of Cardiovascular Surgery, Rämistrasse 100, 8091 Zurich, Switzerland. Tel: +41-44-2554775; fax: +41-44-2554446; e-mail: simon.suendermann@usz.ch (S. Sündermann).

Received 5 October 2012; received in revised form 12 November 2012; accepted 19 November 2012

Abstract

OBJECTIVES: Implantation of an annuloplasty ring is an essential component of a durable mitral valve repair. Currently available off-the-shelf rings still do not cover all the variations in mitral annulus anatomy and pathology from subject to subject. Computed tomography (CT) and echo imaging allow for 3-D segmentation of the mitral valve and mitral annulus. The concept of tailored annuloplasty rings has been proposed although, to date, no surgically applicable implementation of patient-specific annuloplasty rings has been seen. The objective of this trial was to prove the concept of surgical implantation of a model-guided, personalized mitral annuloplasty ring, manufactured based on individual CT-scan models.

METHODS: ECG-gated CT angiography was performed in six healthy pigs under general anaesthesia. Based on the individual shape of the mitral annulus in systole, a customized solid ring with integrated suturing holes was designed and manufactured from a biocompatible titanium alloy by a rapid process using laser melting. The ring was implanted three days later and valve function was assessed by intraoperative echocardiography. The macroscopic annulus–annuloplasty match was assessed after heart explantation.

RESULTS: CT angiography provided good enough image quality in all animals to allow for segmentation of the mitral annulus. The individually tailored mitral rings were manufactured and successfully implanted in all pigs. In 50%, a perfect matching of the implanted ring and the mitral annulus was achieved. In one animal, a slight deviation of the ring shape from the circumference was seen postoperatively. The rings implanted in the first two animals were significantly oversized but the deviation did not affect valve competence.

CONCLUSIONS: CT image quality and accuracy of the dimensions of the mitral annulus were sufficient for digital modelling and rapid manufacturing of mitral rings. Implantation of individually tailored annuloplasty rings is feasible.

Keywords: Cardiac surgery • Animal feasibility study • Mitral valve repair • Personalized annuloplasty

INTRODUCTION

Mitral valve repair is the gold standard treatment for mitral valve regurgitation [1, 2]. Various repair techniques, including leaflet resection and chord replacement, are used in combination with the implantation of an annuloplasty ring. Mitral annuloplasty is an essential component of a durable mitral valve repair and provides very good mid- and long-term results [3–5]. A number of off-the-shelf rings are available for different underlying pathologies. Saddle-shaped rigid or semi-rigid rings are most commonly used for the repair of primary (degenerative) mitral valve insufficiency. The GeoForm ring or the ETlogix rings (both by Edwards Lifesciences Corp., Irvine, CA, USA) are intended to treat patients

with secondary (functional) mitral valve regurgitation. All rings partly influence and remodel the three-dimensional shape of the mitral valve annulus in different ways, but do not take account of anatomical variations between individuals.

Based on the availability of 3-D imaging modalities with sufficiently high resolution and accuracy for modelling the mitral annulus, the concept of patient-specific annuloplasty rings was proposed by Lantada and colleagues [6]. This group designed a ring based on dimensional data obtained from computed tomography (CT) images. The ring was manufactured out of epoxy resin using a rapid-prototyping technique. The rings were not intended for implantation, since the material was not biocompatible and no sutures could be placed through the ring because of its solid composition. In view of these limitations, we sought to develop a personalized, implantable ring using a

^{*}S.H. Sündermann and M. Gessat contributed equally to this work.

biocompatible material and including features that facilitate implantation. Here we present a feasibility study where custom-made annuloplasty rings, individually designed, based on CT segmentations of the mitral annulus, were manufactured using a biocompatible titanium alloy and implanted in pigs.

METHODS

Study subjects

Six healthy pigs with a mean weight of 59.5 ± 2.7 kg were included. All pigs underwent a cardiac CT-scan under general anaesthesia. After tailoring and manufacturing of the individualized annuloplasty rings (see below), all animals were re-anaesthetized and operated 3 days later. Immediately after successful ring implantation and assessment of the valve

function, they were euthanized and the explanted hearts studied. The protocol was the same for all six animals and the experiment was intended as a proof of concept. All animals received humane care in compliance with the Swiss Animal Protection Law (TSchG) and the Swiss Animal Protection Act (TSchV). The study protocol was approved by the local Committee for Experimental Animal Research (Kantonales Veterinäramt des Kantons Zürich, permission number 008/2011).

Imaging and modelling

The pigs were anaesthetized and ECG-gated CT angiography (Siemens Somatom Definition Flash, Siemens Healthcare, Forchheim, Germany) was performed with 400–500 slices of $0.3 \times 0.3 \times 0.3 \text{ mm}^3$ resolution and the use of 80 ml of Ultravist 300 contrast agent. Beta-blockers and Lidocaine were

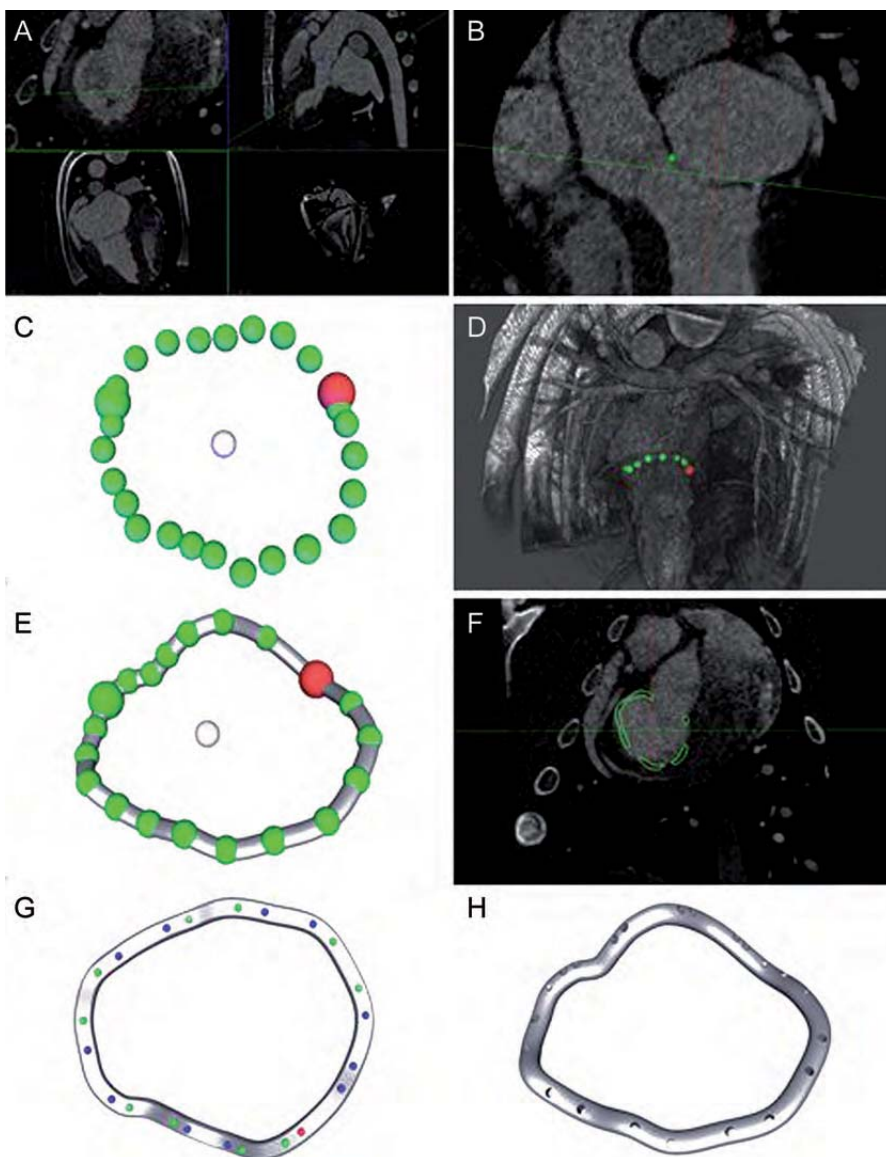


Figure 1: Process of ring manufacturing. (A) Cardiac CT images ($0.3 \times 0.3 \times 0.3 \text{ mm}^3$ resolution, end systolic); (B) manual placement of 24 landmarks on the mitral annulus; (C) 3-D shape of the mitral annulus before and (D) after smoothing; (E) computed model of annuloplasty ring following the modelled annulus; (F) ring model shown in CT images; (G) assignment of suturing holes; (H) final ring model.

administered as needed to stabilize and decrease the heart rates of the pigs to 60–70 bpm.

Using these CT images, specially developed software created a digital model of the individual mitral annuli. The principal steps of the modelling process are depicted in Fig. 1. In order to segment the mitral annulus, the software was used to localize the mitral commissures and 22 additional points on the mitral annulus. A three-dimensional model was computed as a cyclic third-order interpolant through all 24 points. This curve served as an initial centreline for the annuloplasty ring geometry. This geometry was adjusted manually before defining the positions of the suturing holes. The software ensured that the distance between holes was between 7 mm and 12 mm; indentations marking the commissures—and thus facilitating orientation during implantation—were automatically added on the atrial surface of the 3-D models (Fig. 2).

Ring production

Based on these 3-D models, tailored annuloplasty rings (Fig. 3) were produced from a titanium alloy for each pig, using the Selective Laser Melting (SLM) method [7]. SLM is an additive manufacturing process that uses a high-powered laser beam, guided by a digital 3-D model, to create three-dimensional metal parts by locally heating a metal powder above its melting temperature and fusing it. The Ti6Al4V titanium alloy that was

used is known to be biocompatible [8]. The process parameters (laser energy, melting time, curing time and afterglow) were optimized to reduce air pockets and maximize the homogeneity and mechanical durability of the material after melting. Homogeneity and air inclusion were assessed visually using microsections of material samples. Durability was tested using repetitive tensile tests.

Implantation

The rings were implanted under general anaesthesia using standard haemodynamic monitoring. Access was gained through a left-sided thoracotomy. Cardiopulmonary bypass (CPB) was installed with an arterial cannula in the descending aorta and a venous cannula in the pulmonary artery. The procedure was performed on the beating heart. The left atrium was opened and the mitral valve exposed in a standard way. The ring was implanted using single-knot sutures through the preformed holes (Fig. 2B). A sealing test indicated valve sufficiency. After closure of the left atrium, the animals were weaned off bypass and valve function was assessed by epicardial B-mode and Doppler echocardiography (Philips iE33 platform and X5-S real-time probe, Philips Medical Systems, Andover, MA, USA). Afterwards the animals were euthanized, the hearts explanted and the mitral annuli with the implanted rings dissected and examined for prosthesis-annulus alignment (Fig. 2C).

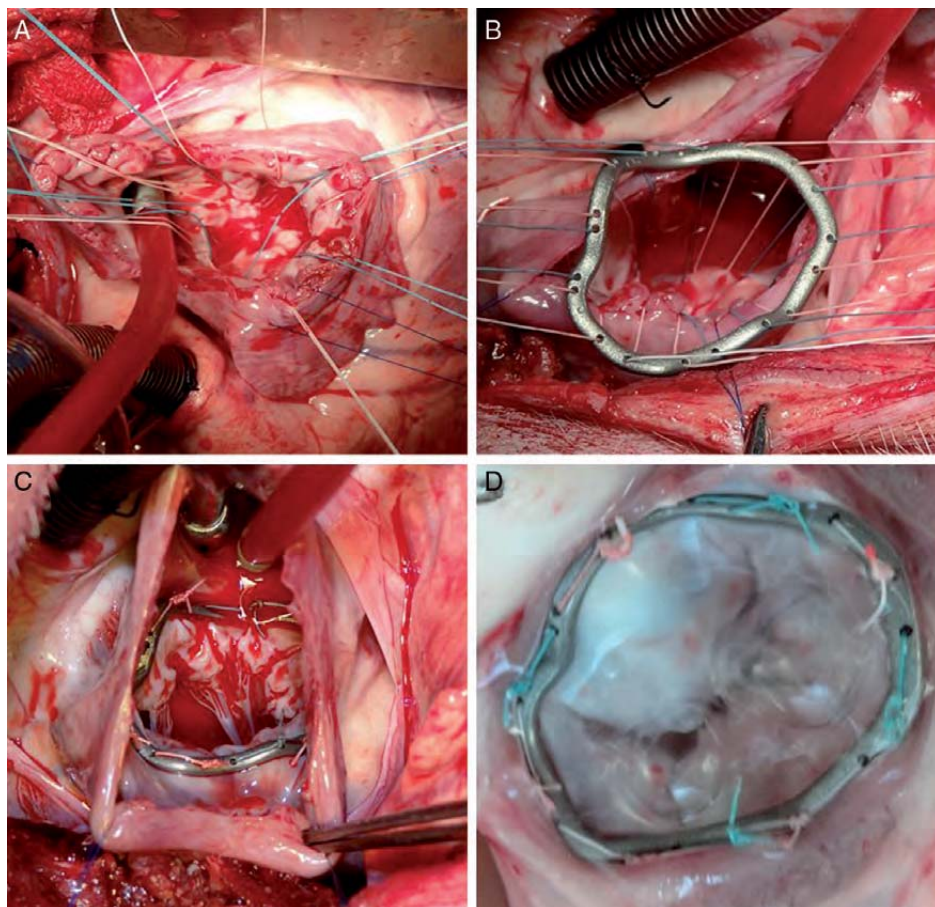


Figure 2: Ring implantation. (A) Atrial view on mitral valve; (B) preparation of sutures; (C) implanted ring; (D) explanted annulus with ring.

RESULTS

Imaging, modelling and production

Identification of the mitral annulus in the CT angiography images and ring modelling was possible in all cases. Manufacturing of the rings took three days. The precision of the melting process preserved all relevant details of the ring models, including the preformed suturing holes and commissural indentations. The mean weight of the rings was 2.2 ± 0.2 g. The mean perimeter of the rings was 109.7 ± 11.2 mm. The mean diameter from

commissure to commissure was 32.4 ± 5.2 mm. Eight to twelve suturing hole pairs were preformed and two indentations were created, corresponding to the commissures (Table 1). The computed annular geometry and the rings created from these data differed considerably in shape from commercially available mitral annuloplasty rings (Fig. 3).

Implantation

Operation time was 83 ± 25.3 min and CPB time was 50 ± 12.2 min. Ring suturing time was comparable to that for conventional annuloplasty rings but no time was required for sizing. Implantation of the individual rings was successful in all six cases. Eight to twelve sutures were necessary for attachment. In the first two animals the rings were significantly oversized; their diameters differed from the annulus around 10 mm in all directions. A system error in the modelling process was identified as a cause for this mismatch and was corrected for the subsequent implantations: the modelling process and software were adjusted accordingly before continuation of the experiment with the remaining four animals. All rings chosen in the second batch (Pigs 3–6) matched the annular circumference almost perfectly (Fig. 2C and D). Epicardial echocardiography after implantation showed no new MR and normal movement of both leaflets.



Figure 3: (A) Custom-made ring for Pig 5; (B) comparison between four rings manufactured for Pigs 3–6.

DISCUSSION

Mitral valve repair is considered the gold standard for the treatment of mitral valve regurgitation [1, 2]. Annuloplasty rings were introduced in 1971 to achieve stabilization and reduction of the mitral annulus [9]. Ring shapes underwent continuous development, from planar oval rings over planar D-shaped and later saddle-shaped rings. The rationale for this evolution is the attempt to increase the postoperative curvature of the mitral leaflets to reduce peak leaflet stress and to achieve a larger area of coaptation [10, 11]. Additionally, rings have been developed to address the asymmetric geometry of the mitral annulus in special situations such as dilated cardiomyopathy [12]. Compared to conventional (symmetrical) annuloplasty rings, asymmetric designs produce less mechanical stress at the mitral annulus, whilst achieving the same increase of the area of coaptation [13].

Table 1: Odds ratio (OR) and ring parameters

Pig	A-Weight	OR-T	CPB-T	Weight	Diameter	Post. P	Ant.P	Peri.	Stitches	Distance
P1	59.5	–	–	2.3	36.9	68.2	49	117.2	11	8
P2	60	100	70	2.43	39.2	66	57.6	123.6	12	8
P3	60.5	60	50	2.04	32.1	59.7	40	99.7	9	8
P4	54.5	65	40	2.04	24.7	70.6	30.4	101	9	6.1
P5	62.5	120	50	2.39	31.7	78.3	39.9	118.2	10	8
P6	60	70	40	2	29.6	62.1	36.4	98.5	8	7.6

P1–P6: labelling of animals; A-Weight: weight of animals in kg; OR-T: OR time in min; CPB-T: cardiopulmonary bypass time in min; Weight: weight of rings in g; Diameter: overall diameter of the ring in mm; Ant. P: perimeter from anterior to posterior commissure around the anterior annulus in mm; Post. P: perimeter from anterior to posterior commissure around the posterior commissure in mm; Peri.: total perimeter of the ring in mm; Stitches: number of stitches; Distance: distance between the suturing holes in mm.

Other concepts like flexible or partial rings were introduced with the aim of meeting the requirements of preserving annular expansion throughout the cardiac cycle[14, 15]. Devices that can be adjusted in the beating heart after closure of the atrium are now available, allowing post-procedural fine adjustment (e.g. the Valtech Cardinal adjustable annuloplasty ring: unpublished data).

In medical disciplines like orthopaedics, traumatology and oral and maxillofacial surgery, many research projects have been successfully undertaken, addressing production and implantation of patient-specific implants [16, 17]. In contrast, in cardiac surgery, individual tailoring of devices has not yet been investigated extensively. The difficulties are the soft tissue composition of the heart and the changing dimensions during the cardiac cycle. The mitral valve anatomy is complex and the three-dimensional geometry of the annulus shows high variability between individuals.

The concept of patient-specific annuloplasty rings was first introduced in 2010 [6]. The authors presented an image-based modelling approach that resulted in an annulus model that was printed in epoxy resin, using stereo lithography. The material is not biocompatible and the models were not intended for implantation.

Here we report the first animal experiment where custom-shaped solid annuloplasty rings were successfully implanted in six healthy pigs. The pig as an animal model was chosen because the anatomy of the cardiovascular system, especially the mitral valve, has been shown to be very similar to the human anatomy [18, 19]. The rings were designed according to the individual annular morphology. Unlike in previous approaches, the rings were custom-made from a biocompatible Ti6Al4V titanium alloy in a rapid manufacturing process. The ring design included suturing holes, assuring good fixation at the annulus, and featured commissural markers facilitating the correct ring orientation—an aspect which is of particular importance when dealing with asymmetrical rings.

Image quality and accuracy of CT imaging were sufficient for the digital modelling of the annulus. Nevertheless, the use of 3-D echocardiography may be considered as an alternative approach for further investigations, as this technique allows for studying the mitral annular shape dynamically, compared to the non-dynamic CT assessment. Which moment of the cardiac cycle is best for defining the final shape and size of an individually tailored annuloplasty ring is a subject that remains to be studied.

The chosen design, consisted of a solid, biocompatible titanium alloy ring with inbuilt suturing holes that ensured secure implantation and commissural markers that facilitated positioning of the ring. Suturing times were comparable to suturing times with conventional rings, while no CBP time was wasted on ring sizing.

An important advantage of patient-specific mitral valve annuloplasty might be the possibility of individual treatment optimization, based on quantitative functional models. Modifications of the annuloplasty ring—addressing the individual underlying pathology, including symmetrical or asymmetrical downsizing—might result in a better outcome. However, the proof of such a concept is still lacking.

The present study only investigated the acute feasibility of implantation of custom-made solid metal rings. At this point, no assessment of long-term aspects—such as endothelial healing—has been performed. Also, the mitral valves of the study pigs were competent and hence no statement can be made

concerning reduction of mitral regurgitation or valve competence after correctional ring annuloplasty. The next research steps therefore include chronic animal trials, fatigue testing and refinement of the modelling software, as well as studying the efficacy in subjects with mitral regurgitation.

In conclusion, the concept of personalized annuloplasty might offer patient-specific treatment of mitral valve disease according to the individual anatomy and pathology. Planning, production and implantation of individually built, biocompatible annuloplasty rings are feasible in an animal model.

Funding

This work was funded by the Swiss Heart Foundation within its regular program for supporting basic research.

Conflict of interest: none declared.

REFERENCES

- [1] Vahanian A, Alfieri O, Andreotti F, Antunes MJ, Barón-Esquivias G et al. Authors/Task Force Members. Guidelines on the management of valvular heart disease (version 2012): The Joint Task Force on the Management of Valvular Heart Disease of the European Society of Cardiology (ESC) and the European Association for Cardio-Thoracic Surgery (EACTS). Eur J Cardiothorac Surg 2012;42:S1-44.
- [2] Markar SR, Sadat U, Edmonds L, Nair SK. Mitral valve repair versus replacement in the elderly population. J Heart Valve Dis 2011;20:265-71.
- [3] Seeburger J, Borger MA, Doll N, Walther T, Passage J, Falk V et al. Comparison of outcomes of minimally invasive mitral valve surgery for posterior, anterior and bileaflet prolapse. Eur J Cardiothorac Surg 2009; 36:532-38.
- [4] David TE, Ivanov J, Armstrong S, Christie D, Rakowski H. A comparison of outcomes of mitral valve repair for degenerative disease with posterior, anterior, and bileaflet prolapse. J Thorac and Cardiovasc Surg 2005; 130:1242-49.
- [5] Braunberger E, Deloche A, Berrebi A, Abdallah F, Celestin JA, Meimoun P et al. Very long-term results (more than 20 years) of valve repair with Carpentier's techniques in nonrheumatic mitral valve insufficiency. Circulation 2001;104:I8-I11.
- [6] Diaz Lantada A, Valle-Fernández RD, Morgado PL, Muñoz-García J, Muñoz Sanz JL, Munoz-Guijosa JM et al. Development of personalized annuloplasty rings: combination of CT images and CAD-CAM tools. Ann Biomed Eng 2010;38:280-90.
- [7] Vandenbroucke B, Kruth J. Selective laser melting of biocompatible metals for rapid manufacturing of medical parts. Rapid Prototyping Journal 2007;13:196-203.
- [8] Long M, Rack HJ. Titanium alloys in total joint replacement—a materials science perspective. Biomaterials 1998;19:1621-39.
- [9] Carpentier A, Deloche A, Dauplain J, Soyer R, Blondeau P, Piwnica A et al. A new reconstructive operation for correction of mitral and tricuspid insufficiency. J Thorac Cardiovasc Surg 1971;61:1-13.
- [10] Jensen M, Jensen H, Smerup M, Levine R. Saddle-shaped mitral valve annuloplasty rings experience lower forces compared with flat rings. Circulation 2008;118:250-55.
- [11] Salgo IS, Gorman JH, Gorman RC, Jackson BM, Bowen FW, Plappert T et al. Effect of annular shape on leaflet curvature in reducing mitral leaflet stress. Circulation 2002;106:711-17.
- [12] De Bonis M. The GeoForm annuloplasty ring for the surgical treatment of functional mitral regurgitation in advanced dilated cardiomyopathy. Eur J Cardiothorac Surg 2011;40:488-95.
- [13] Daimon M, Fukuda S, Adams DH, McCarthy PM, Gillinov AM, Carpentier A et al. Mitral valve repair with Carpentier-McCarthy-Adams IMR ETlogix annuloplasty ring for ischemic mitral regurgitation: early echocardiographic results from a multi-center study. Circulation 2006; 114:I588-93.

- [14] Durán CMC, Pomar JL, Cucchiara GG. A flexible ring for atrioventricular heart valve reconstruction. *J Cardiovasc Surg (Torino)* 1978;19: 417–20.
- [15] Odell JA, Schaff HV, Orszulak TA. Early results of a simplified method of mitral valve annuloplasty. *Circulation* 1995;92:I1150–54.
- [16] Scolozzi PP. Maxillofacial reconstruction using polyetheretherketone patient-specific implants by 'mirroring' computational planning. *Aesthetic Plast Surg* 2012;36:660–65.
- [17] Shen F, Chen B, Guo Q, Qi Y, Shen Y. Augmented reality patient-specific reconstruction plate design for pelvic and acetabular fracture surgery. *Int J Comput Assist Radiol Surg* 2012;[Epub ahead of print].
- [18] Smerup M, Pedersen T, Nyboe C. A long-term porcine model for evaluation of prosthetic heart valves. *Heart Surgery Forum* 2004;7:e259–e264.
- [19] Crick SJS, Sheppard MNM, Ho SYS, Gebstein LL, Anderson RHR. Anatomy of the pig heart: comparisons with normal human cardiac structure. *J Anat* 1998;193 (Pt 1):105–19.

eComment. Personalized annuloplasty rings for mitral valve repair: lessons from the pig model

Authors: Leo A. Bockeria, Aleksandr A. Fadeev, Aleksandr P. Melnikov and Osman A. Makhachev

Bakoulev Scientific Center for Cardiovascular Surgery, Moscow, Russia

doi: 10.1093/icvts/ivt069

© The Author 2013. Published by Oxford University Press on behalf of the European Association for Cardio-Thoracic Surgery. All rights reserved.

It does make sense to try to develop a method to tailor and manufacture personalized patient-specific annuloplasty rings with regard to preoperative computed tomography (CT)-sizing of a patient's mitral valve annulus [1]. The sizing of mitral annulus area, the knowledge of normal and pathological dynamics of the annulus is essential prior to surgical mitral repair. The dimensions of the mitral annulus

vary considerably among individuals [2]. Off-the-shelf rings currently available tend to disregard anatomic variations. Such variability is detected in clinical practice and could be taken into consideration when configuring annuloplasty rings. The authors' idea is to make a 3D-segmentation of the mitral valve and mitral annulus of a patient in systole before surgery. The *in vivo* study on the animal model has demonstrated that a "three-step" algorithm consisting of CT-annulus sizing, digital modeling and ring manufacturing, and finally the implantation of such patient-specific devices is feasible. This is quite evident from the article. What only remains is to evaluate the performance of mitral annulus correction using such ring in a patient with mitral valve pathology. We need to answer the question: what is the point of making an annuloplasty using a ring obtained by scanning the pathologically changed annulus of the mitral valve. In this case, the outcome of mitral correction is likely to fail.

It is quite obvious that before being implanted in a patient with mitral regurgitation, both the shape and the dimensions of such a ring need to be modified (reduced or downsized) to required values. The authors accept the possibility of modifying annuloplasty rings obtained for an individual by using CT-images of the diseased mitral valve to be corrected. It remains unclear how a solid metal ring can be downsized. However, the authors do not propose any technology for solid ring modification. This device, as attested by clinical practice, is often used in cardiac surgery to compensate for valve tethering and to force coaptation.

In conclusion, we would like to congratulate the authors of the article on the innovative method they use to address the issue of developing a person-specific implantable device.

Conflict of interest: none declared.

References

- [1] Sündermann S, Gessat M, Cesarovic N, Frauenfelder T, Biaggi P, Bettex D et al. Implantation of personalized, biocompatible mitral annuloplasty rings: feasibility study in an animal model. *Interact CardioVasc Thorac Surg* 2013;16:417–22.
- [2] Isnard R, Acar C. The mitral annulus area: a useful tool for the surgeon. *J Heart Valve Dis* 2008;17:243–50.

2.2 Computertomographie zur Planung der Implantation eines kathetergestützten Mitralklappen-Annuloplastie-Bandes. Anwendungsstudie im Tiermodell

Sündermann SH, Gordic S, Manka R, Cesarovic N, Falk V, Maisano F, Alkadhi H. Computed Tomography for Planning and Postoperative Imaging of Transvenous Mitral Annuloplasty: First Experience in an Animal Model. Int J Cardiovasc Imaging 2015 Jan;31(1):135-42.³³

[doi: 10.1007/s10554-014-0516-7](https://doi.org/10.1007/s10554-014-0516-7)

In dieser Studie wurde die CT im Großtiermodell verwendet, um eine individualisierte Therapieplanung zu evaluieren. Für Hochrisikopatienten ist seit ca. 2 Jahren ein Gerät zur kathetergestützten Behandlung der Mitralklappeninsuffizienz verfügbar, das sogenannte Cardioband der Firma Valtech³⁴. Es handelt sich dabei um ein Annuloplastie-Band, welches mit mehreren schraubenartigen Ankern am Mitralklappenannulus befestigt wird. Dabei ist es wichtig, für jeden Patienten vor dem Eingriff die benötigte Länge des Bandes festzulegen. Während der präklinischen Entwicklung des Cardiobandes wurde bei 7 Schweinen aus dieser Serie ein präoperatives CT angefertigt, um die individuellen Parameter des Mitralklappenannulus jedes Tieres auszumessen. Relevante Werte waren unter anderem der Diameter des Mitralklappenannulus, der Abstand von Kommissur zu Kommissur auf dem posterioren Annulus sowie der Abstand zum Ramus circumflexus. Das Cardioband wurde dann bei allen Tieren im Akutexperiment implantiert. Nach der Implantation erfolgte erneut die Durchführung einer CT. Anschließend wurde das Herz entnommen und makroskopisch untersucht. Es zeigte sich, dass die Darstellung des Mitralklappenannulus anhand der CT möglich ist. Auch in der postoperativen Untersuchung ergaben sich durch die Anker keine Artefakte, die die Bildqualität in höherem Maße beeinträchtigten. Die Implantation des Cardiobandes gelang in allen Tieren und die präoperative Längenbestimmung war korrekt gelungen, was sich außer in der präoperativen CT auch in der makroskopischen Inspektion der Herzen zeigte.

Es ist in dieser Studie gelungen zu zeigen, dass die CT zur individuellen Therapieplanung einer kathetergestützten Mitralklappenannuloplastie geeignet ist. Die Ergebnisse der Studie, insbesondere das modifizierte CT-Protokoll, werden aktuell in einer multizentrischen Zulassungsstudie am Menschen verwendet.

Computed tomography for planning and postoperative imaging of transvenous mitral annuloplasty: first experience in an animal model

Simon H. Sündermann · Sonja Gordic ·
Robert Manka · Nikola Cesarovic · Volkmar Falk ·
Francesco Maisano · Hatem Alkadhi

Received: 3 July 2014/Accepted: 8 August 2014/Published online: 15 August 2014
© Springer Science+Business Media Dordrecht 2014

Abstract To investigate the use of computed tomography (CT) to measure the mitral valve annulus size before implantation of a percutaneous mitral valve annuloplasty device in an animal trial. Seven domestic pigs underwent CT before and after implantation of a Cardioband™ (a percutaneously implantable mitral valve annuloplasty device) with a second-generation 128-section dual-source CT machine. Implantation of the Cardioband™ was performed in a standard fashion according to a protocol. Animals were sacrificed afterwards and the hearts explanted. The Cardioband™ was found to be adequately implanted in all animals, with no anchor dehiscence and no damage of the circumflex artery (CX) or the coronary sinus (CS). The correct length of the band as chosen according to the length of the posterior mitral annulus measured in CT before implantation was confirmed in gross examination in all animals. The device did not result in a metal artifact-

related degradation of image quality. The closest distance from the closest anchor to the CX was 2.1 ± 0.7 mm in diastole and 1.6 ± 0.5 mm systole. Mitral annulus distance to the CS was 6.4 ± 1.3 mm in diastole and 7.7 ± 1.1 mm in systole. CT visualization and measurement of the mitral valve annulus dimensions is feasible and can become the imaging method of choice for procedure planning of Cardioband™ implantations or other transcatheter mitral annuloplasty devices.

Keywords Computed tomography · Mitral annuloplasty · Heart · Mitral annulus

Abbreviations

CT	Computed tomography
CX	Circumflex artery
ECG	Electrocardiogram
FoV	Field of view
ICE	Intracardiac echocardiography
IVC	Inferior vena cava
MR	Mitral valve regurgitation
MVR	Mitral valve repair
SAFIRE	Sinogram-affirmed iterative reconstruction
TAVI	Transcatheter aortic valve implantation
TSchG	Swiss Animal Protection Law
TSchV	Swiss Animal Protection Act

Introduction

Mitral valve repair (MVR) has become the gold standard therapy for severe mitral valve regurgitation (MR) with excellent results [1, 2]. However, due to age, comorbidities, and poor left ventricular function up to 50 % of symptomatic patients with severe MR are not referred to surgery [3].

S. H. Sündermann · V. Falk · F. Maisano
Division of Cardiovascular Surgery, University Hospital Zurich,
Zurich, Switzerland

S. Gordic · R. Manka · H. Alkadhi (✉)
Institute of Diagnostic and Interventional Radiology, University
Hospital Zurich, Zurich, Switzerland
e-mail: hatem.alkadhi@usz.ch

R. Manka
Clinic of Cardiology, University Hospital Zurich, Zurich,
Switzerland

R. Manka
Institute for Biomedical Engineering, University and ETH
Zurich, Zurich, Switzerland

N. Cesarovic
Department of Surgical Research, University Hospital Zurich,
Zurich, Switzerland

Several new transcatheter techniques have been introduced for treating MR in high risk surgical candidates. The currently most popular device is the MitraClip™ that produces a double orifice by clipping the free edges of the mitral valve together [4]. Other devices are placed through percutaneous intervention into the coronary sinus with the aim to reduce the size of the posterior annulus [5, 6]. Further devices use techniques directly addressing the annulus either mechanically or using energy sources to shrink the annular tissue. The Mitralign™ device uses a cinching technique at the mitral valve annulus for reducing its size. The QuamumCor™ device reduces the size of the posterior mitral annulus with radiofrequency ablation [7]. Irrespective of the device used, precise planning of such minimally invasive procedures is essential. This planning mainly includes estimations of the required device size for the individual patient before implantation.

Recently, the Cardioband™ (ValtechCardio, Or Yehuda, Israel) direct annuloplasty system was introduced to closely replicate surgical implant of a posterior annuloplasty Dacron™ band, with a transfemoral percutaneous approach [8]. Multidetector computed tomography (CT) has been used as an imaging modality for pre-procedural sizing of the device and planning of the Cardioband™ implantation procedure. Herein we report our initial experience in the animal model that has been used for the preclinical evaluation of the device prior to human clinical trials.

Materials and methods

All animals received human care in compliance with the Swiss Animal Protection Law (TSchG) and the Swiss Animal Protection Act (TSchV). The study protocol was approved by the local Committee for Experimental Animal Research (Kantonales Veterinäramt des Kantons Zürich, permission number 161/2012).

Seven domestic pigs with a mean weight of 99.8 ± 6.9 kg (range 90–112 kg) underwent procedure planning and Cardioband™ implantation. CT was performed in all animals pre- and postoperatively. General anesthesia was induced with Propofol and maintained with Propofol and Isoflurane. Amiodarone (150–300 mg) was administered preoperatively to avoid arrhythmias during the procedure.

After the postoperative CT scan all animals were sacrificed and the hearts were explanted. The left ventricle's anterior wall was split from the middle of the anterior mitral leaflet to the apex. The correct positioning of the Cardioband™ was verified and the length was measured at the expanded heart.

CT imaging protocol and data reconstruction

Under general anesthesia, animals were scanned twice—immediately before and after Cardioband™ implantation—with a second-generation 128-section dual-source CT machine (Somatom Definition Flash, Siemens Healthcare, Forchheim, Germany) equipped with an integrated circuit detector (Stellar, Siemens Healthcare, Forchheim, Germany) [9]. The data acquisition was synchronized with the electrocardiogram (ECG) of the animals using retrospective ECG-gating, and with the following scan parameters: detector collimation $2 \times 0.6 \times 64$, slice acquisition $2 \times 0.6 \times 128$ by means of a z-flying focal spot, gantry rotation time 0.28 s, tube current–time product 380 mAs/rotation, and tube voltage 120 kVp.

Eighty ml iopromide (Ultravist® 370, Bayer Healthcare, Berlin, Germany) was used as contrast agent for the CT scans.

All CT data was reconstructed using a slice thickness of 0.6 mm and increment of 0.4 mm using sinogram-affirmed iterative reconstructions (SAFIRE) at a strength level of 3 [10]. The reconstruction field-of-view (FoV) was set to 200 mm with a pixel matrix of 512×512 . Images were reconstructed in 10 % steps of the RR-interval.

Definition of the mitral annulus and CT data analysis

The mitral annulus is a fibrous cord that marks the hinge-line of the 2 mitral valve leaflets. The anterior border of the mitral annulus is related to the aortic valve and the right and left fibrous trigones. In the area of aortic-mitral fibrous continuity, the distal margin of the left atrial myocardium over the leaflet defines the hingeline of the anterior mitral annulus. The area opposite of the fibrous continuity corresponds to the posterior mitral annulus [11].

The following measurements in systole (30 % of the RR-interval) and in diastole (70 % of the RR-interval) were performed using the multiplanar reformation software tool installed on the scanner workstation as described in [12]:

- After reformation in a 2D short-axis a slice was chosen where the anterolateral and posteromedial commissures could be identified. The posterior circumferential distance of the commissures was defined as the posterior mitral annular circumference and was measured free-hand (Fig. 1a),
- Shortest distance from the posterior annular circumference to the circumflex artery (CX) was measured after following the CX in its entire length (Fig. 1b),

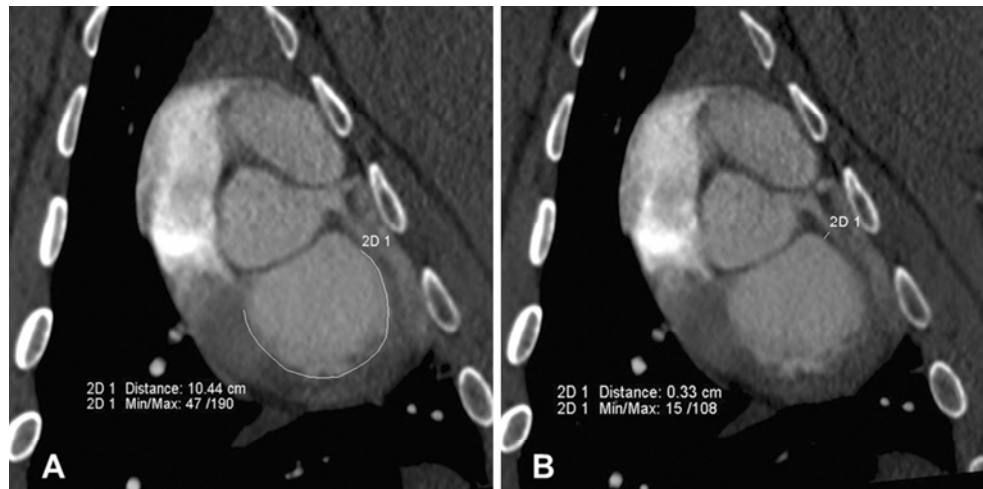


Fig. 1 CT short-axis reformations parallel to the mitral annulus showing the measurements of the **a** posterior mitral annular circumference and the **b** shortest distance of the posterior mitral annulus to the circumflex artery

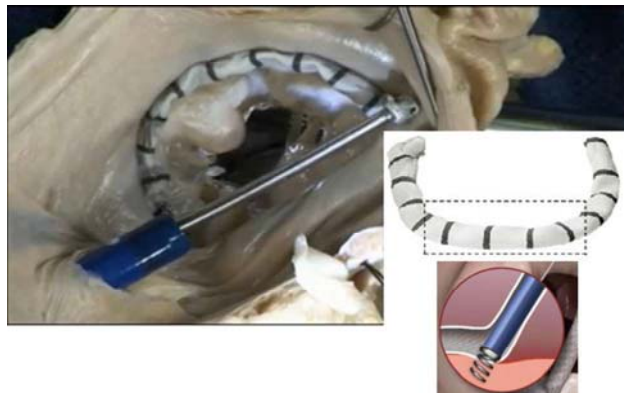


Fig. 2 Schematic representation of the Cardioband™ implantation. The *large image* shows the Cardioband™ implanted in a cadaver atrium. The *inlay picture* shows the Cardioband™ and a schematic of the anchors used to fix the device at the mitral valve annulus

- Shortest distance from the posterior annular circumference to the coronary sinus was measured after following the coronary sinus in its entire length,
- Device length by measuring free-hand the circumferential length along the device from the first anchor to the last anchor in a 2D short-axis reformation, and
- Shortest distance of the closest anchor to the CX.

The Cardioband™ device

The Cardioband™ (Valtech Cardio, Or Yehuda, Israel) consists of a delivery system made for transvenous access and a Dacron band intended to be anchored sutureless

Table 1 Available Cardio-band™ sizes according to the measurements of the posterior mitral annular circumference commissure to commissure distance in mm

Length in mm	Cardioband™ size
73–80	A
81–88	B
89–96	C
97–104	D
105–112	E
113–120	F

along the posterior mitral annulus from commissure to commissure in the beating heart. Iliac artery sizing is not mandatory prior to the procedure, because access to the mitral valve is gained through transseptal puncture from the right atrium which is approached from the femoral vein. Cardioband™ is fixated along the annulus using a series of stainless steel anchors delivered through the implant into the native annular tissue. After implantation, the band can be contracted or expanded with an adjustment tool under echocardiographic guidance (Fig. 2). The adjustment induces a reduction of the distance from commissure to commissure and also of the anterior–posterior diameter, and with that also increases the length of coaptation of the anterior and the posterior mitral valve leaflet.

The Cardioband™ is available in different lengths from 73 to 120 mm. The necessary size has to be chosen before the implantation and depends on the length of the posterior mitral valve annulus from commissure to commissure. The planning algorithm for the CT measurements is described below. The Cardioband™ lengths according to the measurements of the posterior mitral annular circumference commissure to commissure distance is provided in Table 1.

Implantation procedure

After preoperative CT, the animals were kept in general anesthesia and brought to the animal hybrid operating room. All implantations were performed in a state-of-the-art hybrid operating theater (Philips monoplane AlluraXper FD20C) with support of angiography and intracardiac echocardiography (ICE).

Access was gained through a right-sided, muscle sparing thoracotomy in the 4th and 5th intercostal space. Access to the right atrium was gained through a 10 mm DacronTM prosthesis, sutured to the lower part of the right atrium close to the inferior vena cava (IVC) with an angulation of around 45° meant as a neo-IVC. This step was undertaken because the angulation between the natural IVC and the mitral annular plane is more acute in pigs compared to humans. A large port-like construct was placed into the end of the prosthesis as access for the catheters and devices. A 10Fr sheath was placed in the apex of the heart, a 10Fr sheath was placed in the femoral artery as access for two ICE catheters (Acunav, Siemens Healthcare, Forchheim, Germany) that were used for guiding the implantation.

The first step of the procedure is transseptal puncture to gain access to the left atrium above the mitral valve. The CardiobandTM delivery system (transseptal steerable sheath and implant delivery system) was placed into the left atrium above the mitral valve over an Amplatz Superstiff (Boston Scientific, Natick, MA, USA) guide wire. Anchors were loaded through the delivery system individually and advanced into the anchor channel through the implant. The first anchor was placed in the anterolateral commissure. Placement of further anchors was then performed in a counter-clockwise direction, until reaching the posteromedial commissure. Every intended anchoring position was confirmed by ICE and angiography. After complete implantation of the CardiobandTM, it was released from the delivery system. Using a specialized catheter, the size of the CardiobandTM could be reduced temporarily to proof functionality of the system, and therefore restored to its initial size. The implant delivery system would be then disconnected and the neo-IVC was ligated close to the atrial anastomosis. The thoracotomy was closed and the animals were brought to the CT again to visualize and to measure the length of the CardiobandTM. After the second CT, the animals were euthanatized and the heart explanted to visually verify correct or incorrect placement of the anchors and to verify the correct length of the CardiobandTM chosen before the implantation.

Results

Transseptal puncture and implantation of the first anchor of the CardiobandTM could be performed in all animals. In all

animals, the implantation of the whole device including retrieval of the delivery device could be successfully performed.

After sacrificing the animals, hearts were explanted. Measurements of the length of the CardiobandTM could be successfully performed on postoperative CT in all animals. Gross examination found the CardiobandTM adequately implanted in all animals, with no anchor dehiscence and no surrounding structure damage (including no circumflex artery lesions). In all animals the CardiobandTM was implanted exactly from commissure to commissure confirming accuracy of the preoperative performed CT measurements.

Qualitative CT image analysis

The CardiobandTM device did not result in a metal artifact-related degradation of image quality in any of the animals. Both the implant and the surrounding structures could be visualized on postinterventional CT with high quality. The single anchors are clearly visualized as well as the adjustment mechanism close to the first anchor (Fig. 3).

Every single anchor can be clearly identified with a screw placed in the mitral valve annulus. Close to the first anchor at the anterolateral commissure, the adjustment coil is located. The unharmed circumflex artery could be visualized clearly to exclude accidental injury to the vessel and resulting bleeding or ischemia. The CardiobandTM itself was not visualized by CT.

In-vivo and ex vivo measurements

The results from in vivo and ex vivo measurements are summarized in Table 2.

Before implantation, the mitral valve circumference and the posterior mitral annulus length was 9.9 ± 0.4 cm (range 9.4–10.4 cm) during diastole and 8.94 ± 0.3 cm (range 8.5–9.4 cm) during systole. After implantation, the mean Cardioband length measured in MDCT was 8.77 ± 0.6 cm during diastole and 8.59 ± 0.4 cm during systole. Direct measurements after explantation revealed an average length of the implant of 9.87 ± 0.7 mm (Fig. 4).

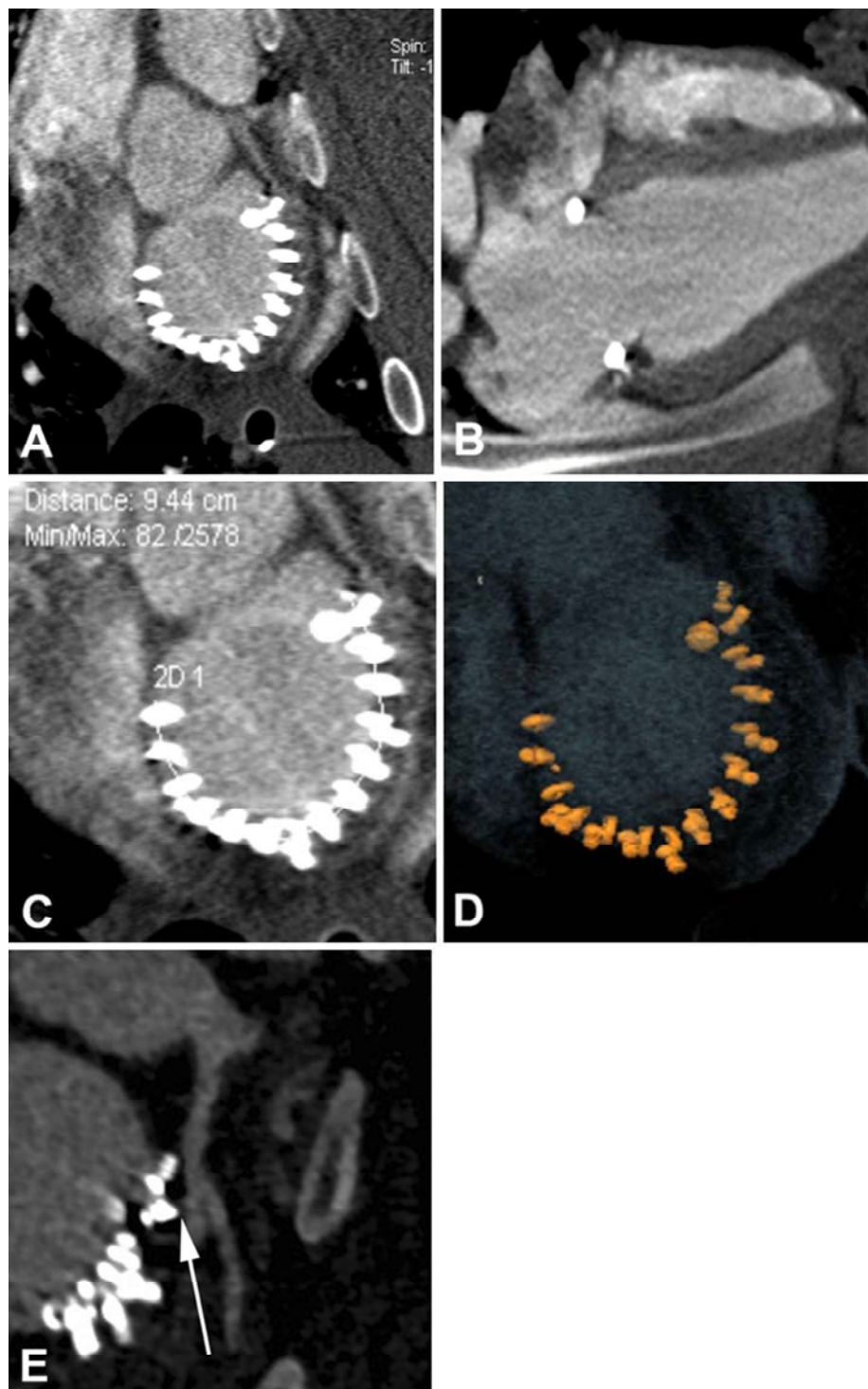
The distance from the posterior mitral annulus to the CX varied among the animals, with a median distance of 3.3 ± 0.8 mm (range 3–6 mm) in diastole and 3.9 ± 1.2 mm during systole (range 1–3 mm) (see Fig. 1b).

The distance from the posterior mitral annulus to the coronary sinus varied among the animals, with a median distance of 6.4 ± 1.3 mm (range 4–8 mm) in diastole and 7.7 ± 1.1 mm during systole (range 6–9 mm).

After implantation of the CardiobandTM, the closest distance from the closest anchor to the CX was 2.1 ± 0.7 mm (range 1–3 mm) in diastole and 1.6 ± 0.5 mm (range 1–2 mm) in systole (see Fig. 3).

Fig. 3 CT reformations after Cardioband™ implantation **a** in the short-axis and **b** in the long axis of the left ventricle.

c Measurements of the device length after implantation and **d** 3D volume rendered image of the implant. Zoomed maximum intensity image **e** illustrates the close spatial relationship of the anchors of the device to the CX (arrow)



Discussion

To the best of our knowledge, this study is the first to describe the results from pre- and postoperative CT evaluation of a direct annuloplasty device. We provide measurements of the posterior mitral annulus with CT pre- and postoperatively and after intervention in explanted hearts in

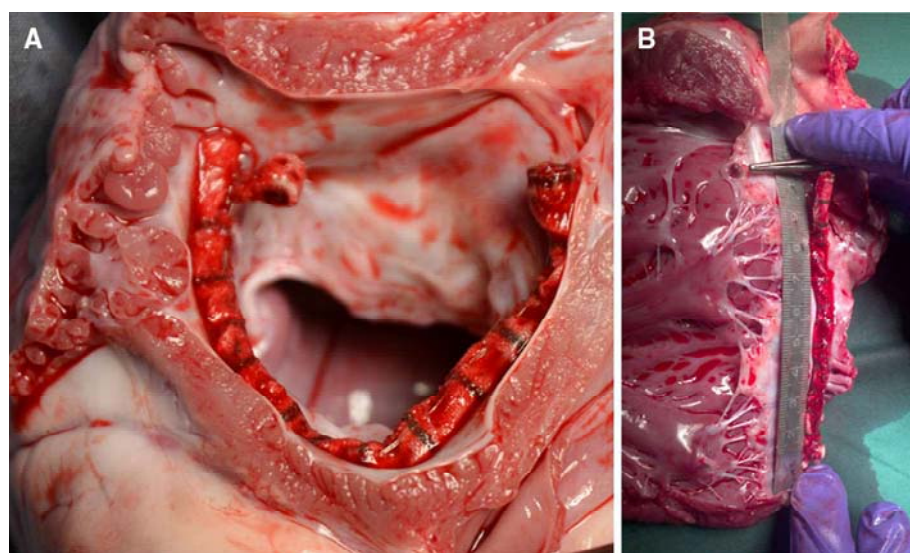
an animal study during preclinical evaluation of the Cardioband™ system, a direct annuloplasty device replicating a surgical posterior annuloplasty band procedure.

Surgical MVR is the gold standard therapy for MR [1, 2]. Since few years, new concepts and devices are developed for off-pump interventions to avoid the need of cardiopulmonary bypass and cardioplegia. Former devices

Table 2 Measurement results for the CT and the direct measurement of the CardioBand™ (diastole/systole)

	Weight (kg)	Posterior annular length CT pre (cm) (diastole/systole)	Cardioband length CT post (cm) (diastole/systole)	Cardioband length Explant (cm)	Shortest distance of mitral annulus to circumflex artery (mm) (diastole/systole)	Shortest distance of the closest anchor to the circumflex artery (mm) (diastole/systole)	Shortest distance of mitral annulus to coronary sinus/great cardiac vein (mm) (diastole/systole)
Animal 1	112	10.4/9.4	9.4/9.2	10.5	3/3	1/2	4/6
Animal 2	99.5	9.4/8.8	8.4/8.2	—	3/3	2/2	6/7
Animal 3	103	9.8/9.0	8.9/8.7	9	3/3	3/2	7/9
Animal 4	90	9.9/9.0	8.3/8.5	9.7	5/6	3/1	8/9
Animal 5	95	9.8/8.5	8.1/8.5	9.7	3/4	2/2	7/7
Animal 6	97.5	9.7/8.9	8.5/8.2	9.5	3/3	2/1	6/8
Animal 7	101.5	10.3/9.0	8.9/8.8	10.8	4/5	2/1	7/8

Fig. 4 Explanted pig heart after removal of the left atrium. **a** The Cardioband™ is anchored in the posterior mitral annulus from commissure to commissure along the posterior leaflet. **b** Outspread mitral annulus for manual measurement of the length of the device



focused on the CS. The MONARC and the CARILLON device are placed in the CS via a catheter and are intended to improve leaflet coaptation in secondary mitral valve regurgitation [5, 6]. The concept of these devices was shown to be feasible, but clinical results are not yet convincing. Main issues are the variability of the coronary sinus anatomy and the potential for compressing the circumflex artery. More recently, direct annuloplasty has gained growing interest, as the ideal approach for percutaneous mitral valve annuloplasty. The Cardioband™ device is intended to be anchored directly to the mitral valve posterior annulus from commissure to commissure. Promising results are available from an animal trial with direct atrial approach [8]. An important issue of such procedures is precise planning and pre-procedural choice of the correct implant size. Standard modality for mitral valve imaging pre-, post- and intraoperatively actually is transesophageal echocardiography (TEE) [2, 13, 14]. One major concern about TEE is operator dependency and

reproducibility of echocardiographic results [15]. Besides TEE, CT has been described for assessment of the mitral valve anatomy for patients with normal renal function that can be harmed with contrast medium. Delgado and colleagues assessed mitral valve anatomy and geometry with 64-slice CT in a cohort of 151 consecutive patients [16]. Besides others, they measured mitral valve area, diameter from commissure to commissure and anteroposterior diameter. Patients with and without secondary MR were compared, and differences in mitral valve geometry were demonstrated. However, no systematic surgical assessment of the patients was available to confirm their CT measurements.

In a study performed by our group, we assessed the three-dimensional shape of the mitral valve in order to produce patient-specific annuloplasty rings in an animal experiment [17]. In this study, CT was used to produce an exact model of the mitral valve annulus. In a rapid prototyping procedure, rings were produced from these models

and implanted in 6 healthy pigs. It could be observed, that the shape of the rings matched almost perfectly to the annular circumference. From this data, we concluded that assessment of the mitral annulus with CT is feasible and offers an exact visualization of the structures of interest. In a recent study by Wang and colleagues [18], CT was used as basis for finite element modeling of the mitral valve. Only one patient was identified as eligible out of a database for the study due to sufficient image quality. From these images a model of the whole mitral valve within systole and diastole could be constructed. This confirms the role and the importance of use and improvement of CT imaging in mitral valve disease. In our study we compared the annular dimension in systole and diastole, too. We found the posterior annulus length to be decreased around 10 % during systole. This corresponds to *in vivo* findings in humans [19]. We could not find in the literature such measurements in animals.

In this study, CT reliably predicted posterior annular size in all animals undergoing the procedure. Compared to baseline, annular size was slightly reduced in the follow-up CT, especially compared to the diastolic measurement, due to some residual cinching after Cardioband™ implantation. The Cardioband™ was intentionally disconnected with minimal amount of cinching in this study to focus on CT sizing performance. However, we must acknowledge the study limitation that our animal population was rather homogenous in size, and our results suggest that a 9.5–10 cm ring could have been used in all animals.

In addition, CT allowed for an evaluation of the shortest distance from the posterior mitral annulus to the CX and to the coronary sinus prior to intervention, and allowed for a depiction of the spatial relationship and distance of the closest anchor to the CX and coronary sinus after Cardioband™ implantation. The distance from the anchor to the CX varied between 1 and 3 mm in this study. No injuries or impingements of the CX were found in gross examination. Nevertheless, this remains a potential complication of the procedure. Therefore, we consider it important to obtain precise imaging of these structures prior to implantation to be aware of the exact close anatomical proximity which might increase the risk of these complications. Together these findings support the use of CT as an adjunct to TEE for procedure planning and for post-interventional control in mitral valve procedures for ongoing and future clinical trials.

Currently, Cardioband™ is under clinical evaluation in a feasibility and safety human trial. Patient selection and device sizing is strongly supported by CT derived imaging. CT is used to size the annulus, in a similar fashion to what described here, and to guide device size selection. In addition, CT offers invaluable information relative to anatomy of the annulus, relationship with the circumflex

artery, and presence and quantification of annular or leaflet calcification, which would be a contraindication for any annuloplasty procedure.

Another fact underlining the importance of CT as planning tool is that in contrast to mitral valve interventions, for transcatheter aortic valve implantation (TAVI) procedures, computed tomography already has become the standard imaging modality to plan the procedure [20] due to its versatility, 3D nature and low interobserver variability.

Besides transcatheter MVR, MV replacement will be an important alternative therapy for high risk patients with MV disease in the future. Several prostheses are under preclinical evaluation or have already witnessed their first-in-human implantation [21]. For planning of these procedures, as for TAVI procedures, CT will be a very important imaging tool.

In conclusion, preoperative measured length of the distance between postero-medial and antero-lateral commissure adequately predicted the necessary length of the Cardioband™ to be implanted as shown by the gross examination after explantation of the hearts. Postoperative CT showed the intentionally cinched and released Cardioband™ a little shorter than measured after explantation. This might be explained by the “floppy” character of the heart after explantation: The Cardioband™ then expands to its initial length but not in the beating heart.

In conclusion, transvenous implantation of a Cardioband™ at the posterior mitral annulus is feasible in an acute animal model. CT visualization and measurement of the mitral valve annulus dimensions can become the imaging method of choice for procedure planning before implantation of a Cardioband™ or other transcatheter devices that are already available or will be available in the future.

Acknowledgments We want to thank Tal Sheps (Valtech Cardio) for his support and valuable input in this study.

Conflict of interest Volkmar Falk and Francesco Maisano are consultants for Valtech Cardio.

References

1. Seeburger J, Borger MA, Falk V, Kuntze T, Czesla M, Walther T, Doll N, Mohr FW (2008) Minimal invasive mitral valve repair for mitral regurgitation: results of 1339 consecutive patients. Eur J Cardiothorac Surg 34:760–765
2. Authors/Task Force Members, Vahanian A, Alfieri O, Andreotti F, Antunes MJ, Barón-Esquivias G, Baumgartner H, Borger MA, Carrel TP, De Bonis M, Evangelista A, Falk V, Lung B, Lancellotti P, Pierard L, Price S, Schäfers HJ, Schuler G, Stepinska J, Swedberg K, Takkenberg J, Von Oppell UO, Windecker S, Zamorano JL, Zembala M (2012) Guidelines on the

- management of valvular heart disease (version 2012): The Joint Task Force on the Management of Valvular Heart Disease of the European Society of Cardiology (ESC) and the European Association for Cardio-Thoracic Surgery (EACTS). *Eur J Cardiothorac Surg* 42:S1–S44
3. Mirabel M, Iung B, Baron G, Messika-Zeitoun D, Détaïnt D, Vanoverschelde JL, Butchart EG, Ravaud P, Vahanian A (2007) What are the characteristics of patients with severe, symptomatic, mitral regurgitation who are denied surgery? *Eur Heart J* 28:1358–1365
 4. Maisano F, Franzen O, Baldus S, Schäfer U, Hausleiter J, Butter C, Ussia GP, Sievert H, Richardt G, Widder JD, Moccetti T, Schillinger W (2013) Percutaneous mitral valve interventions in the real world: early and 1-year results from the ACCESS-EU, a prospective, multicenter, nonrandomized post-approval study of the MitraClip therapy in Europe. *J Am Coll Cardiol* 62:1052–1061
 5. Harnek J, Webb JG, Kuck KH, Tschope C, Vahanian A, Buller CE, James SK, Tiefenbacher CP, Stone GW (2011) Transcatheter implantation of the MONARC coronary sinus device for mitral regurgitation: 1-year results from the EVOLUTION phase I study (Clinical Evaluation of the Edwards Lifesciences Percutaneous Mitral Annuloplasty System for the Treatment of Mitral Regurgitation). *JACC Cardiovasc Interv* 4:115–122
 6. Schofer J, Siminiak T, Haude M, Herrman JP, Vainer J, Wu JC, Levy WC, Mauri L, Feldman T, Kwong RY, Kaye DM, Duffy SJ, Tübler T, Degen H, Brandt MC, Van Bibber R, Goldberg S, Reuter DG, Hoppe UC (2009) Percutaneous mitral annuloplasty for functional mitral regurgitation: results of the CARILLON Mitral Annuloplasty Device European Union Study. *Circulation* 120:326–333
 7. Goel R, Witzel T, Dickens D, Takeda PA, Heuser RR (2009) The QuantumCor device for treating mitral regurgitation: an animal study. *Catheter Cardiovasc Interv* 74:43–48
 8. Maisano F, Vanermen H, Seeburger J, Mack M, Falk V, Denti P, Taramasso M, Alfieri O (2012) Direct access transcatheter mitral annuloplasty with a sutureless and adjustable device: preclinical experience. *Eur J Cardiothorac Surg* 42:524–529
 9. Morsbach F, Desbiolles L, Plass A, Leschka S, Schmidt B, Falk V, Alkadhi H, Stolzmann P (2013) Stenosis quantification in coronary CT angiography: impact of an integrated circuit detector with iterative reconstruction. *Invest Radiol* 48:32–40
 10. Baumüller S, Winklehner A, Karlo C, Goetti R, Flohr T, Russi EW, Frauenfelder T, Alkadhi H (2012) Low-dose CT of the lung: potential value of iterative reconstructions. *Eur Radiol* 22:2597–2606
 11. Ho SY (2002) Anatomy of the mitral valve. *Heart* 88(Suppl 4):5–10
 12. Gordic S, Nguyen-Kim TD, Manka R, Sündermann S, Frauenfelder T, Maisano F, Falk V, Alkadhi H (2014) Sizing the mitral annulus in healthy subjects and patients with mitral regurgitation: 2D versus 3D measurements from cardiac CT. *Int J Cardiovasc Imaging* 30(2):389–398. doi:[10.1007/s10554-013-0341-4](https://doi.org/10.1007/s10554-013-0341-4)
 13. García-Orta R, Moreno E, Vidal M, Ruiz-López F, Oyonarte JM, Lara J, Moreno T, García-Fernández MA, Azpitarte J (2007) Three-dimensional versus two-dimensional transesophageal echocardiography in mitral valve repair. *J Am Soc Echocardiogr* 20:4–12
 14. Swaans MJ, Van den Branden BJL, Van der Heyden JAS, Post MC, Rensing BJ, Eefting FD, Plokker HW, Jaarsma W (2009) Three-dimensional transoesophageal echocardiography in a patient undergoing percutaneous mitral valve repair using the edge-to-edge clip technique. *Eur J Echocardiogr* 10:982–983
 15. Hien MD, Großgasteiger M, Weymann A, Rauch H, Rosendal C (2013) Reproducibility in echocardiographic two- and three-dimensional mitral valve assessment. *Echocardiography*. doi:[10.1111/echo.12365](https://doi.org/10.1111/echo.12365)
 16. Delgado V, Tops LF, Schuijff JD, de Roos A, Brugada J, Schalij MJ, Thomas JD, Bax JJ (2009) Assessment of mitral valve anatomy and geometry with multislice computed tomography. *JACC Cardiovas Imaging* 2:556–565
 17. Sündermann SH, Gessat M, Cesarovic N, Frauenfelder T, Biaggi P, Bettex D, Falk V, Jacobs S (2013) Implantation of personalized, biocompatible mitral annuloplasty rings: feasibility study in an animal model. *Interact CardioVasc Thorac Surg* 16:417–422
 18. Wang Q, Sun W (2013) Finite element modeling of mitral valve dynamic deformation using patient-specific multi-slices computed tomography scans. *Ann Biomed Eng* 41:142–153
 19. Alkadhi H, Desbiolles L, Stolzmann P, Leschka S, Scheffel H, Plass A, Schertler T, Trindade PT, Genoni M, Cattin P, Marinck B, Frauenfelder T (2009) Mitral annular shape, size, and motion in normals and in patients with cardiomyopathy: evaluation with computed tomography. *Invest Radiol* 44:218–225
 20. Binder RK, Webb JG, Willson AB, Urena M, Hansson NC, Norgaard BL, Pibarot P, Barbanti M, Larose E, Freeman M, Dumont E, Thompson C, Wheeler M, Moss RR, Yang TH, Pasian S, Hague CJ, Nguyen G, Raju R, Toggweiler S, Min JK, Wood DA, Rodés-Cabau J, Leipsic J (2013) The impact of integration of a multidetector computed tomography annulus area sizing algorithm on outcomes of transcatheter aortic valve replacement: a prospective, multicenter, controlled trial. *J Am Coll Cardiol* 62:431–438
 21. De Backer O, Piazza N, Banai S, Lutter G, Maisano F, Herrmann HC, Franzen OW, Søndergaard L (2014) Percutaneous transcatheter mitral valve replacement: an overview of devices in preclinical and early clinical evaluation. *Circ Cardiovasc Interv* 7:400–409

2.3 Simulation der Implantation von Transkatheter-Aortenklappenprothesen in CT-basierte Modelle der Aortenwurzel

Sündermann SH, Gessat M, Maier W, Kempfert J, Frauenfelder T, Nguyen TD, Maisano F, Falk V.

Simulated Prosthesis Overlay for Patient-Specific Planning of Transcatheter Aortic Valve Implantation Procedures.

Innovations (Phila) 2015 Sep-Oct;10(5):314-22.³⁵

[doi: 10.1097/IMI.0000000000000198](https://doi.org/10.1097/IMI.0000000000000198)

In dieser Studie wurde eine patientenspezifische Therapieplanung von Transkatheter-Aortenklappenimplantationen (TAVI) untersucht. Aus Planungs-CTs, welche vor jeder TAVI-Prozedur durchgeführt werden, wurden für 81 Patienten mit einer speziell dafür entwickelten Software Segmentierungen der Aortenwurzel durchgeführt. Diese patientenspezifischen Aortenwurzeln wurden dann für die Therapieplanung genutzt. Die Software ermöglichte die Auswahl und virtuelle Implantation verschiedener TAVI-Prothesen in diese. 14 Ärzte wurden als Probanden eingesetzt, um eine retrospektive Planung der bereits durchgeföhrten Implantationen durchzuführen. Den Probanden wurde die bereits segmentierte Aortenwurzel eines Patienten vorgelegt. In diese sollte jeder dann die aus seiner Sicht ideale Prothesengröße und -art virtuell implantieren. Die Probanden werteten jeweils mehrere Patienten aus, ohne das Ergebnis der wirklichen Implantation zu kennen. Auf diese Weise wurde für jeden der 81 Patienten 3 Mal eine retrospektive Planung durchgeführt. Die Ergebnisse der Auswahl der Probanden wurden dann mit den Ergebnissen der realen Implantation verglichen. Es zeigte sich, dass in der Gruppe der Patienten, für die die Probanden retrospektiv mit der Software eine kleinere Prothese ausgewählt hätten, die Rate an neuen Herzschrittmacherimplantationen bei 85% lag. Umgekehrt lag die Rate von paravalvulären Lecks bei den Patienten, für die die Probanden retrospektiv eine größere Prothese gewählt hätten, bei 66%.

Zusammenfassend konnte gezeigt werden, dass die Verwendung von CT-basierten, dreidimensionalen Modellen der Aortenwurzel zur virtuellen Implantation von TAVI-Prothesen bei der patientenspezifischen Therapieplanung von Nutzen ist und diese ergänzen und verbessern kann.

Simulated Prosthesis Overlay for Patient-Specific Planning of Transcatheter Aortic Valve Implantation Procedures

Simon H. Sündermann, MD, Michael Gessat, PhD,† Willibald Maier, MD, PhD,‡ Jörg Kempfert, MD,* Thomas Frauenfelder, MD, PhD,§ Thi D. L. Nguyen, MD,§ Francesco Maisano, MD,|| and Volkmar Falk, MD, PhD**

Objective: We tested the hypothesis that simulated three-dimensional prosthesis overlay procedure planning may support valve selection in transcatheter aortic valve implantation (TAVI) procedures.

Methods: Preoperative multidimensional computed tomography (MDCT) data sets from 81 consecutive TAVI patients were included in the study. A planning tool was developed, which semiautomatically creates a three-dimensional model of the aortic root from these data. Three-dimensional templates of the commonly used TAVI implants are spatially registered with the patient data and presented as graphic overlay. Fourteen physicians used the tool to perform retrospective planning of TAVI procedures. Results of prosthesis sizing were



Video clip is available online.

Accepted for publication August 3, 2015.

From the *Department of Cardiothoracic and Vascular Surgery, Deutsches Herzzentrum Berlin, Berlin, Germany; †Computer Vision Laboratory, Swiss Federal Institute of Technology (ETH) Zurich, Zurich, Switzerland; ‡Division of Cardiology, University Hospital Zurich, Zurich, Switzerland; §Institute for Diagnostic and Interventional Radiology, University Hospital Zurich, Zurich, Switzerland; and ||Division of Cardiovascular Surgery, University Hospital Zurich, Zurich, Switzerland.

Simon H. Sündermann, MD and Michael Gessat, PhD, contributed equally to this study.

A video clip is available for this article. Direct URL citations appear in the printed text and are provided in the HTML and PDF versions of this article on the journal's Web site (www.innovjournal.com). Please use Firefox when accessing this file.

The Division of Cardiovascular Surgery of the University Hospital Zurich holds a research grant from Koninklijke Philips Electronics NV, Amsterdam, the Netherlands. This work has been supported by the Swiss National Science Foundation and the Swiss Heart Foundation.

Disclosures: Francesco Maisano, MD, is a consultant for Abbott Vascular, Chicago, IL USA; Medtronic, Inc, Minneapolis, MN USA; St. Jude Medical, Inc, St. Paul, MN USA; and Valtech Cardio, Or Yehuda, Israel, and receives royalties from Edwards Lifesciences, Inc, Irvine, CA USA. Volkmar Falk, MD, PhD, is a consultant or on the advisory board for Medtronic, Inc, Minneapolis, MN USA, and received speaker's bureau honoraria from Edwards Lifesciences, Inc, Irvine, CA USA. Simon H. Sündermann, MD, Michael Gessat, PhD, Willibald Maier, MD, PhD, Jörg Kempfert, MD, Thomas Frauenfelder, MD, PhD, and Thi D. L. Nguyen, MD, declare no conflicts of interest.

Address correspondence and reprint requests to Simon H. Sündermann, MD, Division of Cardiothoracic and Vascular Surgery, Deutsches Herzzentrum Berlin, Augustenburger Platz 1, 13353 Berlin, Germany. E-mail: suendermann@dhzb.de.
Copyright © 2015 by the International Society for Minimally Invasive Cardiothoracic Surgery
ISSN: 1556-9845/15/1005-0314

compared with the prosthesis size used in the actually performed procedure, and the patients were accordingly divided into three groups: those with equal size (concordance with retrospective planning), oversizing (retrospective planning of a smaller prosthesis), and undersizing (retrospective planning of a larger prosthesis).

Results: In the oversizing group, 85% of the patients had new pacemaker implantation. In the undersizing group, in 66%, at least mild paravalvular leakage was observed (greater than grade 1 in one third of the cases). In 46% of the patients in the equal-size group, neither of these complications was observed.

Conclusions: Three-dimensional prosthesis overlay in MDCT-derived patient data for patient-specific planning of TAVI procedures is feasible. It may improve valve selection compared with two-dimensional MDCT planning and thus yield better outcomes.

Key Words: Heart valve, transapical approach, Computed tomography imaging, 3D modeling, Transcatheter aortic valve replacement.

(*Innovations* 2015;10:314–322)

Transcatheter aortic valve implantation (TAVI) has evolved into a routine procedure for treating aortic valve stenosis in high-risk patients.¹ Multidimensional computed tomography (MDCT) images are used for the visualization and measurement of aortic root landmarks and distances.^{2,3} Despite careful planning, paravalvular leakage⁴ and atrioventricular block⁵ remain the most frequent complications after TAVI. In this study, a newly developed prototype planning software was used.^{6,7} With this software, three-dimensional (3D) templates of the CoreValve [Medtronic, Inc, Minneapolis, MN USA (CoreValve)] and SAPIEN [Edwards Lifesciences, Inc, Irvine, CA USA (SAPIEN)] prostheses can be virtually implanted in MDCT-derived 3D aortic root models in addition to the regular two-dimensional (2D) visualization. We hypothesize that the use of these 3D TAVI prosthesis templates might improve the planning of TAVI procedures.

METHODS

Preoperative computed tomographic (CT) angiographies of 81 patients were used to acquire retrospective planning data with the 3D-template tool by 14 clinicians (8 surgeons, 3 cardiologists, 2 radiologists, 1 anesthesiologist) who participated in the study as active participants. The local authorities approved the study (KEK-ZH No. 2011–0393). Because of its

Innovations • Volume 10, Number 5, September/October 2015

retrospective character, written informed consent from the patients was not required, but the anonymization of patient data was handled very strictly.

End points were relevant paravalvular aortic insufficiency (AI, grade > 1+) and new pacemaker (PM) implantation. Postoperative transesophageal and transthoracic echocardiography reports and images from up to 3 months after intervention were used to classify paravalvular AI from 0 (no paravalvular AI) to grade 4 (severe paravalvular AI). Indications for perioperative new PM implantation were new conduction system disorders such as third-degree or advanced second-degree atrioventricular block not expected to resolve or the presence of sinus node dysfunction and documented symptomatic bradycardia in accordance with the American College of Cardiology/American Heart Association/Heart Rhythm Society recommendations for device-based therapy of cardiac rhythm abnormalities.⁸

Risk factors for the development of AI (ie, New York Heart Association class IV, absence of previous valve surgery, asymmetric calcification,⁹ and oval annulus shape⁴) and new PM implantation [ie, porcelain aorta, absence of previous aortic valve surgery,¹⁰ and preoperative right bundle branch block (RBBB)¹¹] were assessed from the medical reports of the patients.

Imaging and Preprocedural Planning

All preoperative CT examinations were performed using a second-generation, 128-slice DSCT system (Somatom Definition Flash, Siemens Healthcare, Forchheim, Germany). Iopromide 40 mL (Ultravist 300, 300 mg/mL; Bayer Schering Pharma, Berlin, Germany) was injected at a flow rate of 4 mL/s,

followed by 40-mL bolus of saline solution at the same flow rate. Bolus tracking in the ascending aorta was performed with a signal attenuation threshold of 100 Hounsfield units. A craniocaudal scan direction was chosen in all protocols. The scan ranged from the apex of the lung to the symphysis. The CT scan was started automatically based on the previous 10 heartbeats to reach the 60% R-R interval at the level of the valve.

Before the actual implantations, which were performed between January 2010 and January 2012, prosthesis selection was based on imaging as follows: the center line of the aortic root and the ascending aorta was drawn semiautomatically using dedicated software (3mensio benzslicer 4.3, Bilthoven, the Netherlands). The aortic annulus was defined by marking the three insertion points of each leaflet at the nadir of the sinus. The largest and shortest diameters and the circumference were measured.

Asymmetric calcification was regarded as present when the leaflet and annulus of one sinus visually had at least the same level of calcification as the two other sinuses together. The annulus shape was classified as oval when the longer diameter was equal to or greater than 120% of the shorter diameter.

Study-Specific Retrospective Planning With 3D TAVI Templates

Planning Software

The prototype planning software was developed as described previously.^{6,7} We used the open-source software libraries VTK and DCMTK and the open-source framework OpenMAF 2.0 as the basis for development. The planning workflow implemented in this tool is depicted in Figure 1 and can be seen in video 1, SDC, <http://links.lww.com/INNOV/A60>.

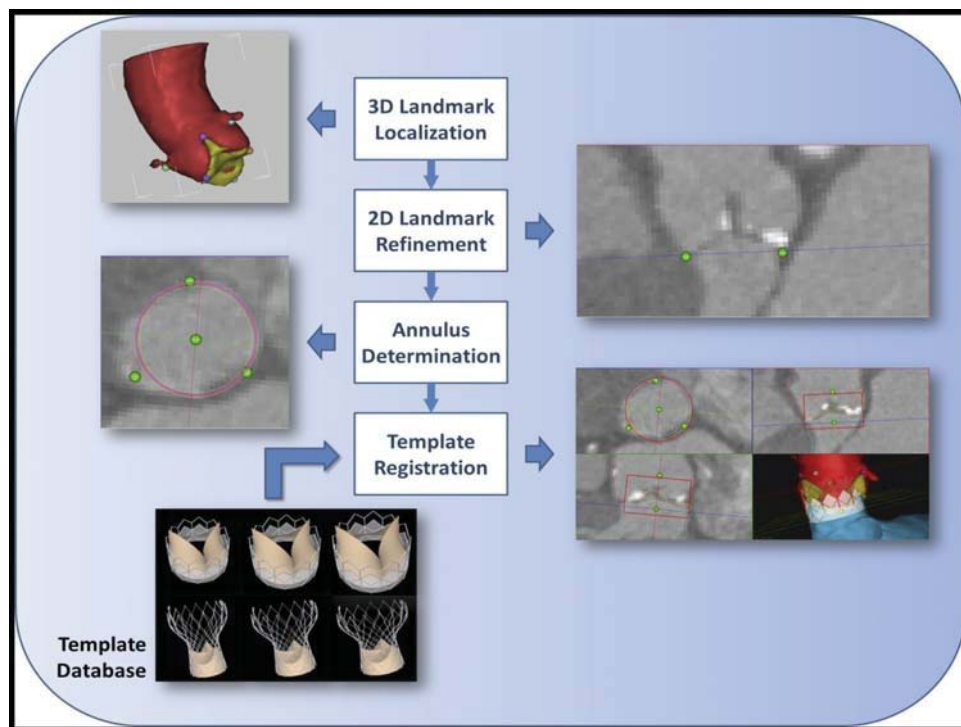


FIGURE 1. Workflow of 3D template based TAVI planning as used in the study. 3D, three dimensional; TAVI, transcatheter aortic valve implantation.

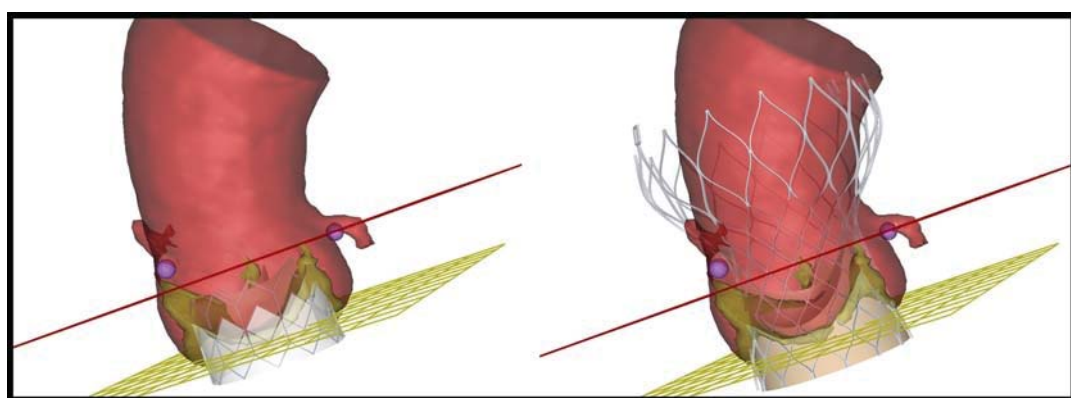


FIGURE 2. Automatically registered 3D templates representing the SAPIEN valve (Edwards Lifesciences) (left side) and CoreValve (Medtronic) (right side) prostheses. 3D, three dimensional.

Data Import

Patient MDCT images and segmentations of the aortic root, aortic valve, and left ventricle are imported from a local storage or via the network from a PACS [picture archiving and communication system] server.

Three-dimensional Landmark Localization

A 3D visualization of the segmentations is presented to the user who is prompted to localize eight landmarks on the segmented surfaces: the three nadirs of the aortic valve sinus, the three aortic valve commissures, and the two coronary ostia (00:00–00:30 in the video, SDC, <http://links.lww.com/INNOV/A60>).

Automatic Plane Computation

Three planes are computed from these landmarks: the basal or annular plane (yellow), which is defined by the three nadirs of the sinus; the commissural plane (blue) through the three commissures; and the coronary plane (red), which is parallel to the sinus plane and runs through the lower of the two ostia (right lower window in the video from 00:30, SDC, <http://links.lww.com/INNOV/A60>).

Two-dimensional Landmark Refinement

The 3D visualization allows for quick orientation and identification of the landmarks (and thereby definition of the three planes), but because of limitations in the segmentation accuracy, the selected landmarks are not 100% accurate. To improve the accuracy, the user is prompted to check and refine each landmark in a 2D cross-sectional visualization of the CT images. The system automatically offers three different triplanar sections showing all three commissures, all three sinus, or both coronary landmarks, respectively. At the press of a button the user can switch between these three views, refine the landmark positions, and thereby update the plane definitions (00:31–00:57 in the video, SCD, <http://links.lww.com/INNOV/A60>).

Annulus Sizing

After refinement and confirmation of the landmarks, a circle of best fit through the aortic annulus is computed according to the sinus landmarks and visualized in the cross-sectional view. The user may adjust the radius and the center of this circle manually (00:58–01:15 in the video, SDC, <http://links.lww.com/INNOV/A60>).

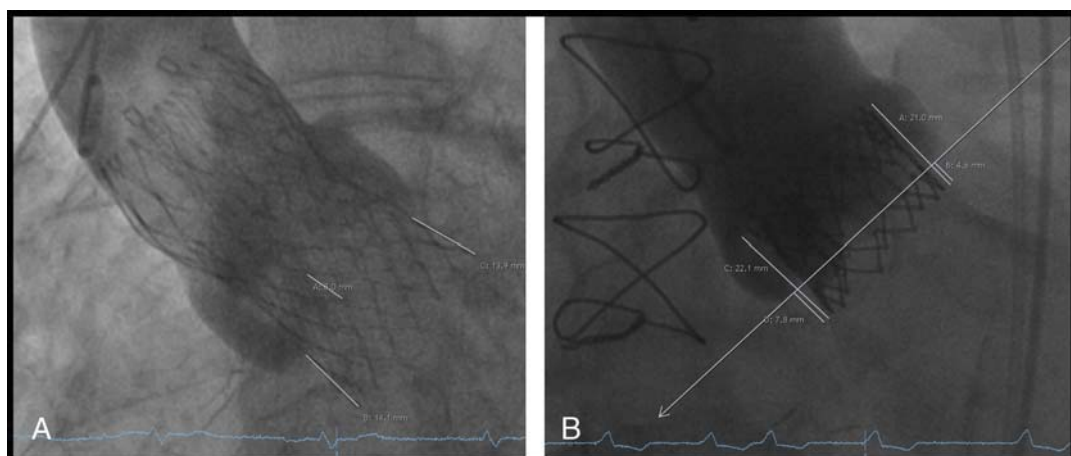


FIGURE 3. Measurement of the implantation depth of the CoreValve (Medtronic) prosthesis (left side) and the SAPIEN Valve (Edwards Lifesciences) prosthesis. The formula to calculate the part of the SAPIEN prosthesis below the annulus is as described by Nijhoff et al¹³: $[(D / C) + (B / A)] / 2 \times 100\%$.

TABLE 1. Baseline Characteristics

	Total	Equal Size	Undersizing	Oversizing	P
n	81	54	20	7	
Age, mean (SD), y	84 (6)	83 (6)	85 (4)	84 (4)	0.4
Female sex, n (%)	44 (54.3)	32 (59)	9 (45)	3 (42)	0.5
Logistic EuroSCORE, mean (SD), %	21.3 (11.8)	20.2 (9.1)	25.1 (17.9)	19.3 (7.3)	0.3
Left ventricular ejection fraction, mean (SD), %	55.1 (12.7)	56.9 (11.7)	51.8 (14.8)	50 (12.8)	0.2
NYHA class (III-IV), n (%)	59 (73)	36 (67)	18 (90)	5 (71)	0.1
Previous aortic valve surgery, n (%)	3 (3.7)	3 (5.6)	0	0	0.5
Previous CABG, n (%)	18 (22.2)	15 (28)	3 (15)	0	0.2
Coronary heart disease, n (%)	45 (55.6)	28 (52)	12 (60)	5 (71.4)	0.6
Peripheral vascular disease, n (%)	24 (29.6)	15 (27.8)	8 (40)	1 (14.3)	0.4
Previous myocardial infarction, n (%)	8 (9.9)	6 (11.1)	1 (5)	1 (14.3)	0.7
Previous PCI, n (%)	29 (35.8)	17 (31.5)	9 (45)	3 (42.9)	0.5
Previous stroke/TIA, n (%)	9 (11.1)	5 (9.3)	3 (15)	1 (14.3)	0.8
Renal failure, n (%)	34 (42)	22 (40.7)	9 (45)	3 (42.9)	0.9
COPD, n (%)	6 (7.4)	3 (5.6)	2 (10)	1 (14.3)	0.6
Pulmonary hypertension, n (%)	3 (3.7)	3 (5.6)	0	0	0.5
AF, n (%)	18 (22.2)	8 (14.8)	7 (35)	3 (42.9)	0.1
RBBB	8 (9.9)	5 (9.3)	1 (5)	2 (28.6)	0.2
LBBB	7 (8.6)	11 (6.1)	3 (15)	1 (14.3)	0.3
Peak aortic valve gradient, mean (SD), mm Hg	72.8 (22.8)	74.5 (21)	70.8 (26.8)	63.8 (27.4)	0.6
Mean aortic valve gradient, mean (SD), mm Hg	44.9 (14.6)	45.8 (13.2)	44.5 (18.2)	39.6 (15)	0.6
AVA, mean (SD), cm ²	0.7 (0.2)	0.7 (0.2)	0.7 (0.2)	0.8 (0.3)	0.3
Oval annulus	47 (58)	33 (61.1)	10 (50)	4 (57.1)	0.6
Asymmetric calcification	24 (30)	15 (27.8)	4 (20)	5 (71.4)	<0.05
Porcelain aorta	3 (3.7)	3 (5.6)	0	0	0.5

AF, atrial fibrillation; AVA, aortic valve area; CABG, coronary artery bypass grafting; COPD, chronic obstructive pulmonary disease; LBBB, left bundle branch block; NYHA, New York Heart Association; PCI, percutaneous coronary intervention; RBBB, right bundle branch block; TIA, transient ischemic attack.

Automatic Implant Template Registration

Once the annular ring is accepted, the system automatically registers 3D templates representing the SAPIEN valve (Edwards Lifesciences, Inc, Irvine, CA USA) and CoreValve (Medtronic, Inc, Minneapolis, MN USA) prostheses with the annulus (Fig. 2). The prosthesis templates are positioned perpendicular to the sinus plane at the center of the circle that was defined to mark the annulus. Implantation depth is defined such that the nadirs of the implants' leaflets are at the level of the natural nadirs of the aortic valve sinus. In the case of the SAPIEN prostheses, the vertical distance to the coronary ostia is also considered hereby. A 1-mm safety margin is maintained between the distal rim of the prostheses and the lower ostium (01:16–01:45 in the video, SDC, <http://links.lww.com/INNOV/A60>).

Implant Selection

The user may adjust the orientation and position in three dimensions of each template and choose the best-fitting template. Two-dimensional and 3D visual overlays of the CT images, anatomical models, and 3D templates were provided to allow for a visual assessment of the suitability of each of the available implant prostheses. The main criterion for selection was not a numerical (diameter) but a visual selection of the optimal match of valve size and type (01:46–3:21 in the video, SDC, <http://links.lww.com/INNOV/A60>).

The resulting selection, the final landmark positions, and the spatial registration that determines the orientation and

TABLE 2. Procedural Details; SAPIEN: SAPIEN (32 Patients) and SAPIEN XT (14 Patients)

	Total	Undersizing	Oversizing	P
n	81	20	7	—
CoreValve implantation, n (%)				
23 mm	1 (1)	1 (5)	0	—
26 mm	13 (16)	1 (5)	0	—
29 mm	20 (25)	6 (30)	5 (71)	—
31 mm	1 (1)	0	0	—
SAPIEN implantation, n (%)				
23 mm	20 (25)	5 (25)	0	—
26 mm	21 (26)	7 (35)	1 (14)	—
29 mm	5 (6)	0	1 (14)	—
Transapical access, n (%)	10 (12)	0	0	—
Postdilatation, n (%)	9 (11)	5 (25)	0	0.3
Implantation depth CoreValve, mean (SD), mm	12.2 (5.3)	12.6 (4.6)	10.4 (5.4)	0.5
Implantation depth SAPIEN, mean (SD), % of stent height	7.9 (11.5)	9 (10)	-10 (16)	0.3
Annulus rupture, n (%)	0	0	0	—
Coronary obstruction, n (%)	0	0	0	—
Peri-interventional MI, n (%)	0	0	0	—
Access site complications, n (%)	4 (5)	2 (10)	0	1
Other complications, n (%)	7 (9)	1 (5)	1 (14)	1

MI, myocardial infarction.

position of the selected valve template in relation to the coordinate system of the CT image are stored to a local hard drive or a PACS server via the network.

Each case was planned by three participants. The assignment of patients to participants was based on a semirandomized scheme, which ensured that the distribution of complications in each participant's data set matched the distribution in the complete data set. The participants had to choose the optimal size of the CoreValve and of the SAPIEN valve for each patient. Figure 2 shows the virtually implanted prostheses. Where the three observers arrived at differing results for the same patient, these results were aggregated based on a majority vote.

For each patient, the valve size selected was compared with that of the actually implanted valve. The patients were divided into three groups. Those for whom retrospective planning proposed a prosthesis smaller than actually implanted were labeled the "oversizing" group. Those where retrospectively a larger prosthesis was planned than actually implanted were the "undersizing" group. All other patients had equal sizing.

The study participants did not have access to the outcome data and did not know before or during the retrospective planning process which valve type had been implanted.

The time for the whole planning process was measured, starting with the placement of the first landmark at the segmented aorta and finishing at the final decision on prosthesis size.

Postinterventional Evaluation of Depth of Prosthesis Implantation

Deep implantation of the CoreValve prosthesis is a risk factor for permanent PM implantation after the intervention.¹² Therefore, the depth of implantation was assessed from the intraoperative angiography of the final implant position in the implant projection in left anterior oblique view.

The distance from the annulus to the lowest point of the stent was measured at both margins of the Medtronic CoreValve Revalving System (CoreValve) prosthesis from the nadir of the noncoronary sinus and the left coronary sinus, and the mean implantation depth was calculated. The height of a stent cell (8 mm) was taken as the reference structure to confirm the accuracy of the measurements.

For the SAPIEN prostheses, the part of the stent below the annulus was assessed as described by Nijhoff et al.¹³ The measurements were performed using Synedra software (version 3.3.0.12; Synedra Information Technologies GmbH, Innsbruck, Austria). Exemplary images of the measurement for both prostheses are shown in Figure 3.

Statistics

Continuous variables were calculated as means with SD. Differences in the means of continuous variables were calculated by Student *t* test or one-way analysis of variance. For static variables, χ^2 test was used to compare the groups. Logistic regression was used to calculate the association of risk factors and new PM implantation and the development of significant paravalvular insufficiency. Multivariable logistic regression modeling was performed to determine the independent predictors of new PM implantation using purposeful selection of covariates. Variables associated at univariate analysis with new PM implantation

(all with $P < 0.1$) as well as those judged to be of clinical importance from previously published literature were eligible for inclusion in the multivariable model-building process. For paravalvular leakage, no association with any of the variables was found in the univariate analysis. Therefore, no multivariate analysis was performed. A *P* value of less than 0.05 was considered significant. Data analysis was performed using IBM SPSS Statistics, version 22.0 (IBM Corporation, Armonk, NY USA).

RESULTS

Baseline Characteristics and Risk Factors

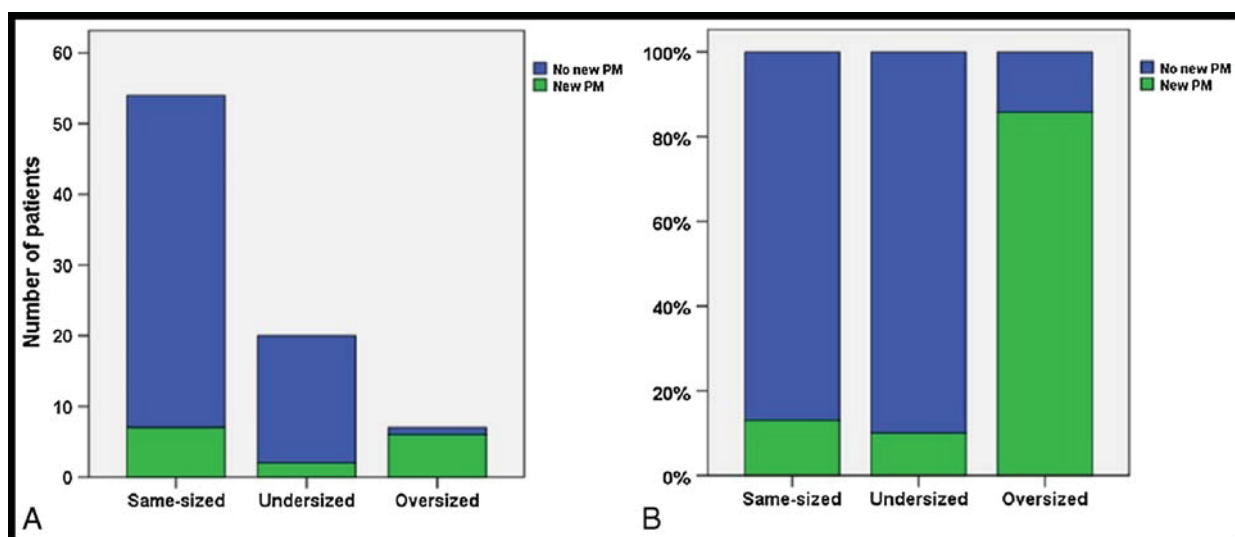
Baseline characteristics are summarized in Table 1. The number of patients who had coronary artery bypass grafting in their history was higher in the undersizing group (15% vs 0%), more patients had peripheral vascular disease in the undersizing group (40% vs 14%), previous myocardial infarction was more common in the oversizing group (14% vs 5%), and more patients showed RBBB before implantation RBBB (29% vs 5%) and asymmetric calcification (71% vs 20%) in the oversizing group. No relevant differences were seen for the other parameters.

Procedural Details

Thirty-five patients had received a CoreValve, and 46 patients had received a SAPIEN (32 patients SAPIEN, 14 patients SAPIEN XT) prosthesis (Table 2). Implantations were mainly performed by transfemoral access (87.7%). None of the patients experienced coronary obstruction or annulus rupture during the intervention or showed signs of peri-interventional myocardial infarction. Four patients had inguinal vascular access site complications, and one patient from the undersized group had a prosthesis dislocation, which ended in hemodynamic instability and finally in the death of the patient. Four patients had prosthesis embolization (one patient with CoreValve implantation from the equal-size group; one patient with CoreValve implantation from the oversizing group; one patient from the SAPIEN group, who primarily had CoreValve implantation, that embolized; and one patient from the equal-size

TABLE 3. Procedural Outcome

	Total	Undersizing	Oversizing	P
n	81	20	7	
Paravalvular leak (at least moderate), n (%)	10 (11)	7 (35)	0	0.1
SAPIEN	3 (4)	2 (10)	0	
CoreValve	7 (9)	5 (25)	0	
Paravalvular leak (at least mild), n (%)	45 (56)	17 (85)	4 (57)	0.3
New PM implantation, n (%)	14 (17)	2 (10)	6 (85)	0.001
SAPIEN	5 (6)	1 (5)	2 (29)	
CoreValve	9 (11)	1 (5)	4 (57)	
Stroke, n (%)	0	0	0	—
30-d mortality, n (%) (n = 81)	4 (4.9)	3 (15)	0	0.5
6-mo mortality, n (%) (n = 63)	6 (7.3)	4 (20)	1 (14.3)	0.5
1-y mortality, n (%) (n = 51)	7 (8.5)	5 (25)	1 (14.3)	0.3
2-y mortality, n (%) (n = 21)	7 (8.5)	5 (25)	1 (14.3)	0.3



SAPIEN group) during the implantation; all valves were replaced during the same intervention. One of these patients died 2 days after the event. Another patient had right ventricular perforation, probably caused by the temporary PM probe; sternotomy and suturing of the rupture site were necessary. All other implantations were uneventful.

The mean (SD) implantation depth of the CoreValve prostheses was 12.2 (5.3) mm [12.6 (4.6) vs 10.4 (5.4) mm for the undersizing vs the oversizing group, $P = 0.5$]. At the noncoronary sinus, the mean (SD) implantation depth was 12.4 (5.5) mm [11.7 (4.1) vs 10.7 (5) mm for the undersizing group vs the oversizing group, $P = 0.7$]. The mean (SD) implantation depth at the left coronary sinus was 11.9 (5.7) mm [13.6 (5.3) vs 11.8 (5.8) mm for the undersizing group vs the oversizing group, $P = 0.5$].

The mean (SD) implantation depth for the SAPIEN prostheses was 8.4% (11.6%) of prosthesis height below the

annulus [9% (10%) vs -10% (15.6%) for the undersizing group vs the oversizing group, $P = 0.3$].

Outcome

Mortality rate within 30 days after implantation was 4.9%, 6-month mortality was 7.3%, and 1- and 2-year mortality was 8.5%. No patient experienced stroke, 15 patients (18.5%) required a new PM, and 10 patients (12.3%) had relevant paravalvular regurgitation (grade > 1+).

Retrospective Planning

Retrospective planning resulted in 243 plans. Time needed for the retrospective planning varied between 2 and 15 minutes. A learning curve could be seen for the participants. In seven cases (9%), a smaller prosthesis and in 20 cases (24%), a larger

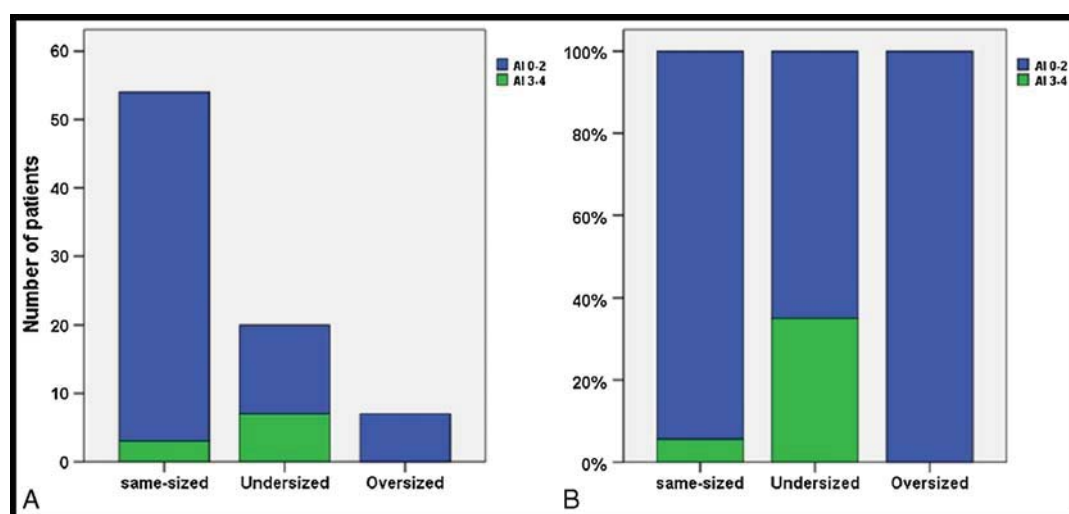


FIGURE 5. Distribution of paravalvular leakage of more than grade 2 in the equal-size, undersizing, and oversizing groups. A, The number of patients with relevant paravalvular leak in each group. B, The percentage of relevant paravalvular leak in each group. AI 0-2, no to mild paravalvular leak; AI 3-4, moderate to severe paravalvular leak. AI, aortic insufficiency.

prosthesis would have been chosen by the participants. Results are documented in Table 3.

The rate of new PM implantations was 18% in the total patient cohort. In the oversizing patient cohort, the rate of new PM implantations was much higher than in the undersizing group (85% vs 10%, $P = 0.001$). In the equal-size group, the rate of new PM implantations was 13% (Fig. 4). Sixty percent of the patients with new PM implantation had a CoreValve.

The rate of relevant paravalvular leakage was 12% in the total cohort. In the undersizing group, 35% of the patients had relevant paravalvular leakage, whereas in the oversizing group, no relevant AI was seen ($P = 0.1$). In the group with equal sizing, the rate of relevant paravalvular leakage was 5.6% (Fig. 5). Moreover, almost all patients (85%) in the undersized group showed at least mild paravalvular leakage after the procedure. Patients in the oversizing group had no or mild paravalvular AI in 57% of the cases ($P = 0.3$). In 46% of the cases in which retrospective planning resulted in equal-size choice, neither of these complications was observed.

Univariate logistic regression showed that preoperative RBBB, left bundle branch hemiblock (LBHB), and the affiliation to the sizing group were associated with the need for postinterventional new PM implantation. The results are summarized in Table 4. In the purposeful selection of covariates, LBHB was excluded. The multivariate analysis showed

TABLE 4. Results for the Univariate Logistic Regression of Potential Risk Factors Leading to Postinterventional New PM Implantation

	Odds Ratio	95% Confidence Interval	P
Sizing group	3.7	1.6–8.6	0.002
RBBB before intervention	10.5	2.2–51	0.004
Sex	1.3	0.4–4.2	0.6
EuroSCORE	1	0.9–1	0.2
Previous valve surgery	0	—	1
Previous CABG	0.2	0.03–1.7	0.1
Coronary heart disease	0.9	0.3–2.8	0.8
Previous myocardial infarction	0.6	0.07–5.3	0.6
Previous PCI	0.9	0.3–2.9	0.8
LBBB before intervention	1.9	0.3–11	0.5
LBHB before intervention	3.6	0.9–15	0.08
Atrial fibrillation	1.3	0.4–4.9	0.6
Porcelain aorta	0	—	1
Oval annulus	1	0.3–3.3	0.9
Transapical access	1.1	0.2–5.9	0.9
Valve type	0.4	0.1–1.4	0.2
Postdilatation	0	—	1
Deep implantation	1	0.3–3.5	0.9
Noncoronary sinus depth (CV)	1	0.8–1.1	0.6
Left coronary sinus depth (CV)	0.9	0.8–1	0.2
Mean depth (CV)	0.9	0.8–1.1	0.3
Mean depth (SAPIEN)	0.9	0.8–1	0.03

CV, CoreValve; LBBB, left bundle branch block; LBHB, left bundle hemiblock; PCI, percutaneous coronary intervention; RBBB, right bundle branch block.

RBBB and the affiliation to the sizing group to be independent predictors for postoperative new PM implantation ($P = 0.006$ and $P = 0.004$, respectively). The depth of implantation of CoreValve prostheses was not associated with new PM implantations. In contrast, the depth of implantation of SAPIEN prostheses was associated with new PM implantation. The patients with new PM implantations in the SAPIEN group had significantly higher implantations [10% (11%) below the annulus vs –2% (12%) below the annulus, $P = 0.01$]. For relevant paravalvular leakage, no significant association with the tested variables was found.

DISCUSSION

We used 3D TAVI prosthesis templates to investigate the hypothesis that this tool might improve the planning of TAVI procedures compared with conventional 2D MDCT measurements.

Paravalvular regurgitation is seen more frequently after TAVI than after surgical aortic valve replacement and is associated with increased late mortality.⁴ In addition, TAVI is frequently associated with new conduction defects, which result in LV asynchrony and subsequent impairment of LV function.^{14,15} Correct preoperative prosthesis selection is a crucial part of a TAVI procedure to avoid these complications.

For presurgical evaluation of valve pathology, transthoracic and transesophageal echocardiography are the criterion standards.¹⁶ For the planning of TAVI procedures, additional information is necessary because direct visualization and sizing of the valve are not possible. Echocardiographic measurement of the annulus diameter was used when TAVI was first introduced but is a less precise option than MDCT because the aortic annulus often is oval and intraobserver variability is higher than with MDCT.¹⁷ Today, commonly used measurements for decision making with regard to prosthesis selection are different geometric parameters of the aortic annulus and aortic root and the grade and location of calcification in 2D MDCT images.¹⁸

To support TAVI planning, an imaging system that uses 3D templates of the Edwards SAPIEN valve and application of this system to DynaCT images of a cohort of 31 patients were described in previous works.^{6,7} In this study, atrioventricular block and paravalvular leakage were observed in those patients where retrospective planning would have proposed a different size of prosthesis. A strong limitation of that study was the small number of patients and the fact that only one physician participated. Moreover, DynaCT is an intraoperative modality not commonly used and has been shown to be inferior to preoperative CT with regards to the accuracy of annulus dimension measurements.¹⁹

In the present study, we used an advanced version of the previously proposed planning system, with additional templates for the CoreValve. The study design was strengthened by having three independent study participants to plan each of the 81 data sets. The results showed that almost all patients who required a new PM after the intervention were in the oversizing group and almost all patients planned retrospectively for a larger prosthesis showed at least mild paravalvular leakage after the procedure. Furthermore, the rate of relevant AI was higher in the undersizing group than in the oversizing or equal-size group. None of these results reached statistical

significance. This is most probably attributable to the small number of events that can be compared.

We are aware that it can only be an assumption that the choice of a smaller size valve would not have led to paravalvular leakage and, vice versa, that the choice of a larger prostheses would have reduced the rate of new PM implantations. In addition, the majority of patients who required new PM implantation had received a CoreValve (66%). It is well-known that the rate of new conductive tissue disorders necessitating new PM is higher after CoreValve implantation than after SAPIEN implantation.^{14,20}

The mean depth of implantation of CoreValve prostheses in this series is very low compared with that in recent series,^{20,21} but no association between implantation depth and new PM implantation was found. Of course, this might be due to small sample sizes within the groups. In addition, there was no difference between the oversizing and undersizing patient groups with regard to implantation depth.

The results of this study underline the importance of planning tools. Different ways of planning a procedure can lead to different results.²² They also indicate that 3D template-based planning may be a good additional tool to prevent paravalvular leakage and new PM implantation.

Several limitations apply. This study is retrospective in character and only includes patients treated at one center. The planning was performed in a clinical setting with real patient data; nevertheless, the physicians knew that their planning decisions would not affect patient treatment. Five participants were involved in the original valve selection and implantation; because more than 6 months lay between treatment and retrospective planning for the study, the bias generated by that involvement was regarded as negligible but cannot be excluded completely. Probably the main limitation of the study concerns the CoreValve group: the average depth of implantation is much deeper than the depth considered best practice today. This reflects an early learning curve and may have influenced the outcomes of the study. One consequence could be the low positive predictive value of concordant sizing. In the equal-size group, only approximately half of the patients were free from either new PM implantation or paravalvular leak. This also shows that besides sizing other factors such as the implantation technique and anatomic factors (calcification, left ventricular outflow tract geometry, aortic angulation) play a major role.

CONCLUSIONS

The use of 3D prosthesis templates for the planning of TAVI procedures is feasible. The ability to visually assess the fit of an implant with the individual patient's anatomy helps physicians in determining the optimal implant size and position and might provide an additional tool to improve planning of TAVI procedures so as to prevent paravalvular leakage and new PM implantation. A more contemporary prospective randomized trial is needed to overcome the limitations of this study and to clearly show the positive impact of 3D template-based procedure planning.

ACKNOWLEDGMENTS

The authors thank the following colleagues for their contribution to this study as participants: Mani Arsalan, MD,

Johannes Blumenstein, MD, Won-Keun Kim, MD, Arnaud Van Linden, MD, from the Kerkhoff Klinikum Bad Nauheim, Bad Nauheim, Germany; Maximilian Emmert, MD, PhD, Christian Felix, MD, Héctor Rodriguez Cetina Biefer, MD, Lukas Altwege, MD, from the University Hospital Zurich, Zurich, Switzerland; and Jacques Scherman, from the Christian Barnard Division of Cardiothoracic Surgery, Groote Schuur Hospital, Cape Town, South Africa. The authors also thank Maurizio Taramasso for the statistical advice and Anne Gale for the editorial assistance.

REFERENCES

- Toggweiler S, Humphries KH, Lee M, et al. 5-year outcome after transcatheter aortic valve implantation. *J Am Coll Cardiol.* 2013;61:413–419.
- Gurvitch R, Webb JG, Yuan R, et al. Aortic annulus diameter determination by multidetector computed tomography: reproducibility, applicability, and implications for transcatheter aortic valve implantation. *JACC Cardiovasc Interv.* 2011;4:1235–1245.
- Achenbach S, Delgado V, Hausleiter J, Schoenhagen P, Min JK, Leipsic JA. SCCT expert consensus document on computed tomography imaging before transcatheter aortic valve implantation (TAVI)/transcatheter aortic valve replacement (TAVR). *J Cardiovasc Comput Tomogr.* 2012;6:366–380.
- Buzzatti N, Maisano F, Latib A, et al. Computed tomography-based evaluation of aortic annulus, prosthesis size and impact on early residual aortic regurgitation after transcatheter aortic valve implantation. *Eur J Cardiothorac Surg.* 2013;43:43–50.
- Kodali SK, Williams MR, Smith CR, et al. Two-year outcomes after transcatheter or surgical aortic-valve replacement. *N Engl J Med.* 2012;366:1686–1695.
- Gessat M, Merk DR, Falk V, et al. System for Transapical Aortic Valve Implantation. *Proceedings of SPIE Medical Imaging.* 2009;7261:E1–E12.
- Jacobs S, Gessat M, Walther T, Falk V. Three-dimensional template-based planning for transapical aortic valve implantation. *J Thorac Cardiovasc Surg.* 2011;141:1541–1543.
- Epstein AE, DiMarco JP, Ellenbogen KA, et al. 2012 ACCF/AHA/HRS focused update incorporated into the ACCF/AHA/HRS 2008 guidelines for device-based therapy of cardiac rhythm abnormalities: a report of the American College of Cardiology Foundation/American Heart Association Task Force on Practice Guidelines and the Heart Rhythm Society. *Circulation.* 2013;127:e283–e352.
- Unbehauen A, Pasic M, Dreyssse S, et al. Transapical aortic valve implantation: incidence and predictors of paravalvular leakage and transvalvular regurgitation in a series of 358 patients. *J Am Coll Cardiol.* 2012;59:211–221.
- Ledwoch J, Franke J, Gerckens U, et al; German Transcatheter Aortic Valve Interventions Registry Investigators. Incidence and predictors of permanent pacemaker implantation following transcatheter aortic valve implantation: analysis from the German transcatheter aortic valve interventions registry. *Catheter Cardiovasc Interv.* 2013;82:E569–E577.
- Erkadic D, De Rosa S, Kelava A, et al. Risk for permanent pacemaker after transcatheter aortic valve implantation: a comprehensive analysis of the literature. *J Cardiovasc Electrophysiol.* 2012;23:391–397.
- Saia F, Lemos PA, Bordoni B, et al. Transcatheter aortic valve implantation with a self-expanding nitinol bioprosthetic: prediction of the need for permanent pacemaker using simple baseline and procedural characteristics. *Catheter Cardiovasc Interv.* 2012;79:712–719.
- Nijhoff F, Agostoni P, Samim M, et al. Optimisation of transcatheter aortic balloon-expandable valve deployment: the two-step inflation technique. *EuroIntervention.* 2013;9:555–563.
- Urena M, Webb JG, Tamburino C, et al. Permanent pacemaker implantation after transcatheter aortic valve implantation: impact on late clinical outcomes and left ventricular function. *Circulation.* 2014;129:1233–1243.
- Hoffmann R, Herpertz R, Lotfipour S, et al. Impact of a new conduction defect after transcatheter aortic valve implantation on left ventricular function. *JACC Cardiovasc Interv.* 2012;5:1257–1263.

16. Joint Task Force on the Management of Valvular Heart Disease of the European Society of Cardiology (ESC), European Association for Cardio-Thoracic Surgery (EACTS), Vahanian A, Alfieri O, Andreotti F, et al. Guidelines on the management of valvular heart disease (version 2012). *Eur Heart J.* 2012;33:2451–2496.
17. Jabbour A, Ismail TF, Moat N, et al. Multimodality imaging in transcatheter aortic valve implantation and post-procedural aortic regurgitation: comparison among cardiovascular magnetic resonance, cardiac computed tomography, and echocardiography. *J Am Coll Cardiol.* 2011;58:2165–2173.
18. Tzikas A, Schultz CJ, Piazza N, et al. Assessment of the aortic annulus by multislice computed tomography, contrast aortography, and trans-thoracic echocardiography in patients referred for transcatheter aortic valve implantation. *Catheter Cardiovasc Interv.* 2011;77:868–875.
19. Lehmkohl LH, von Aspern K, Foldyna B, et al. Comparison of aortic root measurements in patients undergoing transapical aortic valve implantation (TA-AVI) using three-dimensional rotational angiography (3D-RA) and multislice computed tomography (MSCT): differences and variability. *Int J Cardiovasc Imaging.* 2013;29:417–424.
20. Khawaja MZ, Rajani R, Cook A, et al. Permanent pacemaker insertion after CoreValve transcatheter aortic valve implantation: incidence and contributing factors (the UK CoreValve Collaborative). *Circulation.* 2011; 123:951–960.
21. Tchetche D, Modine T, Farah B, et al. Update on the need for a permanent pacemaker after transcatheter aortic valve implantation using the CoreValve® Accutrap™ system. *EuroIntervention.* 2012;8:556–562.
22. Kempfert J, Van Linden A, Lehmkohl L, et al. Aortic annulus sizing: echocardiographic versus computed tomography derived measurements in comparison with direct surgical sizing. *Eur J Cardiothorac Surg.* 2012; 42:627–633.

CLINICAL PERSPECTIVE

This is an excellent report describing a planning tool for transcatheter aortic valve implantation (TAVI) using a three-dimensional model of the aortic root created from a data set obtained by preoperative multidimensional computer tomography. The authors looked at 81 consecutive patients and retrospectively used this tool to plan the TAVI procedure. They compared the prosthesis sizing obtained with this planning tool to the prosthesis size used in the actually performed procedure. In the group of patients in which there was actual oversizing (retrospective planning predicted a smaller prosthesis), 85% of the patients had new pacemaker implantation. In the patients in which there was undersizing in the actual procedure, the majority had at least a mild paravalvular leak. In the 46% of patients in which the prosthesis used matched that recommended by the planning tool, neither of these complications were observed.

This type of simulation is an important advance, and planning tools such as this one have the potential to greatly refine implantation techniques. This group is to be congratulated for their beautiful work. The ability to visually assess the fit of an implant with the actual patient's anatomy could limit procedural complications. Future prospective studies from this group and others will continue to define the role of simulated procedural planning in improving TAVI outcomes.

2.4 Verwendung von Stent Maps zur Vorhersage von Komplikationen bei Transkatheter-Aortenklappenimplantationen

Born S, Sündermann SH, Russ C, Hopf R, Ruiz CE, Falk V, Gessat M.
Stent Maps – Comparative Visualization for the Prediction of Adverse Events of Transcatheter Aortic Valve Implantations.

IEEE Trans Vis Comput Graph 2014;20(12):2704-2713³⁶

[doi: 10.1109/TVCG.2014.2346459](https://doi.org/10.1109/TVCG.2014.2346459)

In dieser Studie wurde untersucht, ob es möglich ist, anhand sogenannter Stent Maps Komplikationen von TAVI-Prozeduren vorherzusagen. Eine Stent Map ist eine zweidimensionale Visualisierung des Stents einer TAVI-Prothese. Die Fläche der Stent Map entspricht der Oberfläche des implantierten Stents der Prothese, welcher virtuell gestreckt wurde. Die korrespondierenden anatomischen Strukturen wie Taschen der Aortenklappe und Koronarostien wurden ebenfalls mit auf die Stent Map aufgetragen. Anhand der Stent-Deformation wurde eine mechanische Analyse der Radialkräfte durchgeführt. Die Radialkräfte wurden wie in einer Heat Map in die Stent Map übertragen. Dadurch konnte die Kraftverteilung entlang des kompletten Stents visuell dargestellt werden. Außerdem wurde die Verteilung der Kalzifikation in der Aortenwurzel aufgetragen. Stent Maps wurden für 30 Patientendatensätze angefertigt. Die Hälfte der Patienten hatten in verschiedener Ausprägung ein paravalvuläres Leck. Tatsächlich konnten unterschiedliche Muster für verschiedene Ausprägungen der paravalvulären Insuffizienz identifiziert werden. Die Stent Maps wurden außerdem klinischen Experten vorgelegt, um die potentielle Nützlichkeit in der Routineplanung zu evaluieren. Nach einer gewissen Gewöhnungsphase wurde die Darstellung als hilfreich empfunden. Limitierend war die geringe Anzahl an Patienten. Denkbar wäre zum Beispiel die Erstellung einer sehr großen Anzahl an Patienten, um eine Art Mustererkennung zu erreichen, welche dann im Umkehrschluss präoperativ Aussagen über das Auftreten von Komplikationen zulassen könnten. Die Stent Maps ermöglichten somit eine einheitliche, vereinfachte, zweidimensionale Darstellung komplexer dreidimensionaler Strukturen und somit eine patientenspezifische Therapieplanung.

Stent maps – Comparative visualization for the prediction of adverse events of transcatheter aortic valve implantations

Silvia Born, Simon H. Sündermann, Christoph Russ, *Student Member, IEEE*, Raoul Hopf, Carlos E. Ruiz, Volkmar Falk, and Michael Gessat

Abstract— Transcatheter aortic valve implantation (TAVI) is a minimally-invasive method for the treatment of aortic valve stenosis in patients with high surgical risk. Despite the success of TAVI, side effects such as paravalvular leakages can occur postoperatively. The goal of this project is to quantitatively analyze the co-occurrence of this complication and several potential risk factors such as stent shape after implantation, implantation height, amount and distribution of calcifications, and contact forces between stent and surrounding structure. In this paper, we present a two-dimensional visualization (stent maps), which allows (1) to comprehensively display all these aspects from CT data and mechanical simulation results and (2) to compare different datasets to identify patterns that are typical for adverse effects. The area of a stent map represents the surface area of the implanted stent – virtually straightened and uncoiled. Several properties of interest, like radial forces or stent compression, are displayed in this stent map in a heatmap-like fashion. Important anatomical landmarks and calcifications are plotted to show their spatial relation to the stent and possible correlations with the color-coded parameters. To provide comparability, the maps of different patient datasets are spatially adjusted according to a corresponding anatomical landmark. Also, stent maps summarizing the characteristics of different populations (e.g. with or without side effects) can be generated.

Up to this point several interesting patterns have been observed with our technique, which remained hidden when examining the raw CT data or 3D visualizations of the same data. One example are obvious radial force maxima between the right and non-coronary valve leaflet occurring mainly in cases without leakages. These observations confirm the usefulness of our approach and give starting points for new hypotheses and further analyses. Because of its reduced dimensionality, the stent map data is an appropriate input for statistical group evaluation and machine learning methods.

Index Terms—Comparative visualization, medical visualization, vessel flattening, transcatheter aortic valve implantation (TAVI)

1 INTRODUCTION

The aortic valve is located between the left cardiac ventricle and the aorta (see Fig. 1). Its function is to open when the blood is ejected from the ventricle into the aorta during systole and to avoid the backflow of blood into the ventricle during the remainder of the heart cycle (diastole). Stenosis of the aortic valve, due to calcified and stiffened valve leaflets, is the most common heart valve disease in the western countries. It is problematic for several reasons and needs to be treated (see Sec. 3).

The treatment of choice is the surgical implantation of a prosthetic aortic valve. An alternative to open surgery is a minimally-invasive approach, the *transcatheter aortic valve implantation (TAVI)*, where the pathologically altered valve is not replaced surgically but displaced

towards the aortic wall by an expanded stent containing a prosthetic aortic valve (see Fig. 2c).

Especially for high-risk patients this approach is a valid and reasonable alternative to conventional cardiac surgery. However, postoperatively paravalvular leakages (PVL) may occur. PVL is the backflow of blood between the stent and its surrounding structures into the left cardiac ventricle leading to a volume overload and potential dilation of this heart chamber. Occurrence of PVL has been demonstrated to have relevant impact on the survival of patients treated by TAVI [17].

Clinical science has identified different risk factors and predictors for the onset of PVL after TAVI. These theories consider, e.g., the influence of stent deformation, radial attachment forces, or calcifications (see Sec. 3). What still remains unclear is how important these risk factors are for a specific patient, how they interact and which combination of valve type, size, and position could minimize the risk for PVL. The long-term goal of this project is to improve the preoperative planning of TAVI procedures with biomechanical tools that allow to predict the risk of PVL and other complications for specific cases and support the interventionalist in choosing the most appropriate advancement. For this, we are developing a simulation system, which allows to virtually conduct the aortic valve implantation based on the patient's preoperative CT data and calculate the displacement of tissues and calcifications, the deformation of the stent, and the radial forces between these structures [25].

However, predicting displacements, deformity, and forces remains a fully academic research problem as long as we are not able to actually derive clinically useful information from that data. Useful would be, e.g., an odds ratio for a complication to occur under a given configuration or, one step further, an algorithm that searches for a configuration (e.g., stent type and size and ideal implantation position) that minimizes this odds ratio for a given patient. In order to develop this odds ratio, we need to learn, which parameters or parameter combinations indicate PVL. For this, we analyze postoperative CT data with known outcome as a first step before we can apply our findings to preoperative simulation results in the future. For both use cases, a comprehensive presentation of the high-dimensional anatomical and simulation data is needed.

- *Silvia Born is with the University of Zurich, Switzerland, Hybrid Laboratory for Cardiovascular Technologies. E-mail: silvia.born@uzh.ch.*
- *Simon H. Sündermann is with the University Hospital of Zurich, Switzerland, Division of Cardiovascular Surgery. E-mail: simon.suendermann@usz.ch.*
- *Christoph Russ is with the Swiss Federal Institute of Technology (ETH) Zurich, Switzerland, Computer Vision Laboratory. E-mail: russc@ethz.ch.*
- *Raoul Hopf is with the Swiss Federal Institute of Technology (ETH) Zurich, Switzerland, Institute of Mechanical Systems. E-mail: hopf@imes.mavt.ethz.ch.*
- *Carlos E. Ruiz is with the Lenox Hill Hospital, Structural and Congenital Heart Division. E-mail: cruz@nshs.edu.*
- *Volkmar Falk is with the University Hospital of Zurich, Switzerland, Division of Cardiovascular Surgery. E-mail: volkmar.falk@usz.ch.*
- *Michael Gessat is with the University of Zurich, Switzerland, Hybrid Laboratory for Cardiovascular Technologies and the Swiss Federal Institute of Technology (ETH) Zurich, Switzerland, Computer Vision Laboratory. E-mail: mgessat@ethz.ch.*

Manuscript received 31 Mar. 2014; accepted 1 Aug. 2014. Date of publication 11 Aug. 2014; date of current version 9 Nov. 2014. For information on obtaining reprints of this article, please send e-mail to: tvcg@computer.org.
Digital Object Identifier 10.1109/TVCG.2014.2346459

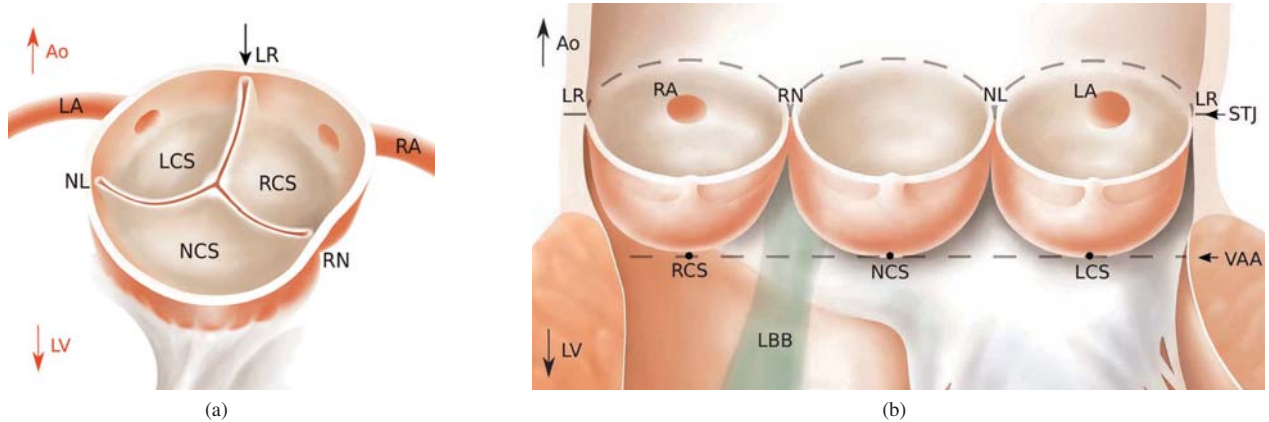


Fig. 1. (a) Healthy tricuspid aortic valve anatomy. (b) Left ventricular outflow tract cut open to show more clearly the three cusps (left coronary, right coronary, non-coronary; named according to the respective ostie located nearby). Abbreviations: Left coronary artery (LA), right coronary artery (RA), left coronary sinus (LCS), right coronary sinus (RCS), non-coronary sinus (NCS), commissure between the respective sinuses (NL, RN, LR), sinotubular junction (STJ), virtual aortic annulus (VAA), left ventricle (LV), aorta (Ao), left bundle branch (LBB).

In this paper, we aim at a visualization approach that incorporates all relevant information and allows users to find patterns indicating PVL. For this, we reduce the dimensionality of the morphological and simulation data and create comprehensive 2D plots. Further, we show how comparison and aggregation of data across individuals in a population or sub-groups of a population can be performed in a straightforward manner. We apply the presented approaches to data from a small cohort of clinical TAVI cases and collect feedback from clinical experts.

2 RELATED WORK

Prediction of TAVI through means of mechanical simulation has been investigated previously – among others – by [3, 6, 25, 30]. They have focused their work on mechanical prediction of stent deployment but have discussed its significance for early detection of PVL and other complications. Lately even a commercial tool has been announced to bring TAVI simulations into the clinics [8]. However, there is still a lack of available methods to evaluate such mechanical simulations and to study and understand the clinical relevance of the produced results for the prediction of potential side effects. Common ways of displaying simulation data are 3D renderings with color-coded radial forces, stress values etc. (see an example in Fig. 3). These visualizations are valid to illustrate specific aspects of single datasets but are inappropriate to efficiently evaluate and compare cases of a larger database. To close this gap, we suggest our stent maps method, which reduces data dimensionality, allows quicker overview and comparison of data, and lays the foundation for a computational evaluation.

Several examples in the medical community demonstrate that methods that reformat and reduce data can lead to useful tools. The learning curve for the user is usually longer for these tools but when established they save time when compared to the examination of raw CT data or 3D scenes. An important example in this context is the bull's eye plot, which maps the three-dimensional surface of the left cardiac ventricle onto a two-dimensional polar plot. It consists of concentric circles where the innermost circle represents the heart's apex and the outermost represents the heart base. On these bull's eye plots 3D image information can be encoded for a quick investigation of the data. This avoids tedious scrolling through 3D image data and decreases intra- and interobserver variability. Nowadays, bull's eye plots are used in various applications, e.g., in the coronary artery disease diagnostics to compare perfusion of the heart during stress and rest [18, 19] or to analyze strain rate changes (gained from speckle 3D echocardiography) to examine, e.g., ischemia [11]. Termeer et al. proposed a volumetric bull's eye plot. By adding a third dimension to this plot, the ventricle's wall thickness can be encoded as additional information [28]. Neugebauer et al. introduced a visualization method where the re-

duction from 3D to 2D helps explore scalar parameters on cerebral aneurysm walls. For this, they combined 3D visualizations of cerebral aneurysms with several 2D maps showing the aneurysm from different view points and provided tools allowing users to correlate between the two depictions [21].

A second group of examples deals with the flattening of tubular anatomical structures. Huysman et al. introduced a generic method to parametrize tubular surfaces onto (flattened) cylinders [15]. Related to this, we also transfer our scene (however consisting of several isolated objects around a common center line) onto a cylinder with generalized cylindrical coordinates. With curved planar reconstruction, e.g., a 3D image dataset is transformed so that a bent vessel is visible in one plane for an easier overview during diagnosis [16, 20]. Flattening is also possible with segmented vessels based on their surface representations [2, 31]. Both methods are especially challenging for bifurcating structures. Ropinski et al. [24] and Diepenbrock et al. [7] used vessel flattening by circular projections for the multimodal, comparative visualization of PET/CT data and Angelelli et al. [1] applied flattening of the aorta to allow for a side-by-side visualization of streamlines from 4D MRI blood flow data. Finally, the flattening of CT colon data was developed to help clinicians find polyps [5, 13].

Along these lines, we apply a novel flattening and reduction approach to multimodal data of the aortic valve and the prosthesis.

3 MEDICAL BACKGROUND

3.1 Aortic valve anatomy

The aortic valve is located in the aortic root at the border between the left cardiac ventricle (LV) and the aorta. It separates the blood pools of these two structures and opens during systole when blood is ejected from the LV into the aorta. The valve is tricuspid, which means that it consists of three semilunar leaflets (cusps) as shown in Figure 1a. The *commissures* mark the border between the three leaflets of the aortic valve and the three sinuses. The right coronary artery (RA) and the left coronary artery (LA), which supply the heart muscle with blood, originate from the corresponding sinuses (right coronary sinus, RCS; left coronary sinus, LCS). One sinus does not contain a coronary artery exit and is called non-coronary sinus (NCS). In this paper, LCS, RCS, and NCS describe the lowest points of the corresponding sinuses (black points in Fig. 1b). The plane defined by these three landmarks is the *virtual aortic annulus* (VAA) whereas the plane defined by the three commissures is called *sinotubular junction* (STJ). These two planes together with the border of the sinuses connecting the commissures and the lowest points of the sinuses is shaped like a crown. Figure 1b shows the anatomical situation of the aortic valve when cut open at the commissure between left and right coronary sinus (LR-

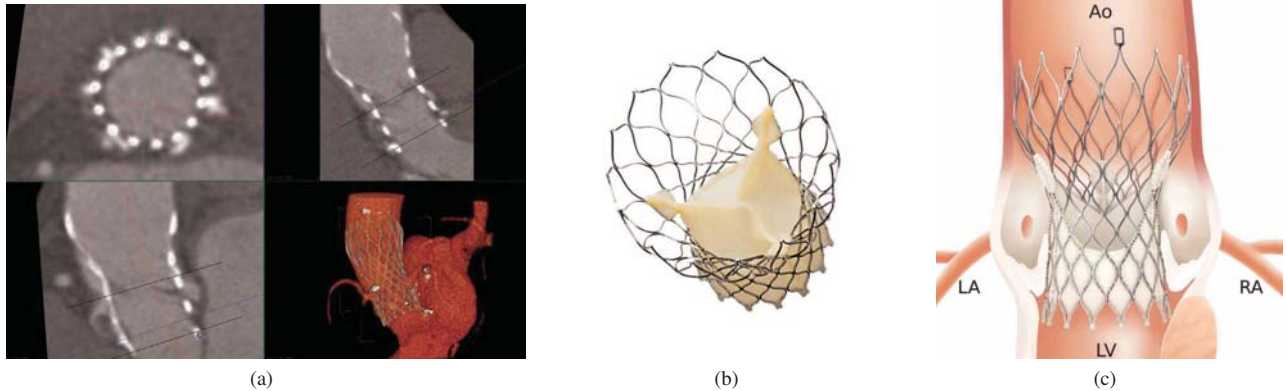


Fig. 2. (a) Postoperative CT data showing the inserted stent as cross-section and longitudinal section in the 2D slices and in a 3D volume rendering. (b) Self-expandable stent as used in the TAVI cases of this paper. The stent contains a tricuspid prosthetic aortic valve made of porcine tissue. The interventionalist can choose from four diameters (23 mm, 26 mm, 29 mm, or 31 mm) depending on the patient's aortic root size. (c) A correctly positioned CoreValve stent in the aortic root (usually the stent is more deformed). Both, a very high and a very low implantation height is suspected to cause leakages. Abbreviations: Left coronary artery (LA), right coronary artery (RA), left ventricle (LV), aorta (Ao).

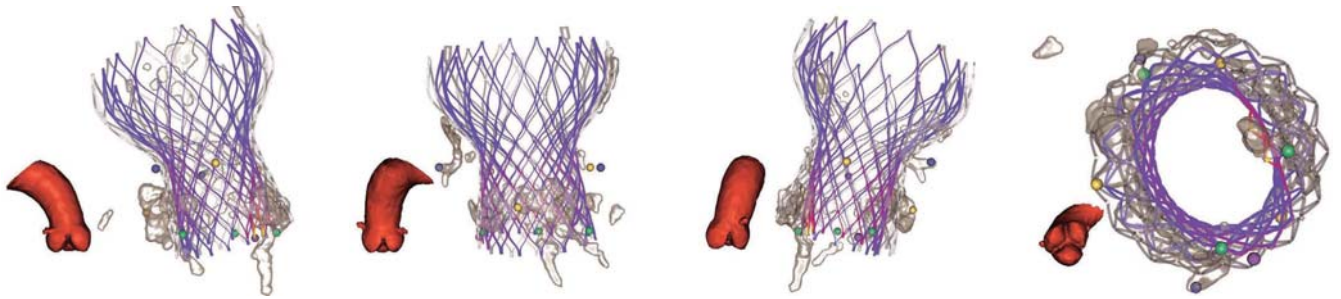


Fig. 3. Conventional visualization of the data in Figure 5b, shows the implanted stent (with radial forces overlay), original stent (gray), calcium (transparent gray), and landmarks (commissures in yellow, sinuses in green, coronary arteries in blue). The first three images show views directed on the commissures (from left to right: NL-commissure, LR-commissure, RN-commissure) and the VAA plane kept horizontally (i.e. sinuses are always displayed in one line). The right image presents the view from below on the VAA plane.

commissure; the other commissures are named RN-commissure and NL-commissure accordingly). This is the view that we have chosen for our stent maps.

3.2 TAVI in a nutshell

The underlying pathological mechanisms of aortic valve stenosis results from a narrowing of the valve due to calcified leaflets. This implies that the blood has to be ejected against increased resistance. Additionally, abnormal high-velocity jets occur, which favor aneurysm development [4]. Aortic regurgitation can occur accompanying due to an insufficient closure of the leaflets. As a consequence, the blood pressure in the left heart and the lungs increases, causing a thickening and stiffening of the heart muscle [22]. Resulting symptoms are shortness of breath and chest pain.

The standard treatment for aortic valve stenosis according to actual guidelines [29] is the surgical implantation of a prosthetic aortic valve (example shown in Fig. 2b) necessitating the use of a cardio-pulmonary bypass machine (CPB) and temporary cardiac arrest. Since 2002, a minimally-invasive alternative, the *transcatheter aortic valve implantation* (TAVI) exists. Instead of open surgery, the pathological aortic valve is approached with a catheter either via the aorta (retrograde) through access in the groin or via the left cardiac ventricle (anterograde) through the apex of the heart. A stent containing the prosthetic aortic valve is inserted, positioned, and released. The stent (which is either self-expandable or expanded with a balloon) pushes the degenerated native aortic valve against the aortic annulus, the prosthetic valve is unfolded, and takes over the valve function (see Fig. 2c). During this procedure, the interventionalist navigates in the heart by

means of transesophageal echocardiography (TEE) and CT angiography.

In the last eleven years, about 50.000 TAVI procedures were performed in more than 40 countries [23]. However, postoperative complications such as left bundle branch block (LBBB; may lead to cardiac arrhythmia) and transvalvular and paravalvular leakages are described [17]. In this paper we mainly address paravalvular leakages (PVL) describing the backflow of blood between the aortic wall/aortic annulus and the stent into the left cardiac ventricle during diastole. Five severity codes are distinguished: none, trivial, mild, moderate, and severe PVL [23].

PVL occurs when the stent does not completely attach to the surrounding structures leaving gaps for paravalvular blood flow. Several causes for an incomplete attachment are conceivable: (1) stent diameter too small for the patient's aortic annulus, (2) stent implanted too high so that blood flows past the prosthetic aortic valve through the stent, (3) stent implanted too low, which is problematic since the diameter at the stent's neck is smaller, (4) aortic valve stent not fully expanded, (5) amount and uneven distribution of calcifications located in the gap between stent and aortic wall.

In severe PVL cases, usually one of the following therapies is chosen: a further dilatation of the valve prosthesis with a balloon, the closing of the leakage hole with an occluder device or – if the valve prosthesis is implanted too low – the treatment with a second, higher implanted prosthesis (valve-in-valve) [27]. Since TAVI patients are mainly high-risk patients, each of these additional interventions is avoided if possible. Therefore, weaker PVL are usually not directly treated but closely monitored. Still, a higher one-year mortality has

been shown even with non-severe PVL [26]. The long-term goal of our project is to help prevent PVL by simulating TAVI procedures pre-operatively and giving the interventionalist advice on the best configuration regarding valve type and positioning. The intermediate goal is to be able to interpret simulation results and use them to predict PVL risks.

4 METHODS

In this paper, we present a visualization approach that incorporates relevant information about stent shape, radial forces, calcifications, anatomical situation etc. in a comprehensive 2D map representing the unrolled 3D scene. Without the necessity for an animated, interactive visualization of a 3D model on a computer screen, it allows to easily grasp the anatomy of the aortic valve, its spatial relation to the stent, and the amount and distribution of calcifications at one glance.

4.1 Requirements and design choices

To be useful for medical research, our visualization needs to meet the following requirements: First, it should communicate important *spatial relationships*. More specifically, it should clearly depict the patient's individual anatomy of the aortic root (the shape of three sinuses/cusps, position of left and right coronary arteries), the amount and positions of calcium on the aortic valve, and the shape and relative position of the stent in the aortic root. Second, our system should display *multiple quantitative parameters*, such as the estimated radial forces, stent compression, and calcium thickness. Third, it should allow an *easy comparison of several datasets* in order to allow to identify patterns typical for cohorts with or without postoperative PVL. And fourth, the visualization approach should provide the basis for further *statistical analyses* and computational pattern matching.

To meet the requirements regarding comparability, we chose to transform the 3D data into 2D side-by-side visualizations (*stent map*) by virtually flattening the data. As an alternative approach, we considered connected 3D renderings of the different stent datasets, which would provide users with corresponding views on the different datasets while navigating. However, navigation is always necessary to view the important spatial aspects of the data, which makes it more difficult and time-consuming to get an overview. For this reason, we preferred the 2D version.

The area of the 2D map covers the area of the straightened and uncoiled stent. The map's vertical axis corresponds to the (bent) centerline of the stent and the map's horizontal axis corresponds to the angle around the centerline, like in a cylindrical coordinate system. The map itself is designed similar to a heatmap, i.e., it is constructed of tiles showing a quantitative property by color. Each tile contains the specific information of a 3D segment as seen from the stent's centerline. By arranging several maps side-by-side, we fulfill the requirement to show multiple parameters. Here, we considered the alternative to display more than one quantitative parameter per map by color-mixing or by encoding more than one property per tile with an approach as shown in [12]. However, we chose the side-by-side version, since a complex encoding strategy would decrease comprehensibility and complicate pattern identification for the users. A redesign in this regard might be useful as soon as the relevant properties are identified and it is clear what users must be looking for in these maps.

Finally, we communicate spatial relationships and important anatomical information with graphical markups that are drawn on the map, similar to the borders between countries on a geographical map. The following structures are depicted by these markups: (1) the shape of the aortic valve and the ostia of the coronary arteries from the aortic root, (2) the contours of the calcifications as segmented from the CT data, and (3) the stent contours. These stent contours together with the color-coded stent distortion (see Sec. 4.3.2) display the necessary information about the stent shape.

4.2 Data preprocessing and mechanical analysis

The process of postoperative CT image acquisition, the method for extracting information about the postoperative stent shape from these images and how that information is used in a mechanical analysis to

create an estimate of the radial forces between the stent and the surrounding tissues and calcifications is presented in [9] and [10]. Here, we confine ourselves to a brief overview over these techniques, and refer the reader to the cited papers for further detail.

We obtained CT images (see Fig. 2a) from patients who had received a self-expandable TAVI prosthesis (see Fig. 2b). A set of landmarks is automatically extracted from those images, which represent the intersection points, or grid points, of the stent's mesh structure, using some diligence to separate the stent from the surrounding calcifications, which show a similar intensity in the images. A mechanical model of the stent in its original (undeformed) shape was created from microCT scans of the device and a method for using the grid points extracted from the patient images as soft kinematic constraints was developed [14]. In [10] we describe, how this method is used to simultaneously reduce point localization errors that occur during the localization of the grid points and to extract estimates for the radial force between the stent and its surroundings. The basic idea here is to derive the radial forces from the deformation of the implanted stent when compared to the relaxed stent shape.

For the presented approach, two additional manual processing steps were added to the pipeline as described in [10]: (1) With an expert clinician, six anatomical landmarks at the aortic annulus (the three commissures and the three sinuses) as well as the approximate position of the left and right coronary arteries were marked manually in the CT images (see Fig. 2a). (2) After subtracting the, now known, stent from the CT images, the remaining high-intensity voxels near the aortic root are considered calcium. Morphological operators are employed to erase very small bits of calcium (by morphological opening) and to close very small holes in larger chunks of calcium (by morphological closing) before computing surface models of the calcifications.

4.3 Map creation

After the previously described preprocessing steps, the relevant data are available as geometric meshes of stent (containing the radial force value for each vertex) and calcium as well as the eight anatomical landmark positions. In the following, the separate steps of map generation are described in more detail.

4.3.1 Generalized cylindrical coordinates

The area of the stent map corresponds to the area of the straightened and unrolled stent (seen from the inside). Thus, to draw the map, the mesh positions and its parameters need to be assigned to the respective map locations. This can be considered as a cylindrical mapping based on a curved cylinder around the stent. As a first step and in order to facilitate this mapping, we transform our 3D scene from cartesian to the stent's cylindrical coordinates. For this, we generate the stent model's centerline and determine for each vertex in the scene the cylindrical coordinates with respect to this centerline. More specifically, in its undeformed shape, the stent can be very well described in cylinder coordinates defined around its central axis. To allow for a similar representation in a deformed shape, where the centerline of the stent can be (slightly) bent, we rely on a *generalized definition of cylindrical coordinates* (see Fig. 4b):

For a given, not necessarily straight, C^1 -smooth curve $\mathbf{c} : [a, b] \rightarrow \mathbb{R}^3$ and a reference point $\mathbf{q} \in \mathbb{R}^3$, generalized cylinder coordinates (r, α, h) of a carthesian point $\mathbf{p} \in \mathbb{R}^3$ with respect to \mathbf{c} are defined as follows:

- The height h is defined by the arc length computed along the curve \mathbf{c} from its origin $\mathbf{c}(a)$ to the orthogonal projection \mathbf{p}_c of \mathbf{p} onto \mathbf{c} .
- The radius $r = \|\mathbf{p}_c - \mathbf{p}\|$.
- The angle α is defined by the angle between \mathbf{p} and the projection \mathbf{q}_p of \mathbf{q} onto a plane E orthogonal to \mathbf{c} in \mathbf{p}_c , measured around the central point \mathbf{p}_c .

The construction requires the curvature of \mathbf{c} to be reasonably low to ensure that the orthogonal projection of each \mathbf{p} onto \mathbf{c} is definite. This

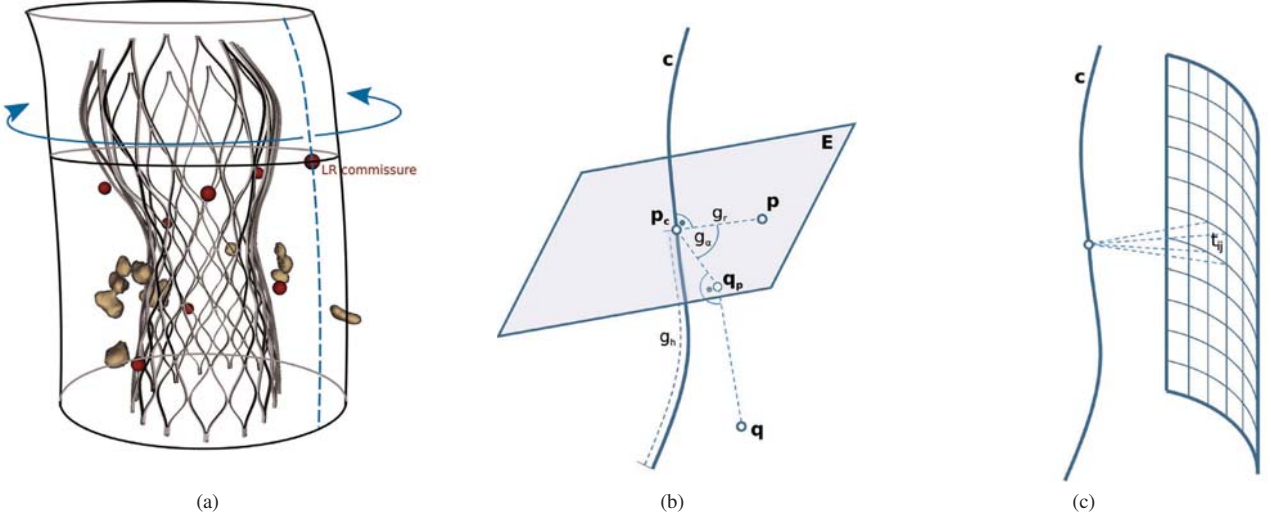


Fig. 4. (a) Generalized cylinder wrapped around the deformed stent. The datasets are cut and unrolled at a consistent landmark. (b) Construction of generalized cylinder coordinates. (c) Map tile on the surface of the generalized cylinder.

curvature requirement is fulfilled in our case, since the implanted aortic valve stents are compressed but not strongly bent. As reference point, we use the commissure between the left and right coronary sinus (see arrow in Fig. 1a). This commissure therefore corresponds to an angle of 0° and represents the left and right border of the stent map.

As a result of this step, a specific position in the 3D scene can be mapped to a specific position in the 2D stent map (i.e., a specific tile). More specifically, the angle of the generalized cylindrical coordinates corresponds to the horizontal axis and the height to the vertical axis in the map. We further speed up the processing by binning the mesh vertices according to height and angle of these generalized cylindrical coordinates.

4.3.2 Creating the map

The stent map consists of tiles. Each tile corresponds to a 3D segment of the scene as viewed from the stent's centerline (see Figure 4c) and its color represents the respective parameter value of this segment. The user can adjust the number of tiles in height and width and with that change the resolution from a high-resolution rendering of the scene (where a tile is simply represented by a pixel) to a more abstract heatmap with reduced data dimensionality.

As a next step in map creation, the respective parameter values for the tiles need to be computed. We implemented and compared two variants.

Direct vertex assignment The first variant is a straight-forward assignment of a vertex to the map tiles based on its generalized cylindrical coordinates. For each vertex $\mathbf{v} \in \mathbb{R}^3$, we use the following equations to compute the two-dimensional index (i, j) of its respective tile t_{ij} :

- $i = \left\lfloor \frac{\alpha_t}{\alpha_w} \right\rfloor$ with $\alpha_t = \frac{360^\circ}{n_w}$
- $j = \left\lfloor \frac{h_t}{h_s} \right\rfloor$ with $h_t = \frac{h_s}{n_h}$

with the stent height h_s and the map resolution $n_w \times n_h$.

As explained previously in Section 4.1, the different parameters of interest for each tile are the radial force \mathbf{rf} , the calcium thickness \mathbf{ct} , and the stent compression \mathbf{sc} . We compute a tile's \mathbf{rf} by determining the maximal radial force over all stent mesh vertices assigned to this tile. We compute a tile's \mathbf{ct} by subtracting the minimal from the maximal radius of calcium mesh vertices assigned to this tile. As only calcium in the closer vicinity of the stent is of interest, we neglect the calcium information for a tile with a minimal calcium radius larger

than 6 mm . Finally, for the computation of a tile's \mathbf{sc} , we determine the tile's maximal, absolute difference of stent radius to the original radius r_{orig} of the unimplanted stent at the same height. The stent compression is then determined by $\mathbf{sc} = \frac{r - r_{orig}}{r_{orig}}$.

The advantage of this method is its efficiency and low run-time. However, it also introduces inaccuracies since only vertex information not triangle information is used for map creation (see further discussion in Sec. 5.3, 6).

Therefore, we also implemented a more precise sampling method that we will compare this method to.

Raycasting The second variant is a raycasting, which samples the 3D scene with rays capturing one 3D segment each. Rays are started from the stent's centerline and capture the scene orthogonal to the centerline in equal angular steps. The resulting map shows the 3D scene from the stent's inside and implicitly straightens the scene. This raycasting approach can be efficiently implemented by utilizing the generalized cylindrical coordinates. The direction of a ray can be given by an angle and height in generalized cylindrical coordinates. Checking for an intersection of a ray with a triangle then boils down to checking whether a 2D point lies in a 2D triangle. Instead of rendering the illuminated mesh (as with traditional raycasting), the properties of maximal radial forces, stent compression, and minimal and maximal calcium radius are determined like in the previous section and stored for each ray for further processing. For each ray, all triangles in the bin need to be tested. The number of rays is not determined by the map or screen resolution but chosen so that the scene is sufficiently sampled. Therefore, we use a virtual resolution of 2400×1200 . This means that a ray covers a 3D segment of 0.15° and a height of about 0.04 mm (stent height ranges between 51.15 mm and 53.87 mm). From this potentially oversampled information, the map with the user-desired tile resolution is determined by aggregating ray information and determining the respective maximal radial force, calcium thickness, and stent compression for the tile.

Due to the stent's grid-like shape, the stent data (necessary for stent compression and calcium thickness properties) in the map is only sparse. With both sampling methods, the missing information between the stent wires is linearly interpolated from the neighboring stent information for complete coverage.

Context rendering

The anatomical and stent context is displayed in the map as a spatial guide for the users. It allows them to detect patient-specific aortic

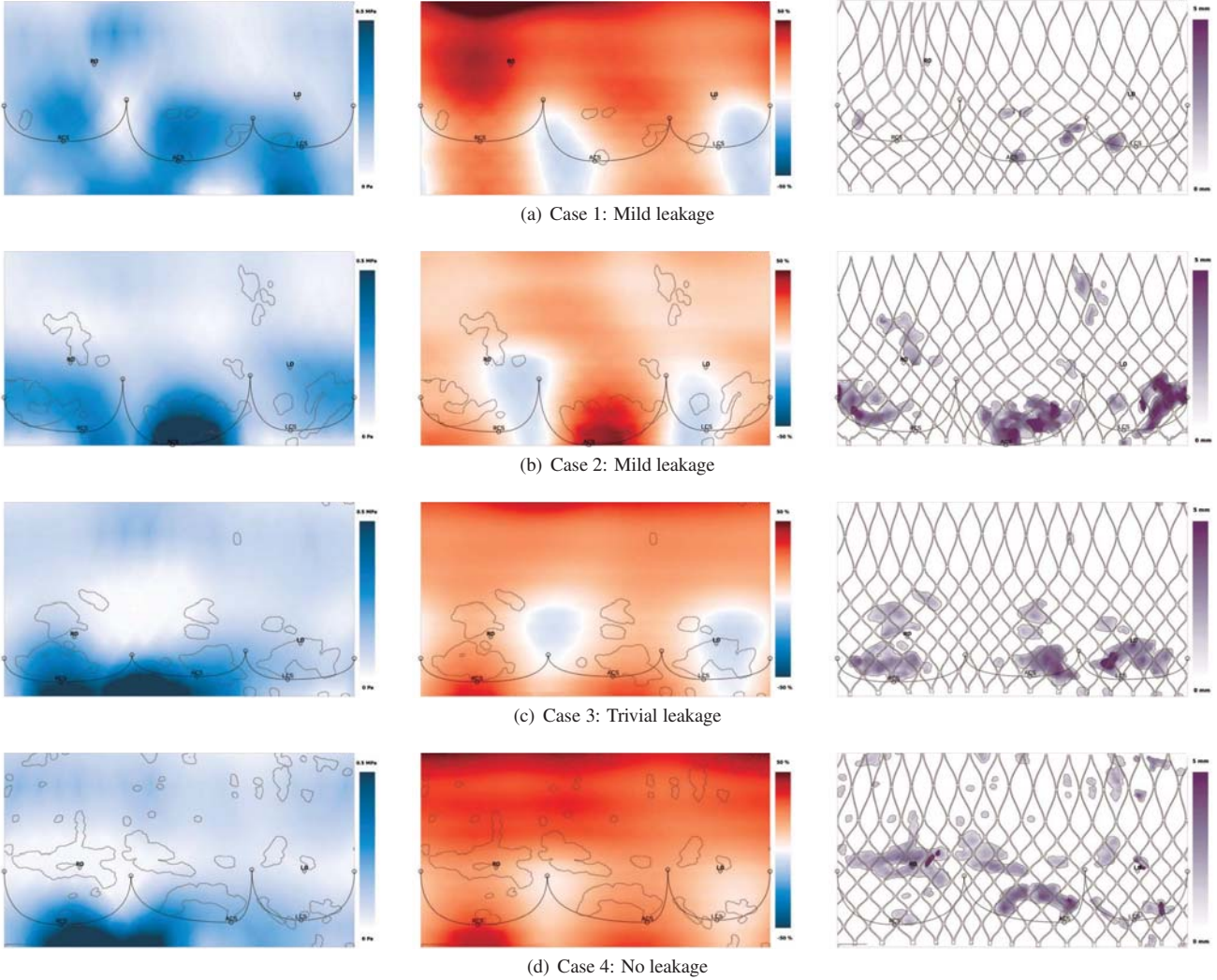


Fig. 5. Stent maps of four TAVI patients (one patient per row). Each column shows a different parameter of interest. Left: Radial force. Middle: Stent compression (red indicates compression, blue expansion with respect to original stent shape). Right: Calcium thickness. All color maps in a column are scaled equally. Abbreviations: Left coronary artery (LA), right coronary artery (RA), left coronary sinus (LCS), right coronary sinus (RCS), non-coronary sinus (ACS).

valve anomalies, analyze the stent implantation height, stent deformation, amount and distribution of calcium, and to rate the different map parameters in this context. In order to avoid the occlusion of the color-coded map parameters, all context is displayed as an unobtrusive, comprehensible line rendering.

The anatomical landmarks, which were detected in the CT data previously (see Sec. 4.2), are now used to render the patient-individual shape of the aortic valve (similar to Fig. 1b). The localization of the landmarks on the stent map is done analogously to the direct vertex assignment by using generalized cylindrical coordinates. The valve crown is defined by the three commissure landmarks and the three bottom points of the sinuses. From these six landmarks the crown-shape is approximated with one B-spline curve per sinus. Further, the left and right coronary arteries are displayed and annotated.

The calcifications are shown as contours of the calcium chunks. These contours are drawn at the borders of tiles with and without calcium information. This implies that the calcium renderings have the same resolution as the complete stent map and appear unsmeared for lower resolutions. The stent contours can be rendered analogously to the calcium context.

Population stent maps

It is not only of interest to analyze data of individual patients, but also of larger populations. For this matter, we generate population stent maps providing results of statistical evaluations (as, e.g., mean, standard deviation, weighted differences) conducted on the parameter data of patient cohorts with or without PVL. The anatomical landmark positions are averaged for each cohort and displayed as its mean aortic valve morphology. Altogether, these population maps allow to detect typical patterns for leaking and leakproof cases and to compare the individual patient to these patterns.

5 RESULTS

We applied our stent map technique to 15 postoperative CT datasets of TAVI patients (3 cases without leakage, 4 cases with trivial leakage, 8 cases with mild leakage, no cases with moderate or severe leakage). Figure 5 shows exemplary results for four patients with different PVL outcomes. These maps display several patient-individual anatomical aspects and spatial information about the implanted stent: From the arch-like sinus renderings, one can observe distinctive anatomical features like, e.g., the rather flat aortic root in case 3 (see narrow arches in Figure 5c). The height of the sinus renderings on the map reflects

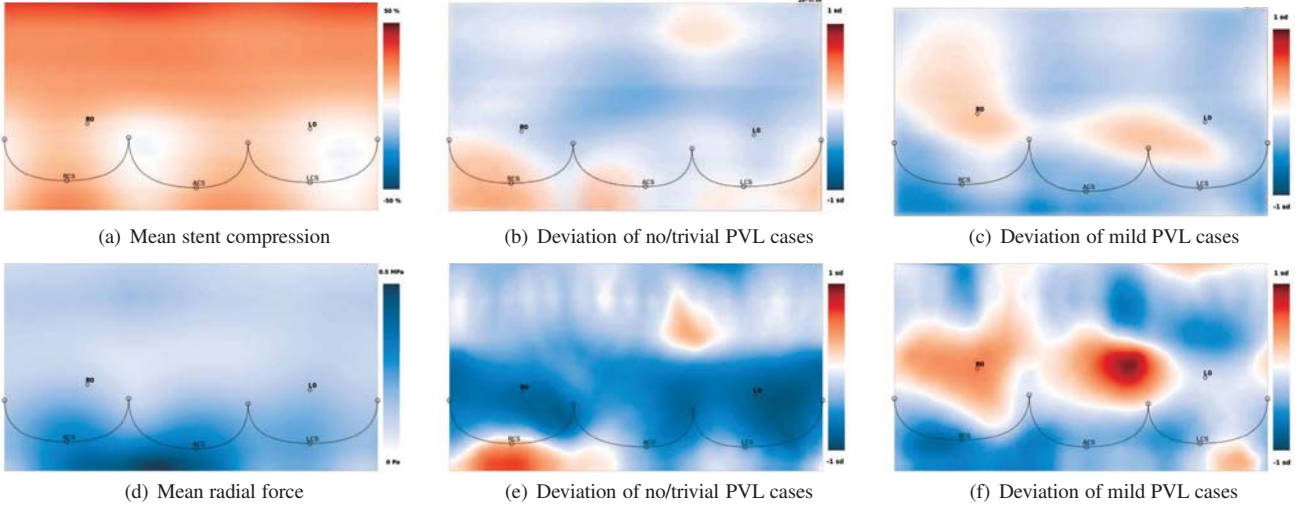


Fig. 6. Population stent maps for stent compression (top row) and radial forces (bottom row). The left column shows the map with the parameter mean for all 15 datasets. In (a) the elliptical shape of the stent profile can be observed. (d) shows the maximal force concentration on the bottom left border of the stent maps. The middle column shows the difference of the parameter mean of the whole population and the no/trivial leakage cohort weighted with the standard deviation (sd). The right column shows the same for the mild leakage cohort. The color maps in b,c,e,f have the same scale. Abbreviations: Left coronary artery (LA), right coronary artery (RA), left coronary sinus (LCS), right coronary sinus (RCS), non-coronary sinus (ACS).

the stent implantation height. Highly-positioned sinuses in the map correspond to a low implantation (see Fig. 5a), and vice versa (see Fig. 5b). The shape of the implanted stent is shown by the stent overlay (see Fig. 5, right column) and the color-coded stent deformation (Fig. 5, middle column). The calcium contour renderings and the calcium thickness map (Fig. 5, right column) allow conclusions regarding the amount and distribution of calcifications in the vicinity of the stent. From the radial force maps (Fig. 5, left column) one can study maximal or minimal force values and their distribution. Finally, population maps (see Fig. 6) show the same criteria for larger patient subgroups and allow researchers to identify patterns typical for different PVL outcomes.

5.1 Feedback of clinical experts

We introduced our method to two heart surgeons (co-authors; one very experienced, one assistant physician) separately by showing and explaining 2-3 stent maps and giving them the opportunity to also explore the corresponding postoperative CT data (similar to Fig. 2a) and 3D stent visualizations with embedded landmark positions and calcifications (similar to Fig. 3). After that, they analyzed the 15 datasets with known PVL outcome. The goal of this overall procedure was to observe the experts during training and analysis and collect their feedback about the visualization, but at the same time to start generate strategies to predict PVL from these maps (by pattern identification).

Heart surgeons are used to work with CT image data, which is mainly viewed as 2D slices (see Fig. 2a). Surgeons are well-trained in mentally creating a three-dimensional impression of this 2D data. However, stent maps show a different kind of 2D view the experts are not used to. Consequently they needed some training to understand and translate the 2D stent map into a mental 3D model as well. The training helped them understand the shown view point, the order of the sinuses, and the color-codings (especially the deformation map). Still, the training phase took no longer than 10 min during which they already started to discuss similarities and differences in the maps and possible conclusions.

Preliminary medical insights gained from these analyses are described in Section 5.2. During analysis, they appreciated the design decision to rely on several side-by-side maps with consistent layout instead of trying to create an all-in-one visualization at this state. Altogether, this design facilitated to grasp the characteristics of one dataset by exploring its numerous parameters and to compare these charac-

teristics in different datasets with different outcomes. At a glance, it was possible for them to identify cases with, e.g., especially high or low positioned stents, with concise force maxima or especially thick and unevenly distributed calcifications. They stated that this would not be possible with state-of-the-art 3D visualizations of the same CT and simulation data (see Fig. 3). These are appropriate for a 3D spatial impression of a single dataset but have several disadvantages: (1) It takes longer to get an overview over a single dataset due to the necessary navigation; (2) comparison of several datasets is more difficult because users need to repeatedly orientate themselves in the anatomy (e.g., identify the sinuses) and find corresponding landmarks; (3) one cannot easily quantify and compare parameters like deformation or calcium distance to the stent, which is possible with the color-coded parameter values in the stent maps; (4) 3D visualizations of whole populations are also not available. So, altogether, the heart surgeons appreciated the advantages of this visualization and are confident that this research direction will bring interesting insights when applied to a larger database.

Further, the clinical experts could imagine several variants and other use cases for this visualization technique. It could easily adapted to other heart valve interventions like the catheter-based implantation of pulmonary or mitral valve prostheses. These are not clinically established yet, but similar questions about selecting the most appropriate valve type, size, and position will come up and the adaption of stent maps to other anatomical situations and prostheses types is rather straight-forward. Other interesting use cases is the planning of different types of aneurysm stenting. A suitable cardiovascular example is the endovascular aneurysm repair (EVAR). Here, Y-shaped stents are inserted minimally-invasive to treat aneurysms in the abdominal aorta. Complications of interest are endoleaks (where an aneurysm is still supplied with blood) or the blocking of important branching arteries. The anatomical situation is comparable between patients and therefore well-suited for analysis with stent maps. Also thinkable is the addition of blood flow information from CFD simulations or flow-sensitive MRI measurements. A second aneurysm use case could be the planning of flow diverter stenting of cerebral aneurysms. Here, complications like stent creeping or perforator infarctions (where the blood flow in important branching vessels is pathologically altered) are investigated. Apart from vessel stenting, tracheal or oesophageal stenting could be investigated as possible stent map applications. Altogether, it is thinkable to adapt and apply stent maps to several other

medical use cases and maybe even establish it as a standard way of displaying multi-parametric data in these contexts (similar to the bull's eye plot described in Sec. 2).

As limitations the medical experts stated the uncertainty about the landmarks. These are reconstructed from the underlying CT data and thus depend on experts' manual positioning. However, this drawback is also true for CT data and the previously shown 3D visualizations. Further, they missed interactivity. In contrast to computed tomography series where the clinician can scroll through the layers, the expert only has one set of images with a lower degree of interaction at his disposal. However, they could not state in detail what further interactions they needed.

As result from this feedback, we believe that an increased acceptance of this visualization method can be expected by training them with typical and representative example cases and by making additional CT data and 3D visualizations available, so that they can – when in doubt – double-check the data with familiar display techniques. Acceptance in clinical routine should also be increased by further research, i.e., when more patterns and criteria have been found for different outcomes, the clinicians will know what they are looking for. When that state of maturity will be reached in the future, they would also vote for a more compact display for use in the clinical routine, i.e., when risk factors for PVL are better known and the visualization would serve not for pattern searching but to merely display simulation results. Then, it might also not be of great importance anymore to create a anatomical mental model from the stent maps but to check for known patterns in rather abstract images.

5.2 Medical insights

Several interesting medical insights have been gained from the stent map visualizations. These insights are preliminary until a larger number of cases has been analyzed, but still very promising.

- Not the mere presence or absence of calcium seems to be important for PVL occurrence, but calcium distribution: mild leakage case 1 has PVL but only very little calcifications, whereas case 4 (without leakage) has lots of calcium but no PVL. For example, it is thinkable that neighboring, thick calcium chunks (see Fig. 5b) form a channel for the blood to flow through. Especially if at the same position the radial force is low and/or the stent is not very compressed.
- From the radial force maps a force concentration at the stent map's lower end below RCS and NCS can be observed for cases 3 and 4. The PVL cases 1 and 2 differ from this pattern. Especially case 1 shows rather low overall force, which might cause PVL because the stent does not sufficiently adapt to its surrounding structures (because it is not fully expanded or the chosen stent size is too small).
- The mild leakage cases 1 and 2 show comparably low and comparably high implantation heights respectively. Cases 3 and 4 with trivial and no leakage, however, have well-positioned stents. This might confirm the theory that an inappropriate implantation height has a strong influence on PVL occurrence.
- A very interesting observation are two blueish stripes in the stent compression maps (middle column) – with one of the stripes located very close to the RN-commissure. The oval shape of the implanted stent (which is the meaning of the stripe pattern) has been observed before but it is a new finding that the oval shape seems to have a preferred orientation in the aortic annulus. The mean stent compression over all 15 patient datasets is shown in Figure 6a and also clearly displays the elliptical shape observed with the four datasets in Figure 5.
- When comparing stent compression data of cohorts of similar outcomes to the mean data, deviations can be noticed: the mild leakage cohort (see Fig. 6c) shows lower compression at the lower end of the stent and higher compression in the middle region; the cohort of non-leakage and trivial leakage cases (which

we examine as one population) shows almost the inverted pattern with more compression in the area below the RCS and less compression above the aortic valve.

- A similar pattern difference can also be observed for the radial force information. Figure 6d shows the mean force of the whole population. The maximum force concentration below RCS stands out clearly, which is lowered in the mild leakage cohort (see Fig. 6f) and even stronger in non-leakage and trivial cases (see Fig. 6d).

The mean force and compression patterns are very interesting findings for the clinical experts, as they give a hint on possible PVL prediction patterns. However, these deviation patterns are observed in a study of only 15 datasets. Therefore, they will be further applied to a larger population in the future and hopefully confirm the tendency that the cohorts can be distinguished with this approach.

5.3 Comparison of sampling methods

The advantage of sampling with raycasting is its precision, which however comes at the cost of some preprocessing time (for sampling and interpolation). The actual map drawing (tile averaging and rendering) depends on the map resolution and takes below 250 ms for a lower tile resolution (120×70) and 345 ms – 975 ms for a higher tile resolution (1000×600). The different times relate to different parameters with different processing costs. The preprocessing may take up to 10 s. However, it could be decreased by code optimization and by using a smaller number of rays.

With direct vertex assignment (DVA) the scene is sampled whenever the map is rendered, which makes preprocessing unnecessary. For a larger tile resolution the map creation (which includes sampling, interpolation, and rendering) takes slightly longer than the raycasting method (between 850 ms and 1.21 s) and has the disadvantage that holes occur when triangles are larger than the tiles (because only vertices are mapped, not the triangles). For smaller resolutions however the run-time is considerably lower than the raycasting method (below 22 ms).

For comparative visualization, we don't necessarily aim at highly resolved images but rather at small multiple views so many maps fit on the screen for comparison. For this, a lower map resolution is sufficient and the cheaper vertex assignment is a valid alternative provided that it is accurate enough. The maps produced by DVA are visually comparable to raycasting. An additional quantitative comparison of these maps was conducted by analyzing the normalized root mean square errors (NRMSE), which produced a low mean NRMSE (over all datasets combined) of 0.06 for force and compression maps and 0.04 for calcium thickness maps. The NRMSE for the individual datasets is given in Figure 7.

Following these analyses, we use the faster DVA for small multiples generation, but still rely on raycasting when we generate data for statistical analyses or high-quality images (as shown in the previous section). Further, one needs to keep in mind that the map accuracy not only depends on the sampling but also on the interpolation technique, which we will further research in the future (see Sec. 6).

6 CONCLUSION

In this work, we have presented stent maps, which are a multi-parametric visualization of medical CT data and mechanical simulation results. This tool is applied for the research of indicators for PVL occurrence after TAVI. Stent maps represent the area of the unrolled stent and show aortic valve anatomy, calcifications, and stent shape as line renderings. The parameters of interest, which are suspected to have an influence on the occurrence of PVL, are shown in a heatmap-like manner. With that, stent maps incorporate all information of interest in a comprehensible way and allows a convenient overview over different parameter patterns of individual patients and patient cohorts. This compact information integration is not achieved when viewing the data as 3D scene or examining the raw CT data and therefore could improve the planning of TAVI procedures. The resolution of the map can be adjusted from a highly-resolved view with a

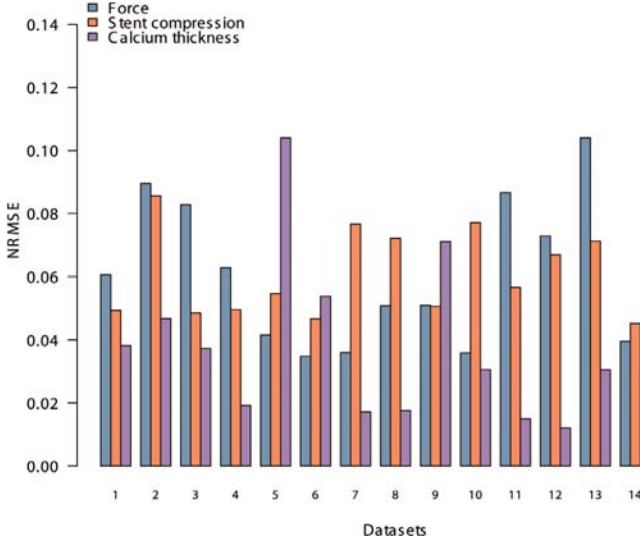


Fig. 7. Comparison of maps rendered with raycasting or by assigning vertices directly to the tiles. (a) Diagram shows the normalized root mean square error (NRMSE) of the maps for the 15 datasets for each parameter map separately.

higher image quality to a low-resolution, more abstract version. The latter is useful for view as small multiples and if a larger dimensionality reduction is desired for further statistical or computational analysis.

For the local assignment of mesh data onto a stent map, we have implemented two sampling methods differing in run-time. Comparison of stent maps rendered with the two methods showed that for lower-resolved images the direct vertex assignment and the raycasting method achieve results with comparable quality. Therefore, the faster DVA method is valid for use with the small multiples view.

The application of our method to 15 datasets revealed several novel radial force and stent compression patterns, which are very promising to bring clinical research closer to understanding different risk factors and their interaction in the context of PVL formation. The gained insight confirms that the abstraction and dimensionality reduction of our method helps comparing numerous datasets and finding patterns, which has not been feasible with other methods, such as 3D renderings as shown in Figure 3. The clinical experts are confident that we will yield significant results when applying our methods of mechanical simulation and stent maps to a larger database. Also, the application of stent maps to other medical use cases such as the preoperative planning of other heart valve interventions or aneurysm stenting could be very beneficial.

Our work gives several starting points for future work. The first has been mentioned already, which is the extension of our training database regarding the number of datasets and types of leakage severities (moderate and severe PVL missing so far). When doing so, new requirements or new parameters of interest might arise. Further, the patterns we have found were eye-catching in the sense that they could also help explain the occurrence of other side effects such as transvalvular leakages and left bundle branch block. Therefore, an investigation considering these outcomes would be of great medical interest as well. A further important aim is the translation of these new tools into clinical practice by facilitating and accelerating the methods necessary to create the stent maps. From a technical point of view, we plan to not only rely on human pattern matching abilities, but we will intensify our research with machine learning and computational pattern matching. Also, the linear interpolation scheme we used for the approximation of stent distances and radial forces between the stent wires is very simple. It has shown satisfactory results, but especially for the forces, we will check whether a more sophisticated interpolation method (such as, e.g., spatial kriging) is more appropriate. Further, we want to investi-

gate whether the strict cut-off at one commissure hinders identifying patterns stretching over this landmark. Alternatively, one could repeat a portion of the neighboring sinus at both ends of the map. A mentioned limitation of our approach is the uncertainty of the manually defined landmarks. We will work on an appropriate way of communicating this uncertainty in the individual and the population stent maps. Finally, we have decided to use a side-by-side visualization approach for the sake of clarity and comprehensibility. For the future, when patterns and PVL indicators are more clear, the goal will be to create a more compact visualization of standardized patterns hinting on PVL occurrence, which would further improve usability for the expert clinician.

ACKNOWLEDGMENTS

The authors wish to thank Stefan Schwyter for preparing the medical illustrations. This work was supported in part by the Swiss National Science Foundation (grant no. CR32I3_135044).

REFERENCES

- [1] P. Angelelli and H. Hauser. Straightening tubular flow for side-by-side visualization. *IEEE TVCG*, 17(12):2063–2070, 2011.
- [2] L. Antiga and D. Steinman. Robust and objective decomposition and mapping of bifurcating vessels. *IEEE T Med Imaging*, 23(6):704–713, 2004.
- [3] F. Auricchio, M. Conti, S. Morganti, and A. Reali. Simulation of transcatheter aortic valve implantation: a patient-specific finite element approach. *Comput Method Biomed*, (March 2013):37–41, Feb. 2013.
- [4] A. J. Barker, M. Markl, J. Bürk, R. Lorenz, J. Bock, S. Bauer, J. SchulzMenger, and F. von Knobelsdorff-Brenkenhoff. Bicuspid Aortic Valve is Associated with Altered Wall Shear Stress in the Ascending Aorta. *Circulation*, 5(4):457–66, July 2012.
- [5] A. V. Bartroli, R. Wegenkittl, A. König, and E. Gröller. Nonlinear virtual colon unfolding. In *IEEE Visualization*, pages 411–420, 2001.
- [6] C. Capelli, G. M. Bosi, E. Cerri, J. Nordmeyer, T. Odenwald, P. Bonhoeffer, F. Migliavacca, a. M. Taylor, and S. Schievano. Patient-specific simulations of transcatheter aortic valve stent implantation. *Med Biol Eng Comput*, 50(2):183–92, Feb. 2012.
- [7] S. Diepenbrock, S. Hermann, M. Schäfers, M. K. And, and K. Hinrichs. Comparative Visualization of Tracer Uptake in In Vivo Small Animal PET/CT Imaging of the Carotid Arteries. *Comput Graph Forum*, 32(3):241–250, 2013.
- [8] FEops (Gent, Belgium). FEops – Better healthcare through simulations, Mar. 2014.
- [9] M. Gessat, L. Altweig, T. Frauenfelder, A. Plass, and V. Falk. Cubic hermite bezier spline based reconstruction of implanted aortic valve stents from ct images. In *Proc. of IEEE EMBC*, pages 2667–2670, Aug 2011.
- [10] M. Gessat, R. Hopf, T. Pollok, C. Russ, T. Frauenfelder, S. Sündermann, S. Hirsch, E. Mazza, G. Szekely, and V. Falk. Image-based mechanical analysis of stent deformation: Concept and exemplary implementation for aortic valve stents. *IEEE T Bio-Med Eng*, 61(1):4–15, Jan 2014.
- [11] O. Gjesdal and T. Edvardsen. Tissue Doppler in ischemic heart disease. *Establishing better standards of care in Doppler echocardiography, computed tomography and nuclear cardiology*, 2011.
- [12] S. Glaß er, U. Preim, K. Tömmies, and B. Preim. A visual analytics approach to diagnosis of breast DCE-MRI data. *Computers & Graphics*, 2010.
- [13] K. Gurijala, R. Shi, W. Zeng, X. Gu, and A. Kaufman. Colon Flattening Using Heat Diffusion Riemannian Metric. *IEEE TVCG*, 19(12):2848–2857, 2013.
- [14] R. Hopf, G. M., F. V., and M. E. Reconstruction of stent induced loading forces on the aortic valve complex. In *Proc. of MICCAI-Workshop on Computer-Assisted Stenting*, pages 104–111, October 2012.
- [15] T. Huysmans, J. Sijbers, and B. Verdonk. Parameterization of Tubular Surfaces on the Cylinder. *Journal of WSCG*, 13(3):97–104, 2005.
- [16] A. Kanitsar, R. Wegenkittl, D. Fleischmann, and M. Groller. Advanced curved planar reformation: flattening of vascular structures. *Proc. of IEEE Visualization*, pages 43–50, 2003.
- [17] S. K. Kodali, M. R. Williams, C. R. Smith, L. G. Svensson, J. G. Webb, R. R. Makkar, G. P. Fontana, T. M. Dewey, V. H. Thourani, A. D. Richard, M. Fischbein, W. Y. Szeto, S. Lim, K. L. Greason, P. S. Teirstein, S. C. Malaisrie, P. S. Douglas, R. T. Hahn, B. Whisenant, A. Zajarias, D. Wang,

- J. J. Akin, W. N. Anderson, and M. B. Leon. Two-year outcomes after transcatheter or surgical aortic-valve replacement. *New Engl J M*, 366(18):1686–95, May 2012.
- [18] D. Lindahl, J. Palmer, J. Pettersson, T. White, A. Lundin, and L. Edendbrandt. Scintigraphic diagnosis of coronary artery disease: myocardial bull's-eye images contain the important information. *Clin Physiol*, 18(6):554–561, 1998.
- [19] M. Minoves, A. Garcia, J. Magrina, J. Pavla, R. Herranz, and J. Setoain. Evaluation of myocardial perfusion defects by means of bulls eye images. *Clin Cardiol*, 22:16–22, 1993.
- [20] G. Mistelbauer, A. Morar, A. Varchola, R. Schernthaner, I. Baclija, A. Kéchl, A. Kanitsar, S. Bruckner, and E. Gröller. Vessel Visualization using Curvilinear Feature Aggregation. *Comput Graph Forum*, 32(3):231–240, 2013.
- [21] M. Neugebauer, R. Gasteiger, O. Beuing, V. Diehl, M. Skalej, and B. Preim. Map Displays for the Analysis of Scalar Data on Cerebral Aneurysm Surfaces. *Comput Graph Forum*, 28(3):895–902, June 2009.
- [22] R. Nishimura. Aortic Valve Disease. *Circulation*, 106(7):770–772, Aug. 2002.
- [23] C. Reidy, A. Sophocles, H. Ramakrishna, K. Ghadimi, P. Patel, and J. G. T. Augoustides. Challenges after the first decade of transcatheter aortic valve replacement: focus on vascular complications, stroke, and paravalvular leak. *J Cardiothorac Vasc Anesth*, 27(1):184–9, Feb. 2013.
- [24] T. Ropinski, S. Hermann, R. Reich, M. Schäfers, and K. Hinrichs. Multimodal vessel visualization of mouse aorta PET/CT scans. *IEEE TVCG*, 15(6):1515–22, 2009.
- [25] C. Russ, R. Hopf, S. Hirsch, S. Sündermann, V. Falk, G. Szekely, and M. Gessat. Simulation of transcatheter aortic valve implantation under consideration of leaflet calcification. In *Proc. of IEEE EMBC*, pages 711–714, July 2013.
- [26] C. Tamburino, D. Capodanno, A. Ramondo, A. S. Petronio, F. Ettori, G. Santoro, S. Klugmann, F. Bedogni, F. Maisano, A. Marzocchi, A. Poli, D. Antonucci, M. Napodano, M. De Carlo, C. Fiorina, and G. P. Ussia. Incidence and predictors of early and late mortality after transcatheter aortic valve implantation in 663 patients with severe aortic stenosis. *Circulation*, 123(3):299–308, Jan. 2011.
- [27] G. Tarantini, V. Gasparetto, M. Napodano, C. Fraccaro, G. Gerosa, and G. Isabella. Valvular leak after transcatheter aortic valve implantation: a clinician update on epidemiology, pathophysiology and clinical implications. *Am J Cardiovasc Dis*, 1(3):312–20, Jan. 2011.
- [28] M. Termeer, J. Oliván Bescós, M. Breeuwer, A. Vilanova, F. Gerritsen, and E. Gröller. CoViCAD: Comprehensive visualization of coronary artery disease. *IEEE TVCG*, 13(6):1632–9, 2007.
- [29] A. Vahanian, O. Alfieri, F. Andreotti, M. J. Antunes, G. Barón-Esquivias, H. Baumgartner, M. A. Borger, T. P. Carrel, M. De Bonis, A. Evangelista, V. Falk, B. Iung, P. Lancellotti, L. Pierard, S. Price, H.-J. Schäfers, G. Schuler, J. Stepinska, K. Swedberg, J. Takkenberg, U. O. Von Oppell, S. Windecker, J. L. Zamorano, and M. Zembala. Guidelines on the management of valvular heart disease (version 2012). *Eur Heart J*, 33(19):2451–96, Oct. 2012.
- [30] Q. Wang, E. Sirois, and W. Sun. Patient-specific modeling of biomechanical interaction in transcatheter aortic valve deployment. *J Biomech*, 45(11):1965–71, July 2012.
- [31] L. Zhu, S. Haker, and S. Tannenbaum. Flattening maps for the visualization of multibranched vessels. *IEEE T Med Imaging*, 24(2):191–198, 2005.

2.5 Bildgestützte mechanische Analyse der Deformation von Transkatheter-Aortenklappenprothesen-Stents

Gessat M, Hopf R, Pollok T, Russ C, Frauenfelder T, Sündermann SH, Hirsch S, Mazza E, Székely G, Falk V

Image-based Mechanical Analysis of Stent Deformation: Concept and Exemplary Implementation for Aortic Valve Stents.

IEEE Trans Biomed Eng 2014;61(1):4-15³⁷

[doi: 10.1109/TBME.2013.2273496](https://doi.org/10.1109/TBME.2013.2273496)

In dieser Studie wurde bei Patienten, bei welchen eine Transkatheter-Aortenklappenimplantation (TAVI) durchgeführt wurde, nach der Intervention eine CT durchgeführt. Aus diesen Bilddaten wurde der implantierte Stent modelliert und die Deformation berechnet. Anhand der Deformation des Stents wurden mathematisch Rückschlüsse auf die Radialkräfte gezogen, welche die Deformation verursacht haben. Für 21 Patienten wurden die Stent-Analysen durchgeführt. Bei 18 Patienten gelang eine Extraktion von allen Parametern, welche eine Analyse der Radialkräfte ermöglichte. Bei 3 Patienten lagen Bewegungsartefakte vor, welche eine Landmarkextraktion erschwerten bzw. unmöglich machten. Bei allen anderen Patienten konnten die 167 Landmarken, welche den Stent definieren, identifiziert werden. Die Identifizierung des Stents gelang auch in Bereichen, in welchen Kalzifikationen den Stent überlagerten. Zur Validierung der automatischen Extraktion des Stents wurden für 5 Patienten alle 167 Landmarken manuell von jeweils 3 Probanden gesetzt. Die Abweichung betrug deutlich unter einem Millimeter. Die berechneten Radialkräfte lagen zwischen 0 Newton an Stellen, an denen der Stent nicht an der Gefäßwand anlag, und maximal 2.06 Newton. Die mittlere Radialkraft am Annulus betrug ca. 0.4 Newton, im mittleren Teil ca. 0.1 Newton und im distalen Bereich des Stents zwischen 0.2 und 0.4 Newton.

Zusammenfassend kann festgehalten werden, dass es gelungen ist, anhand der aus CT-Daten modellierten Stents von Transkatheter-Aortenklappenprothesen und deren Deformation Rückschlüsse auf die am Stent wirkenden Radialkräfte zu ziehen. Diese Ergebnisse tragen zu einem besseren Verständnis der mechanischen Kräfte bei, welche bei dieser Art Intervention auftreten, und können als Grundlage für Simulationen dienen, welche zur Vorhersage von typischen Komplikationen durchgeführt werden. Dadurch könnte eine individuellere Therapieplanung gelingen und patientenspezifische Faktoren besser berücksichtigt werden.

Image-Based Mechanical Analysis of Stent Deformation: Concept and Exemplary Implementation for Aortic Valve Stents

Michael Gessat*, Raoul Hopf, Thomas Pollok, Christoph Russ, *Student Member, IEEE*, Thomas Frauenfelder, Simon Harald Sündermann, Sven Hirsch, Edoardo Mazza, Gábor Székely, *Member, IEEE*, and Volkmar Falk

Abstract—An approach for extracting the radial force load on an implanted stent from medical images is proposed. To exemplify the approach, a system is presented which computes a radial force estimation from computer tomography images acquired from patients who underwent transcatheter aortic valve implantation (TAVI). The deformed shape of the implanted valve prosthesis' Nitinol frame is extracted from the images. A set of displacement vectors is computed that parameterizes the observed deformation. An iterative relaxation algorithm is employed to adapt the information extracted from the images to a finite-element model of the stent, and the radial components of the interaction forces between the stent and the tissue are extracted. For the evaluation of the method, tests were run using the clinical data from 21 patients. Stent modeling and extraction of the radial forces were successful in 18 cases. Synthetic test cases were generated, in addition, for assessing the sensitivity to the measurement errors. In a sensitivity analysis, the geometric error of the stent reconstruction was below 0.3 mm, which is below the image resolution. The distribution of the radial forces was qualitatively and quantitatively reasonable. An uncertainty remains in the quantitative evaluation of the radial forces due to the uncertainty in defining a radial direction on the deformed stent. With our approach, the mechanical situation of TAVI stents after the implantation can be studied *in vivo*, which may help to understand the mechanisms that lead to the complications and improve stent design.

Index Terms—Biomedical image processing, biomedical imaging, biomechanical simulation, finite element analysis, implants.

Manuscript received March 25, 2013; revised June 7, 2013; July 1, 2013; accepted July 5, 2013. Date of publication July 16, 2013; date of current version December 16, 2013. This work was supported in part by the Swiss National Science Foundation under Grant CR32I3_135044, in part by the Swiss Heart Foundation, and in part by the Baden-Württemberg Stipendium. Asterisk indicates corresponding author.

*M. Gessat is with the Hybrid Laboratory for Cardiovascular Technologies, University of Zurich, 8091 Zurich, Switzerland, and also with the Computer Vision Laboratory, Swiss Federal Institute of Technology (ETH) Zurich, 8092 Zurich, Switzerland (e-mail: mgessat@ethz.ch).

R. Hopf and E. Mazza are with the Center of Mechanics, Swiss Federal Institute of Technology (ETH) Zurich, 8092 Zurich, Switzerland (e-mail: hopf@imes.mavt.ethz.ch; edoardo.mazza@imes.mavt.ethz.ch).

T. Pollok is with the Berlin Institute of Technology, 10623 Berlin, Germany (e-mail: tom.pollok@googlemail.com).

C. Russ, S. Hirsch, and G. Székely are with the Computer Vision Laboratory, Swiss Federal Institute of Technology (ETH) Zurich, 8092 Zurich, Switzerland (e-mail: russc@ethz.ch; hirsch@vision.ee.ethz.ch; szekely@vision.ee.ethz.ch).

T. Frauenfelder is with the Institute of Diagnostic and Interventional Radiology, University Hospital Zurich, 8091 Zurich, Switzerland (e-mail: thomas.frauenfelder@usz.ch).

S. H. Sündermann and V. Falk are with the Division of Cardiovascular Surgery, University Hospital Zurich, 8091 Zurich, Switzerland (e-mail: simon.suendermann@usz.ch; volkmar.falk@usz.ch).

Color versions of one or more of the figures in this paper are available online at <http://ieeexplore.ieee.org>.

Digital Object Identifier 10.1109/TBME.2013.2273496

I. INTRODUCTION

STENTS are used in various fields of medicine as a means to dilate and stabilize vessels or other body cavities. Most stents show a tube-like geometry (or a geometry that is composed of several tubes) and have a mesh structure that allows radial compression (*crimping*) and expansion. Stents are manufactured from metal or polymers, can be self-expanding or are expanded by the means of an inflatable balloon introduced into the stent before crimping, and, depending on the application, vary in diameter as well as length. Across all sizes, shapes, materials, and ways of the deployment, all stents rely on a mechanical equilibrium between the forces trying to embolize (dislocate) them and a radial force that provides the fixation of the stent inside the vessel. While in many cases this radial force and the dilatative effect it has on the surrounding tissue is an intended therapeutic necessity that aims at treating a disease-induced stenosis, it also gives rise to complications and adverse effects. An excessive radial force leads to the irritations of endothelial cells, which can evoke the thrombogenic processes and thereby cause restenosis [1], impede the conductivity of cardiac cells [2], or in extreme cases may lead to vascular rupture [3].

Transcatheter aortic valve implantation (TAVI) is a technique for the treatment of aortic stenosis in high-risk patients with severe aortic stenosis. The TAVI procedure uses a stented valve replacement that is implanted inside the natural, dysfunctional aortic valve under beating-heart conditions [4]. The procedure is well established and clinical trials have proven its effectiveness and safety [5]. Nevertheless, TAVI is still associated with a number of adverse effects, of which paravalvular leaks (diastolic blood flow from the aorta to the left ventricle through gaps between the prosthesis and the surrounding tissue) [6] and conduction abnormalities, which require treatment with a permanent pacemaker [7], are the most common.

A. Study Aim

We propose means to analyze the biomechanical status of an implanted stent (or other deformable implant) *in vivo* by combining methods from medical-image analysis, image-based modeling, and biomechanics. The method makes use of the stent's superelastic properties, which define a relation between the mechanical load imposed by the surrounding tissue and the state of deformation of the implanted stent, and is based on medical images, which could be, depending on the application, generated during or after an implantation. The deformed shape

of the implanted stent is extracted from the images, and the mechanical forces acting on the interface between the device and the surrounding tissues are estimated as a means to quantitatively assess the quality of a treatment and to predict mid- and long-term effects such as stent healing, restenosis, or aneurism regression. Moreover, the method can be applied in order to create *in vivo* ground truth for the evaluation of predictive simulation systems and to provide stent developers with *in vivo* data about the conditions under which the stents are employed.

Here, we present an exemplary implementation of the concept applied to the stent of the Medtronic CoreValve revalving System, which is one of the two most frequently used TAVI prostheses. Like any stent, TAVI stents are fixated against the hydrodynamic and hydrostatic forces acting on it in their longitudinal direction through the radial forces at the interface between the stent and host tissues [8]–[10]. The valve which is carried by the stent is intended to seal the left ventricle against blood flowing back from the aorta during diastole. A sufficient radial force along the complete perimeter of the aortic annulus is required to ensure this seal and to prevent paravalvular leaks. Excessive radial force may lead to rupture of the annulus or the ascending aorta and is suspected to cause conduction abnormalities (atrioventricular node blocks and left bundle branch blocks) through the stress imposed onto the conductive fibers.

B. Related Work

Biomechanical modeling and analysis of stenting procedures have been identified as key components in attempts to optimize the stents and stent deployment strategies. In order to better understand and be able to predict the behavior of stents inside the human body, various models of the stents as a mechanical device and of the vascular and surrounding tissues as biomechanical components have been presented [11]–[14].

Mummert *et al.* [10] investigated the deployment of braided Nitinol stents in explanted porcine and ovine hearts. Crimping diameters versus radial force, pullout, aortic annulus deformation, and friction between the stent and the aortic tissue were looked at. They found a radial dilatation of 2.5 mm necessary to anchor the stent against embolization. The differences in stent shape and structure (they used braided stents whereas the CoreValve like most vascular stents is manufactured from one Nitinol tube by laser cutting and shape setting) and implantation environment (dead, yet nonpathologic animal valves versus living, yet heavily calcified human valves) make their findings not directly applicable to clinical scenarios.

Unlike the direct measurement of the stent-interaction forces described in [10], our approach employs an indirect measurement. For that purpose, a numerical model of the stent's superelastic behavior is required. Most finite-element stent models that deal with TAVI focus on simulating balloon expandable stainless steel stents, which exhibit elasto-plastic material behavior (e.g., [9], [11], [15]). Mechanical models of the CoreValve stent, which this paper focuses on, have been presented previously, e.g., by Tzamtzis *et al.* [16]. They used a tetrahedral meshing procedure in order to obtain a finite-element model for the stent. Such solid element models must be treated with special

care, when it comes to slender structures that are subjected to large rotation bending. Depending on the selection of the exact element type with its assigned integration scheme and on the grade of the meshing itself, undesired numerical side effects such as shear locking or hourgassing, may occur. Necessary countermeasures often include mesh refinement until convergence is reached. This, however, increases model complexity, raising computational cost, and jeopardizing numerical stability. Detailed investigations concerning element type selection for the simulation of stent expansion processes were performed by Hall *et al.* [17], who recommended beam elements for reasons of stability and efficiency as used by [15]. This modeling approach has not yet been applied to CoreValve stents, which are one order of magnitude larger and not cylindrical.

Most literature in the context of biomechanics, FEM, and TAVI, is aiming at the development of predictive models, i.e., models for preinterventional *in-silico* prediction of intervention outcome. Our approach, however, uses FEM for retrospective analysis of the observed postinterventional situation of the aortic root. A similar concept has been proposed by Ganguly *et al.* in [18]. They applied rotational angiography to patients with stents in the femoral artery to acquire 3-D image data of the implanted stents and to extract the centerlines of the stents from these images. They studied the accuracy of this method for analyzing stent deformation and were able to show a very good agreement of the extracted data with the physically measured values in *in vitro* experiments. Their work does not include the integration of the measured displacement with a mechanical simulation. They studied vascular stents with a cylindrical shape and a very fine-grid structure. Therefore, their analysis is limited to a polynomial representation of the stents' centerlines rather than the wires of the stents. For large and complex shaped stents, such as the CoreValve, this approach would not yield sufficient information to describe the deformation required to compute the radial forces.

II. METHOD

The shape of the CoreValve stent is shown in Figs. 1 and 2. It consists of a nickel-titanium alloy known as Nitinol. As reported in [19], the 165 intersection points of the stent's mesh structure can be categorized into 11 layers consisting of 15 points, so that the points in each layer describe a circle around the stent's longest axis. These points are connected by 30 strings running from the proximal to the distal end. At the distal end of the stent, two hooks are attached, which are required to pull the stent into the delivery system through a funnel-shaped device (see Fig. 2). Together with the peaks of these hooks, a labeled set of 167 landmarks can be defined.

A. Method Overview

An overview of the proposed method is given in Fig. 1. It consists of four principal steps. In image preprocessing step, image analysis algorithms are employed to detect the region of interest that contains the stent in a CT image and to suppress high-intensity voxels which do not belong to the stent. The subsequent stent reconstruction step extracts the grid

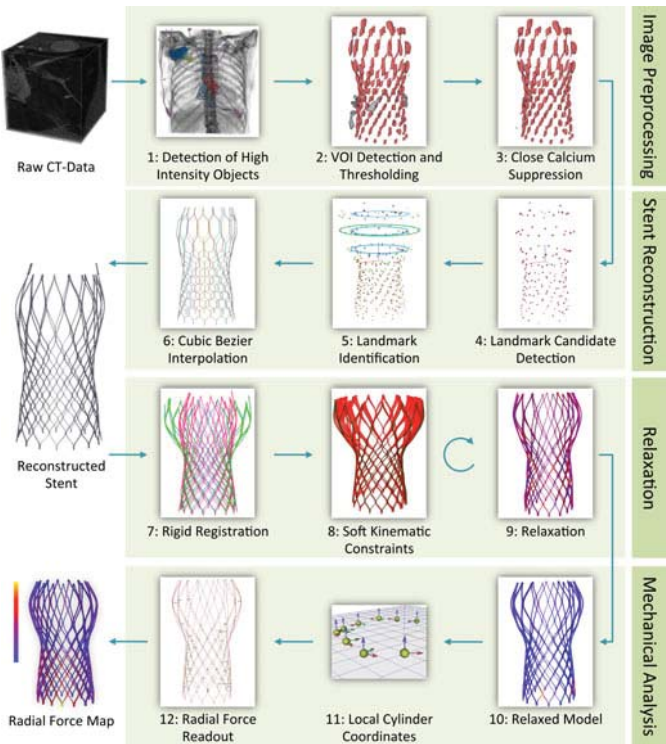


Fig. 1. Method overview.

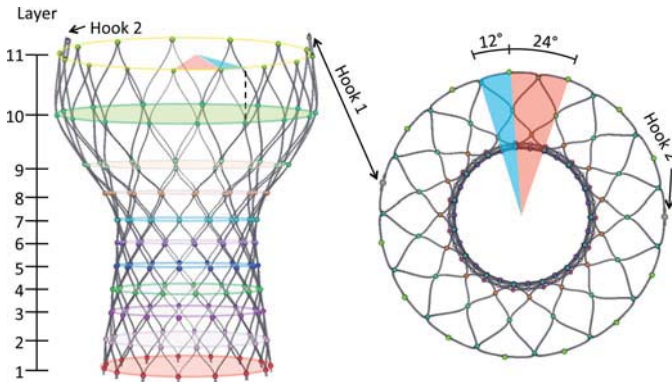


Fig. 2. Shape and structure of the Medtronic CoreValve stent. The balls mark the 167 grid points which are appointed to 11 layers, each visualized as a circle. On these circles, the landmarks have a distance of 24°, neighboring layers are shifted by 12°. The regularity of the structure allows for estimating the positions of the intersection points in the Layers ($j - 1$) and ($j + 1$) from the known intersection points in Layer j .

points of the stent and a model of the deformed stent is created using Bezier interpolation. The displacements of the grid points are employed as kinematic boundary conditions to a mechanical model of the stent. A relaxation step is included, which allows the grid points to migrate within a small region toward a minimum of the deformation energy in the stent, to compensate for landmark localization errors. This relaxation step is alternated with a radial straining step in order to bias the relaxation to the normal and the axial direction. After finding a force equilibrium, the reaction forces between the stent and the surrounding tissues are read out along the radial direction at each grid point. The

work steps and the algorithms used in the proposed method are explained in Section II-B –E.

B. Image Preprocessing

The image processing algorithms were implemented in Java 1.6 using the open-source IDE Eclipse. For the visualization of the images and extracted models, the open-source software framework OpenMAF 2.0 was used.

1) Imaging: ECG-gated Chest CTs were collected from patients who had undergone CoreValve implantation and given their consent for accessing their data. The images were reconstructed at a spatial resolution of 0.7 mm or finer and at 10 time-steps over the cardiac cycle, but not in all the cases were all reconstructions still available on the PACS when the images were retrieved for this study. Of all the available reconstructions with sufficient resolution, we chose the best systolic one. The datasets contained a field of view ranging from the abdomen to the level of the shoulders in caudo-cranial direction, covering the full depth and width of the chest and were acquired between 2 and 841 days (median: 328) days after the implantation.

2) Suppression of High-Intensity Objects: The CoreValve stent is, in most cases, not the only metallic object seen in the images—extracorporeal ECG wires, pacemakers, and other kinds of implants have a similar X-ray density. In a preprocessing step, all the high-intensity objects which do certainly not belong to the stent are detected and suppressed. The selection of these objects is based on cluster-size analysis. The stents' wires are about 0.3 mm thick. At the intersection points, two contacting wires reach a thickness of about 0.7 mm. When applying a high threshold of 2000 HU (Hounsfield Units) to the image, the stent will break into many small voxel clusters due to partial-volume effects. After thresholding, the connected clusters of the high-intensity voxels are created and the number of voxels in each cluster is counted. The maximum number of voxels in a cluster depends on the image resolution, but will never exceed 300 (based on a theoretical resolution of $0.25 \times 0.25 \times 0.25 \text{ mm}^3$ and the volume of the largest cluster at the distal hooks of the stent which is $\approx 5 \text{ mm}^3$). A safety margin of 100 voxels is added to this value. All clusters larger than 400 voxels are erased.

3) Stent Segmentation: After the suppression of all irrelevant metal objects, presegmentation is performed in order to extract a volume of interest (VOI) that contains the stent. A high threshold (1700 HU) is applied to generate the seed voxels for detecting the remaining objects with high intensity in the image. In Fig. 3(a), all voxels in the region of the stent which remain after applying this threshold are marked red. These voxels are used as seed points for a region growing step that connects all the neighboring voxels with an intensity of 650 HU or larger. The result of this second step on the stent region can be seen in Fig. 3(b).

4) Calcium Suppression: The segmentation method described to this point is based on a combination of thresholding and region growing. Both methods are prone to oversegmentation errors, which in this case would lead to an inclusion of the nearby calcifications into the stent segmentation—the image intensity of calcium can reach values of 1600 HU and more.

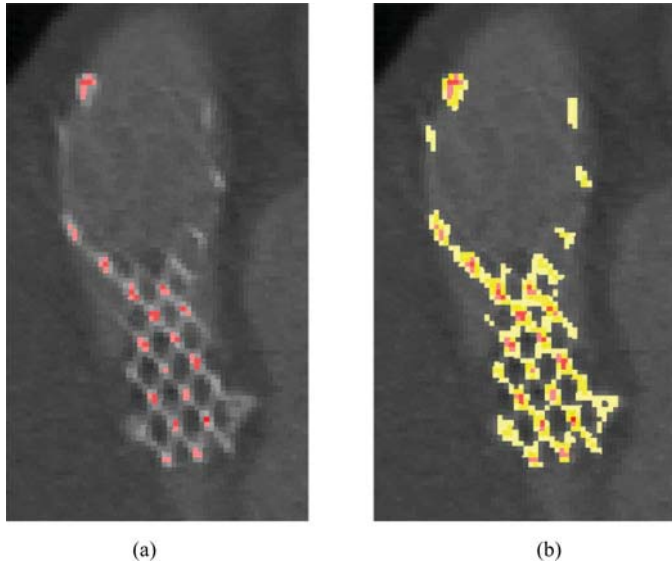


Fig. 3. (a) Seed points for the region growing after thresholding in the stent region (red). (b) Result of the region growing in the stent region.

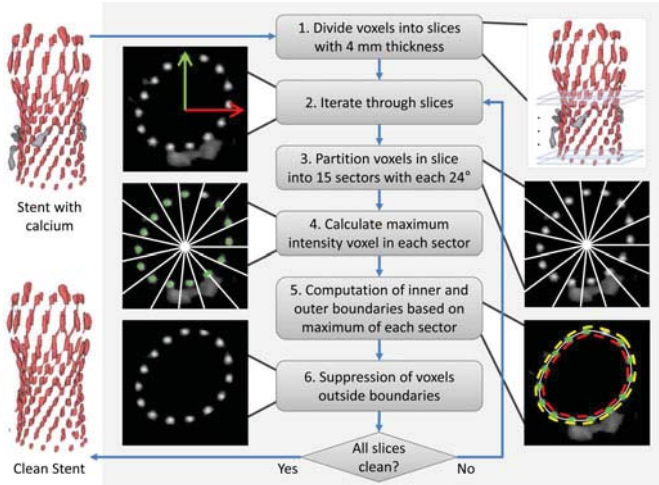


Fig. 4. Separation of the stent voxels and the calcium voxels.

The final step of the image preprocessing is the suppression of those voxels represent the calcium clusters at the stent's perimeter. The method applied for the calcium suppression is summarized in Fig. 4. The VOI containing the stent is sliced in 4 mm steps along an approximation of the stent's centerline computed as the longest axis of the VOI. Each slice is divided into 15 sectors of 24° around the central axis. In each sector, the local intensity maxima are found and the maximum closest to the center is selected. Based on the maxima in all sectors, the stent boundaries are approximated according to the known thickness of the strings. The voxels outside of these boundaries are labeled as calcium and not considered for the stent reconstruction.

C. Stent Reconstruction

The objective of the image preprocessing performed to this point was the identification of the voxels which very likely belong to the stent. In the following, these candidates are identified

among those voxels which are the most likely to represent the intersection points of the stent in its deformed configuration. This step is relying on the fact that, due to the partial-volume effects, the intensity of the voxels at the intersection of two strings is higher than anywhere else in the stent. The minimal distance between two intersection points is in any case larger than 2 mm. A nonmaximum suppression with a kernel size of 2 mm is applied to identify the local maxima within the stent volume. These maxima are considered as candidates for the identification of landmarks that mark the intersection points. Noise, incompletely suppressed calcium, and other effects can yield false positives in the list of landmark candidates. Moreover, the variances in the image quality can result in undersegmentation, i.e., to incomplete sets of landmark candidates. Both the errors need to be corrected in order to create a complete and correct set of 167 landmarks. At this point, prior knowledge about the topology and the geometry of the stent is taken into consideration as a lead in the identification of false candidates, and for the generation of search spaces to find the missing landmarks.

A reference model of the stent in its undeformed (unloaded) state was created based on microCT images of CoreValves that were acquired under no mechanical load (other than gravity).

Principal component analysis is applied to find the center of gravity (mean) and the longest axis of the landmark candidates. The reference model is registered according to this axis and the mean. The remaining degree of freedom, rotation around the long axis, is determined according to the clamp points at the distal end of the stent.

For an identification of the correct landmark candidates and in order to assign the landmarks to the correct layer, a sliding plane is applied, which scans the candidate cloud along the longest axis of the stent. The plane through the second highest layer of the undeformed stent model (Layer 10) is computed. All the landmark candidates which are within a vertical distance less than 3.8 mm (closer to this plane than the two neighboring planes) are considered the candidates for this layer. The candidates are sorted according to their angle around the central axis of the stent. In the unloaded state, the angular distance between two neighboring intersection points is 24°. The selection algorithm picks those 15 landmark candidates which best fulfill this criterion and assigns them to Layer 10. Starting from Layer 10, an iterative search is performed to identify the correct landmarks in all layers based on the knowledge of the distance between all layers in the unloaded state and the alternating rotation of approximately 12° between the intersection points in neighboring layers (see Fig. 2). Thus, the likelihood of a candidate to represent an intersection point of the stent can be rated. In each layer, those 15 landmarks with the highest level of confidence are selected.

Once all the landmarks are localized, identified, and labeled, the Bezier control polygons are constructed that define the 30 centerlines of each of the stent's strings from the proximal to the distal end according to the constraints defined in [19].

D. Relaxation

The image processing pipeline generates an estimate for the position of each intersection point of the stent. The relation

between neighboring intersection points is used to separate the true and the false landmark candidates. Nevertheless, up to this point in the algorithm, the position of each landmark is estimated independently of its neighbors. Image resolution, noise, and artifacts will inevitably create an uncertainty in these positions, which we quantify in Section III-C. Thus, the observed positions $P_0 = \{\mathbf{p}_{i,0}, i \in [1, 165]\} \subset \mathbb{R}^3$ delivered by the process so far will differ from the true positions $\hat{P} = \{\hat{\mathbf{p}}_i, i \in [1, 165]\}$, and for each landmark an unknown landmark positioning error $\mathbf{e}_{i,0} = \mathbf{p}_{i,0} - \hat{\mathbf{p}}_i \in \mathbb{R}^3$ is to be considered. The error vector $\mathbf{e}_{i,0}$ is superimposed on the actual displacement vector $\hat{\mathbf{d}}_i$ of that intersection point which locally describes the deformation of the stent from its unloaded state to the deformed state, so that the measured displacement is $\mathbf{d}_{i,0} = \hat{\mathbf{d}}_i + \mathbf{e}_{i,0}$.

A mechanical model of the stent implemented in Abaqus 6.10-EF1 (Dassault Systemes, Vélizy-Villacoublay, France) is applied as a means to reduce the landmark positioning error $\mathbf{e}_{i,0}$ in order to get a more accurate estimate of the node displacement $\hat{\mathbf{d}}_i$.

1) Beam Model: A finite-element model of the stent is set up using structural beam elements. MATLAB R2013a (The MathWorks, Natick, MA, USA) is used to generate the Abaqus input file. First the control polygon of each string of the stent in the stress-free reference configuration is sampled equidistantly. The neighboring nodes within a string are used to define the local end points of a two point beam element. Additionally, the beam elements require the definition of a cross-sectional geometry and its orientation. For the CoreValve stent this cross-sectional geometry is not constant over each string. This variation is implemented and controlled by using linear functions of the arc length over every spline segment. The element type chosen for this application is the Timoshenko-based B31 element [17]. This selection is not motivated by a strong need of the transverse shear compliance but by the fact that these particular elements are well suited to simulate situations involving large deflections in 3-D space. Assigning beam elements in this way, leads to a continuous beam structure for each of the 30 strings. The points at the intersections of neighboring strings are locally approximated as rigid bodies. For this purpose, both nodes of each intersection are coupled kinematically in the corresponding manner. This is implemented using the beam-type constraint of Abaqus. Coupling of the strings completes the structural model of the stent. Convergence analysis was employed to define the optimal resolution of the model [20]. The final mesh consists of 252 linear beam elements per string, resulting in 7560 elements for the whole stent.

A constitutive model of the stent material is added to the model. Nitinol exhibits superelastic properties, which are required for the crimping and deployment of the stenting procedure. At this stage, we are interested in the final equilibrium between the tissue and stent. In the configurations that we found in the actual patient data, the strain rates in the stent remain within the linear low-strain regime of Nitinol. By taking the stent model from a stress-free reference state directly to the end configuration, we omitted the high-strain states present in the crimped stent. This allowed us to describe the stent material

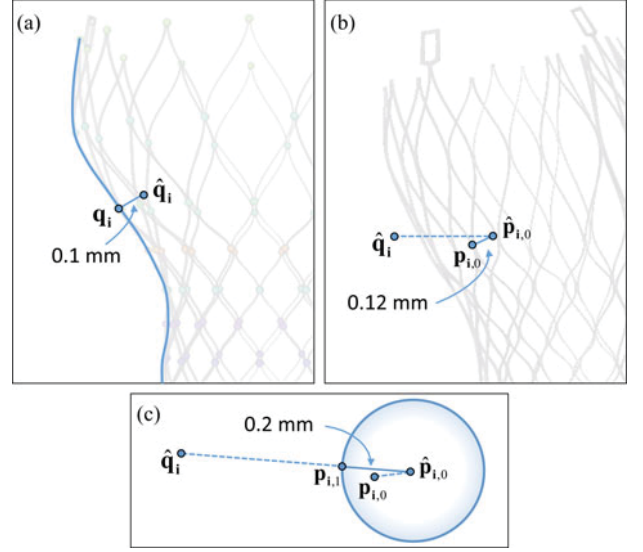


Fig. 5. (a) A nonlinear spring is fixed between a intersection point \mathbf{q}_i and a virtual pivot point $\hat{\mathbf{q}}_i$. (b) $\hat{\mathbf{q}}_i$ is pulled to a position $\hat{\mathbf{p}}_{i,0}$ lying 0.12 mm inside of the measured landmark position \mathbf{p}_i . (c) Spring allows the intersection point to move to a position $\mathbf{p}_{i,1}$ of minimal strain within a radius of 0.2 mm.

with a linear-elastic material model, characterized by the two parameters Young's modulus E and Poisson number ν . The latter is commonly set to 0.33. Young's modulus E of Nitinol is reported between 40 and 75 GPa in the literature [16], [21]. For our beam model of the CoreValve stent, a value of 60 GPa delivered the best experimental results (see Section III-A).

2) Soft Kinematic Constraints: Due to the uncertainty of the landmark extraction, the deformed coordinates cannot directly be applied as the kinematic boundary conditions. This would lead to a strong noise amplification in the axial and the tangential directions of the reaction forces and render the desired radial components highly unreliable. To allow the stent's internal mechanics smoothing out landmark localization errors, 1-D force elements with nonlinear force laws are used to communicate between the measured displacements and the grid points of the stent model as shown in Fig. 5.

For each intersection point \mathbf{q}_i of the undeformed stent model, a virtual pivot point $\hat{\mathbf{q}}_i$ is created at a distance of 0.1 mm along the local normal of the stent surface. A force element (spring) f_i is defined between $\hat{\mathbf{q}}_i$ and \mathbf{q}_i with the force law

$$d_i = \|\mathbf{q}_i - \hat{\mathbf{q}}_i\|_2 \\ s(d) = \begin{cases} 0^N / \text{mm}, & d < 0.1 \text{ mm} \\ 0.1^N / \text{mm}, & 0.1 \text{ mm} \leq d < 0.2 \text{ mm} \\ 50^N / \text{mm}, & d \geq 0.2 \text{ mm} \end{cases} \\ f_i = s(d_i) \cdot (\mathbf{q}_i - \hat{\mathbf{q}}_i)$$

To softly constrain the model with the measured displacements $\mathbf{d}_{i,0}$, the pivotal point $\hat{\mathbf{q}}_i$ is pulled to a location

$$\hat{\mathbf{p}}_{i,0} = \mathbf{p}_{i,0} - 0.12 \cdot \mathbf{r}_{i,0}$$

along a radial vector $\mathbf{r}_{i,0}$, that is computed as the normalized projection of the vector pointing from $\mathbf{p}_{i,0}$ to the centerline of the stent onto the plane, that equalizes the 15 intersection points on layer $l_i = \lceil \frac{i-1}{15} \rceil \in [1, 11]$.

The implicit solver of Abaqus is used to find a minimum of the strain energy in the stent and the virtual spring elements. The force law is selected in such a way that the physical intersection points have the freedom to move inside a 0.2 mm sphere around the displaced pivotal points $\hat{\mathbf{p}}_{i,0}$ to positions $\mathbf{p}_{i,1}$. This allows the stent to find a global minimum of its potential energy, thus smoothing out the high-force spikes in undesired directions.

3) *Incremental Stent Relaxation*: An incremental routine using alternating straining and relaxation steps is employed to move the landmark coordinates $P = \{\mathbf{p}_i, i \in [1, 165]\}$ from the initial positions P_0 to more accurate positions P_n . Starting with the initial landmark coordinates P_0 , the first relaxation step is computed as described previously to yield the landmark coordinates P_1 , and the spring forces $\mathbf{f}_{i,1}$ are reported. P_1 is fed back into the relaxation algorithm as the new initial landmark coordinates, yielding the landmark coordinates P_2 and the spring forces $\mathbf{f}_{i,2}$. The relaxation of step $k = 2$ is computed as

$$\rho_k = \sum_{i=1}^{165} \|\mathbf{f}_{i,k}\|_2 - \|\mathbf{f}_{i,k-1}\|_2.$$

The iteration is continued until $\rho_k < 0.01 \cdot \rho_2$ and $P_n = P_k$ is reported as the final intersection point set. The rationale for this stop condition lies in the aspect ratio between the forces produced by the stent in response to the radial, axial, and tangential displacement of the nodes. When we pull the pivot points inward on a 2-D plane through the measured coordinate and then allow the intersection points to migrate inside a sphere around the pivot point, the axial and tangential components of the internal forces in the stent will dominate the direction of the point migration, as the axial and tangential stiffness of the stent exceeds its radial stiffness by several orders of magnitude (see Section IV-B). After a couple of iterations (in practice 3 to 5), all nodes moved to a local minimum of the overall stent energy, with respect to the axial and tangential deformation, and the annealing of force (energy) between two steps starts to decline. From that point on, the stent will primarily use the radial degree of freedom to relieve itself of the radial displacement.

E. Mechanical Analysis

At each intersection point $\mathbf{p}_{i,n}$, a local coordinate system is defined through a radial, tangential, and axial vector. In Fig. 1, these directions are indicated by the red (axial), green (radial), and blue (normal) arrows at each node. The reaction forces $\mathbf{f}_{i,n}$ in the springs are transformed to these coordinate systems and only the radial component is used for the analysis of the radial force between the stent and the tissue. The average radial force F_j per layer is computed as

$$F_j = \frac{1}{15} \sum_{i=1}^{15} \|\mathbf{f}_{15j+i,n}\|_2.$$

III. EXPERIMENTAL SETUP

The performance of each system component as well as of the overall system was investigated in a series of experiments. In the following sections, the different experiments are described.

The results of each experiment and discussion of these findings is given in Section IV.

A. Mechanical Model Verification

Most experimental protocols for stent testing, involve a two-plate crush procedure as defined by ISO 25539-2:2008 [16]. Performing and simulating the crush tests is challenging by default, since nonlinearities arise from solving the mechanical contact. The CoreValve's curved geometry leads to additional difficulties. To avoid these issues, we employed two-point tensile tests. The stent was clamped at two points and then subjected to tension. Internally, the stent reacted with a complex mode of deformation involving bending, tension, and torsion of its struts. Externally, it acted as a 1-D, nonlinear spring connecting the two clamping points. The characteristic curve of that spring was measured experimentally for three different pairs of clamping points and compared to the simulated reaction to the same tension as computed with our beam model.

B. Stability of the Image Processing Pipeline

21 CT datasets where available for testing. The automatic preprocessing and landmark extraction algorithms were run on all 21 images in order to test whether they are able to locate all the landmarks in all the images.

C. Estimation of Reconstruction Accuracy

The accuracy of the automatic landmark localization was estimated by comparing the results with manually extracted landmark positions, which were defined by three human observers using a graphical interface. Due to the very time-consuming nature of the manual landmark localization, the comparison was limited to five datasets in which all the three observers localized all 167 landmarks. The three different locations \mathbf{p}_{ij} , $i \in \{1, 2, \dots, 167\}$, $j \in \{1, 2, 3\}$ given by the three observers for each landmark were used to define $\mathbf{S}_i(\hat{\mathbf{p}}_i, r_i)$, the smallest sphere which contains the triangle \mathbf{p}_{ij} . The center and radius of this sphere are identical to the center \mathbf{m}_{ci} and radius r_{ci} of the circumscribed circle for the triangles, where all the interior angles are $< 90^\circ$. For the blunt-angled triangles, the sphere is defined by the center of the longest edge and half its length:

$$\mathbf{S}_i = \begin{cases} S\left(\frac{\mathbf{p}_{i0} + \mathbf{p}_{i1}}{2}, \frac{\|\mathbf{p}_{i0} + \mathbf{p}_{i1}\|}{2}\right), & \angle(\mathbf{p}_{i0}, \mathbf{p}_{i2}, \mathbf{p}_{i1}) \geq 90^\circ \\ S\left(\frac{\mathbf{p}_{i0} + \mathbf{p}_{i2}}{2}, \frac{\|\mathbf{p}_{i0} + \mathbf{p}_{i2}\|}{2}\right), & \angle(\mathbf{p}_{i0}, \mathbf{p}_{i1}, \mathbf{p}_{i2}) \geq 90^\circ \\ S\left(\frac{\mathbf{p}_{i1} + \mathbf{p}_{i2}}{2}, \frac{\|\mathbf{p}_{i1} + \mathbf{p}_{i2}\|}{2}\right), & \angle(\mathbf{p}_{i1}, \mathbf{p}_{i0}, \mathbf{p}_{i2}) \geq 90^\circ \\ S(\mathbf{m}_{ci}, r_{ci}), & \text{otherwise.} \end{cases}$$

For each automatically identified landmark, an acceptance function A is defined depending on a parameter α which accepts a landmark if it is not further away from any of the three manual landmarks \mathbf{p}_{ij} than the radius of the sphere \mathbf{S}_i multiplied with the factor α :

$$A_{i,\alpha}(\mathbf{p}) = \begin{cases} 1, & \min_j (\|\mathbf{p}, \mathbf{p}_{ij}\|) \leq \alpha \cdot r_i \\ 0, & \text{otherwise.} \end{cases}$$

With this, for a complete set of automatically localized landmarks \mathbf{p}_i , $i \in \{1, \dots, 167\}$, the acceptance rate \bar{A} for one stent is defined as a function of α :

$$\bar{A}(\alpha) = \frac{\sum_{i=1}^{167} (A_{i,\alpha}(\mathbf{p}_i))}{167}.$$

To better relate these accuracy measurements to the radial force, the effect of the localization error onto the effective *radial strain* was considered. We computed for each layer k of the stent the cross-sectional area A_k as the area circumscribed by a closed polygon formed by the 15 intersection points on that layer in the undeformed configuration. For each of the five patients in this arm of the study, four different versions of the intersection point sets in the deformed configuration were available, three were defined manually ($j \in \{1, 2, 3\}$), and one automatically ($j = 4$). For each of these cases j and on each layer k we computed the deformed cross-sectional area A_{jk} . The radial strain ϵ_{jk} is defined for each layer k and the dataset j by relating the root of A_{jk} to the root of A_k :

$$\epsilon_{jk} = \frac{\sqrt{A_k} - \sqrt{A_{jk}}}{\sqrt{A_k}}.$$

D. Validation of Error Reduction Using Incremental Relaxation

The ability of the incremental method to reduce the landmark localization error was assessed using realistic, yet artificial, displacement fields as ground truth and perturbing them by random noise. Random displacement vectors were added to the intersection points in deformation cases \tilde{P} to create noisy landmark sets P_0 . The direction of these vectors was randomized according to a uniform distribution; the norm of the vectors follows a normal distribution with a mean of 0.74 mm and a standard deviation of 0.16 mm.

The position of each node was traced over the relaxation process. The node error $e_{i,k}$, mean layer error $\epsilon_{j,k}$, and overall mean error E_k were computed for each step k :

$$\begin{aligned} e_{i,k} &= \|\mathbf{p}_{i,k} - \hat{\mathbf{p}}_i\|_2 \\ \epsilon_{j,k} &= \frac{1}{15} \sum_{i=1}^{15} e_{15j+i,k} \\ E_k &= \frac{1}{11} \sum_{j=1}^{11} \epsilon_{j,k}. \end{aligned}$$

As an additional measure for the geometric accuracy, the projected circumference in each layer was computed for the ground truth \tilde{P} as well as for each P_i . Therefore, the landmarks in each layer were projected to the equalizing plane and the circumferences of the polygons spanned by the projected points were computed. After each step k , the circumferential error $\gamma_{j,k}$ was computed for each layer as the difference between the projected circumference ϵ_j in the noise-free dataset and the projected circumference $c_{j,k}$. As a global measure for accuracy, the mean Γ_k of the absolute values of $\gamma_{j,k}$ was computed for each increment k as

$$\Gamma_k = \frac{1}{11} \sum_{j=1}^{11} |\gamma_{j,k}|.$$

Besides the geometric accuracy, we also analyzed the difference between the radial interaction forces in the ground truth and the output after each increment and computed force errors per node, per layer, and for the whole stent in each step k :

$$\begin{aligned} \phi_{i,k} &= \left\| \mathbf{f}_{i,k} - \hat{\mathbf{f}}_i \right\|_2 \\ \varphi_{j,k} &= \sum_{i=1}^{15} e_{15j+i,k} \\ \Phi_k &= \sum_{j=1}^{11} \varphi_{j,k}. \end{aligned}$$

IV. RESULT AND DISCUSSION

A. Computational Cost

Depending on the image size and the amount of high-intensity voxels and voxel regions that needed classification, the image preprocessing step took between 120 and 240 s per dataset. The extraction of landmarks for the stent reconstruction took between 30 and 60 s. Both steps were conducted on a workstation with an Intel Xeon E5647 processor with six cores (12 threads) at 2.4 GHz equipped with 12 GB of RAM running Microsoft Windows 7. The implementation was not optimized with respect to the computation times or memory usage. The relaxation step took 90 s on an Intel Core i7-3770K CPU with four cores (8 threads) at 3.50 GHz equipped with 8 GB of RAM running Linux. The force readout and postprocessing took around 1.5 s on the same machine.

B. Mechanical Model Verification

Three tension experiments were conducted. In the first experiment, the two distal hooks were clamped for the tension test, creating tension along a radial direction. This yielded relatively small forces, as primarily bending of the thin stent wires occurred. The second experiment was an axial test, with the stent being clamped at the distal and proximal end of one string. This resulted primarily in the axial tension of struts, yielding relatively large reaction forces. Finally, a superimposition of both effects was achieved by clamping one distal hook and a proximal point underneath the opposing hook (see Fig. 6).

The blue line in Fig. 6 shows for the third configuration the tension force that was measured continuously in one clamp while slowly increasing the distance between the two clamps by 3.8 mm. The red line shows the simulation result for the same setup. For larger deflections the numerical model leads to a higher global stiffness of the stent, which is to be expected for an implementation with a linear-elastic material model. However, the estimations of the occurring physiological strains which are present in the implanted equilibrium state after TAVI are not expected to exceed the limit imposed by this choice of the constitutive model.

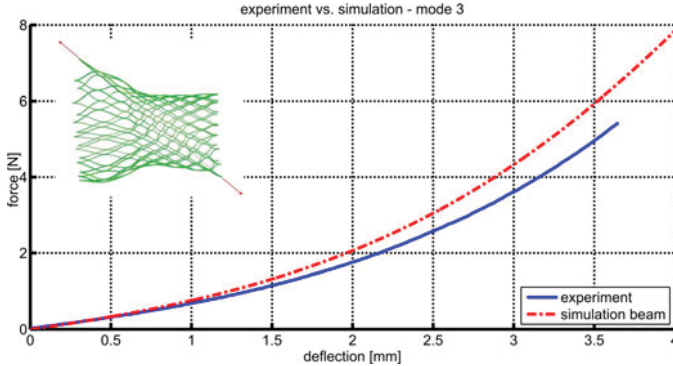


Fig. 6. Validation of the beam model. The image shows how the stent model was loaded to create a superimposition of the radial, axial, and tangential strain. The plot shows the simulated (red) and the experimentally measured (blue) reaction force in the clamp over the linear deflection that was applied by increasing the distance between the clamps.

C. Stability of the Image Processing Pipeline

The identification of the stent among all the high-intensity objects in the image was successful in all 21 cases. The bounding boxes derived from each of the 21 datasets were visually approved to be consistent with the area that contained the stent. Thresholding and calcium suppression in all cases delivered a result which passed qualitative visual assessment. At this point no accuracy measurement was performed, the assessment was only looking for extreme over- or under-segmentation errors. The landmark identification was able to extract all 167 landmarks (including the distal hooks) in 10 datasets. In eight additional datasets, one or both of the landmarks representing the distal hooks could not be localized but all 165 intersection points were found. In three datasets, landmark localization failed. Two of these cases showed motion artifacts in the form of double-images of the stent in the aortal region; one image was cut off to not contain the complete stent. These three datasets were not considered for the subsequent analyses, leaving 18 cases for testing the relaxation step and extraction of forces. Adding the one or two missing hook landmarks in those ten datasets where automatic landmark localization did not find them, would require user interaction of 1 or 2 minutes, including the loading of cases and landmark clouds, the manual localization of the missing landmarks, and the export of the fixed landmark cloud. Since the radial forces administered to the aorta through these hooks on the distal end of the stent are negligible for the overall equilibrium, they were omitted in the mechanical model described in Section II-D.

D. Validation of Reconstruction Accuracy

The mean landmark localization error over all five datasets was $0.37 \text{ mm} \pm 0.16 \text{ mm}$. Fig. 7(a) shows for each of the patients the accumulated histogram of the distance between the automatically localized landmarks and the nearest manually annotated landmark. To level out differences in the image resolution between the different datasets, the distances were measured in number of voxels. The voxel spacing lay between 0.4 and 0.6 mm. More than 90% of the landmarks were less than

1.6 voxels (0.68 mm) away from the nearest manual landmark. The maximum error was 3.24 voxels (1.3 mm). Thus, the landmark localization error compensation included in the mechanical analysis has to compensate an error of that magnitude.

Fig. 7(b) shows the acceptance function plotted for $\alpha \in [0, 7]$. With an α -value of ≥ 2 , more than 90% of landmarks were accepted. Fig. 8 shows the impact the landmark position uncertainty has on the radial strain.

Overall five datasets and eleven layers per dataset, differences in the radial strain between the models based on the point clouds found by the algorithms, and the point clouds defined by the human observers lay between -2% and 2% . The differences between the three study participants (interobserver variance) were in the same region.

E. Validation of Error Reduction Using Incremental Relaxation

Fig. 9(a) and (b) shows the development of the mean node error E_k , after adding random noise to two different patient datasets (“input”) and after 10 increments of the relaxation. The initial mean error of 0.76 mm is reduced to 0.2 mm after five steps in case one, and to 0.27 mm after four steps in case two. The same plots show the relaxation ρ_k for increments $2 \dots 10$. The convergence criterion was met for $k = 5$ steps in case 1 and $k = 4$ in case 2. The projected circumferential errors for the same test cases are plotted in Fig. 9(c) and (d).

The additional radial strain, which is added by the virtual springs, lead to a reduction of the circumferences in the early phase of the incremental relaxation. In that phase, the degrees of freedom were predominantly used to reduce the axial and tangential noise. This lead to negative values of $\gamma_{j,k}$ for small values of k . Only in the last step before the convergence criterion is reached, the radial error was reduced significantly for each layer. After reaching the convergence criterion, the stent started an approximately linear radial expansion, which lead to an increasingly large circumferential error.

F. Radial Forces

Fig. 9(e) and (g) shows on a logarithmic scale the development of the radial force errors $\varphi_{j,k}$ and Φ_k over the 10 increments k of the relaxation algorithm. Below each plot, in Fig. 9(f) and (h), the decline of the tangential and axial force components is plotted. The vertical red line indicates the step after which the convergence criterion was reached for the relaxation. In both cases, the initial radial force error was reduced by several orders of magnitude, the same is true for the axial and tangential force components. The minimum in the global radial force error Φ_k and for most layer-wise radial force errors $\varphi_{j,k}$ was seen after two steps in the case shown on the left and after three steps in the case shown on the right, while the axial and tangential forces required four steps in the first and five steps in the second case. Thus, the radial error was slightly higher in the final result of the relaxation algorithm than it had been earlier in the incremental routine. Nevertheless, an error reduction of more than 90% is reached.

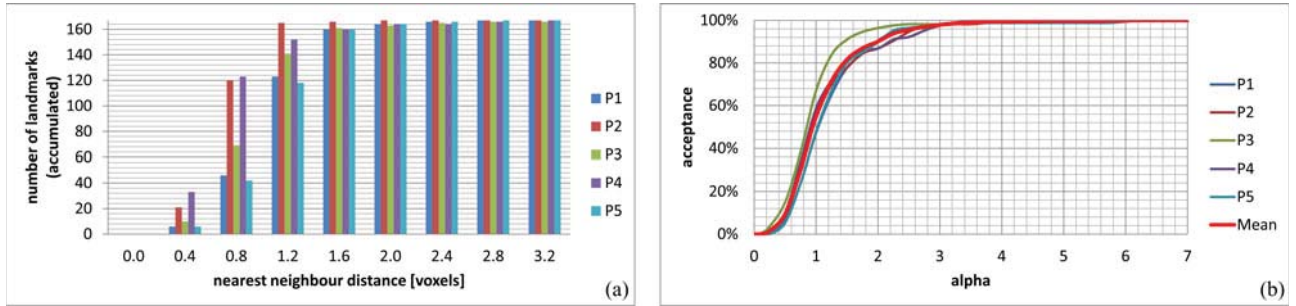


Fig. 7. (a) Accumulated histogram of the distance between automatically found landmarks to the nearest manual reference. Distances are measured in voxels. P1 – P5 denote the five patients of which the manual data was available for the comparison. (b) Value of the acceptance function for $\alpha \in [0, 7]$ for the five patient datasets. The solid red line shows the mean value over all the five datasets.

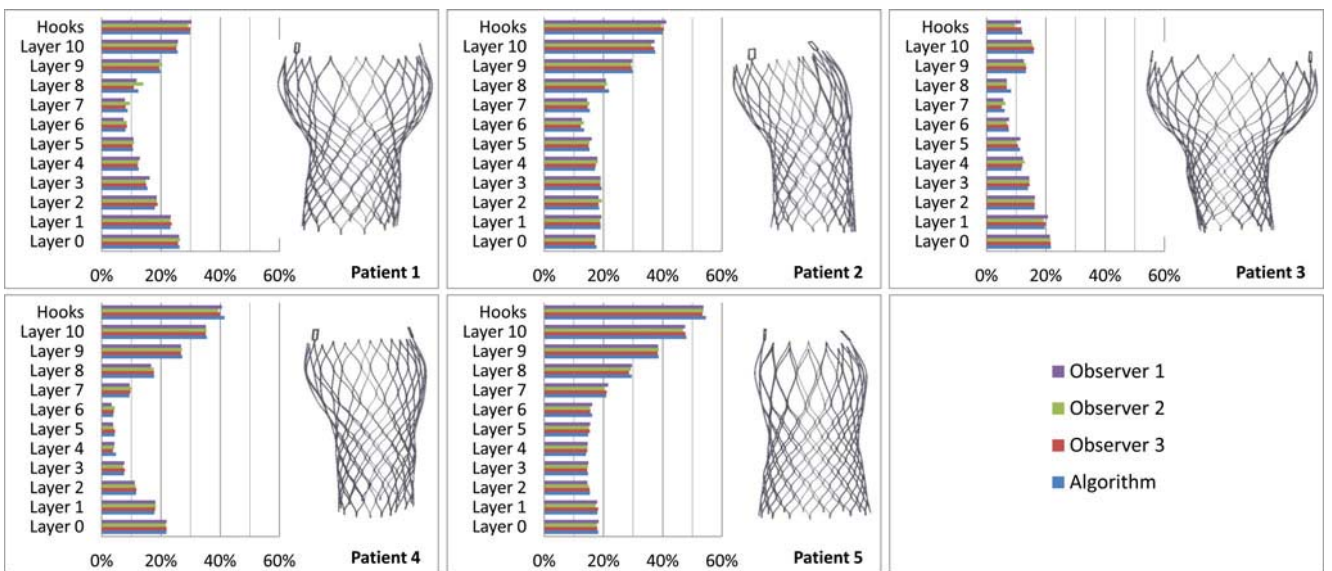


Fig. 8. Radial strain computed based on the three manually defined and one automatically extracted landmark cloud for the five different patients. The pictures shown next to each plot depict the extracted stent shape for the respective patient.

G. Analysis Result

The described procedure was applied to the CT image datasets of 21 patients, stent reconstruction, and derivation of the radial forces was possible in 18 cases (see Section IV-C).

The radial forces measured at the stent nodes ranged from 0.0 N (in areas without contact to the vascular wall) to 2.06 N in one node. The average radial force per node was in the range of [0.3, 0.4] N at the aortic annulus, ≤ 0.1 N in the medial area, and between 0.2 and 0.4 N at the distal end. Visual inspection showed a good correlation between the local maxima of the radial force and calcium clusters (see Fig. 10) as well as regions of large radial strain or ellipticity. For visualization, the point forces given in the intersection points are distributed along the splines interconnecting the intersection points using a linear interpolation scheme.

For comparison with the works of Tzamtzis *et al.*, we computed from our nodal-force data a *hoop force* similar to the definition found in [16]. They reported hoop forces in the range of [3.5, 5.0] N for radial compressions in the range of 5 mm.

When we computed the hoop force for the patient cases with annular deformations in that range, the calculated hoop forces fell into the same range of [3.5, 5.0] N.

V. CONCLUSION AND OUTLOOK

We propose an image-based system for the estimation of the *in vivo* forces on the interface of an implanted Nitinol stent and the surrounding vascular and cardiac tissues. This procedure takes advantage of the superelastic behavior of the Nitinol stent. The system implements a two-staged approach, where the first stage extracts a discrete set of displacement vectors which parameterize the deformation of the stent from a CT image. The second stage includes a mechanical simulation, utilizing the finite-element method as a means to estimate the radial forces that are required to yield the observed deformation. Both stages were verified and validated using real patient data and artificial test data. The extraction of landmarks from the CT images was shown to be not worse than the gold standard, which was represented by the manual annotation of the test datasets by

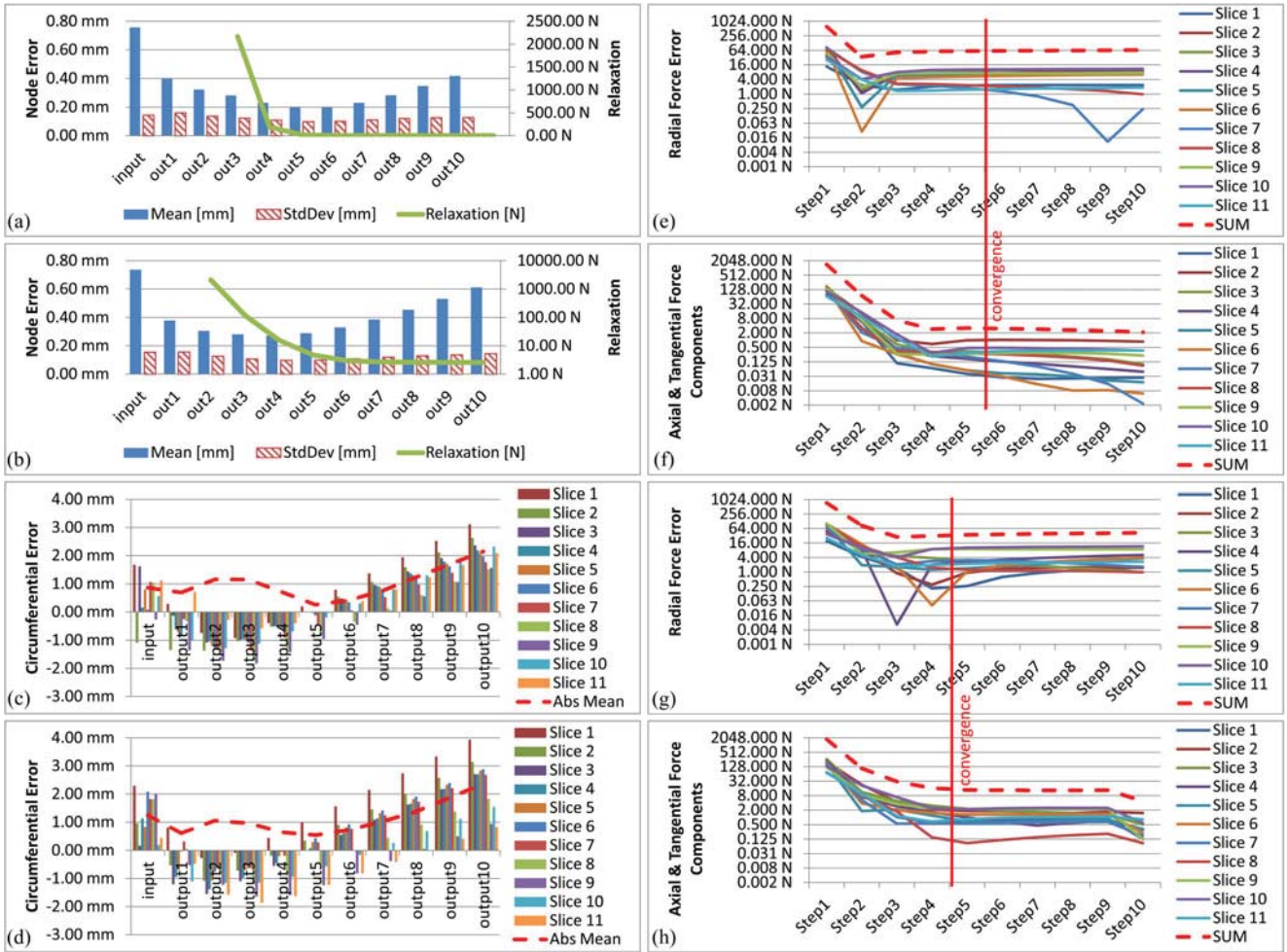


Fig. 9. (a) and (b) Mean and standard deviation of node error E_k in mm (linear, left axis) and relaxation ρ_k in Newtons (logarithmic, right axis) for two test cases with random noise over 10 increments k . (c) and (d) Projected circumferential errors per slice $\gamma_{j,k}$ (bars) and mean of absolute values Γ_k (red dotted line) for two test cases with the artificial noise over 10 increments k . (e) and (g) Radial force errors $\varphi_{j,k}$ and Φ_k over the 10 increments k of the relaxation algorithm for the two patient cases with artificial noise. (f) and (h) Axial and tangential force component in the same increments.

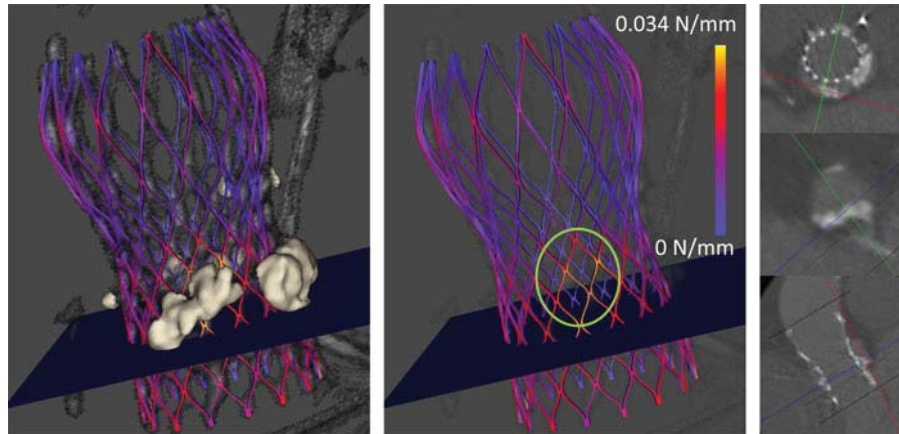


Fig. 10. Influence of calcifications onto force distribution: the calcium cluster in the foreground of the left image causes a local maximum of the radial force, highlighted in the center. The blue plane indicates the level of the native aortic annulus. The images on the right show three cross-sectional visualizations of the calcium cluster as seen in the CT image.

three human observers. The employed mechanism for the FEM-based relaxation of the landmark positions in order to derive a more *natural* stent shape was shown to significantly reduce the measurement uncertainty. This was shown using different error metrics based on the geometric measurements as well as on the analysis of the interaction forces.

With a mean node error below 0.2 mm and a final mean circumferential error below 1 mm, the geometric accuracy of the reconstruction algorithm can be judged as highly accurate, exceeding the resolution of the underlying image data by a factor of two. A large uncertainty remains in the final estimates of the radial force. This uncertainty is caused by the three effects. First, the structure of the stent results inherently in an amplification of the tangential and axial measurement errors, which results in very large tangential and axial force vectors in comparison to the acutally output radial forces. Second, no real contact simulation is employed to yield the true reaction forces normal to some contact surface. Instead, the radial direction is estimated based on a normal vector computed for each layer and a tangential vector computed for each landmark from the two neighboring landmarks in the same layer. Third, as a result of the first two, the projection of the reaction force in the spring element which is used to approximate the radial force is not accurately aligned with the real surface normal. Thus, the radial force is a linear combination of the radial, normal, and axial force components, whereby the aspect ratio between radial and axial/tangential components already results in large errors, even for small deviations from the true surface normal. To compensate for these effects, the actual contact surface needs to be explicitly modeled and simulated.

Our data shows that calcium is the one key factor in the distribution of the radial force on the stent. In future studies we will quantify the impact of the other influences such as the natural annulus shape onto the stent shape and force distribution, and will investigate the changes of both over-the-heart cycle as an effect of the varying blood pressure.

ACKNOWLEDGMENT

The authors would like to thank their colleagues at the Division for Cardiovascular Surgery, the Institute for Diagnostic and Interventional Radiology, and the Division for Cardiology of University Hospital Zurich.

REFERENCES

- [1] J. W. Freeman, P. B. Snowhill, and J. L. Noshier, "A link between stent radial forces and vascular wall remodeling: The discovery of an optimal stent radial force for minimal vessel restenosis," *Connect. Tissue Res.*, vol. 51, no. 4, pp. 314–326, Aug. 2010.
- [2] G. Latsios, U. Gerckens, L. Buellesfeld, R. Mueller, D. John, S. Yuecel, J. Syring, B. Sauren, and E. Grube, "Device landing zone calcification, assessed by MSCT, as a predictive factor for pacemaker implantation after TAVI," *Catheter. Cardiovasc. Interv.*, vol. 76, no. 3, pp. 431–439, Sep. 2010.
- [3] X. Chaufour, G. White, B. Hamblly, W. Yu, J. May, J. Harris, and M. Stephen, "Evaluation of the risks of using an oversized balloon catheter in the human infrarenal abdominal aorta," *Eur. J. Vasc. Endovasc. Surg.*, vol. 16, no. 2, pp. 142–147, Aug. 1998.
- [4] E. Grube, J. C. Laborde, B. Zickmann, U. Gerckens, T. Felderhoff, B. Sauren, A. Bootsma, L. Buellesfeld, and S. Iversen, "First report on a human percutaneous transluminal implantation of a self-expanding valve prosthesis for interventional treatment of aortic valve stenosis," *Catheter. Cardiovasc. Interv.*, vol. 66, no. 4, pp. 465–469, Dec. 2005.
- [5] M. B. Leon, C. R. Smith, M. Mack, D. C. Miller, J. W. Moses, L. G. Svensson, E. M. Tuzcu, J. G. Webb, G. P. Fontana, R. R. Makkar, D. L. Brown, P. C. Block, R. A. Guyton, A. D. Richard, J. E. Bavaria, H. C. Herrmann, P. S. Douglas, J. L. Petersen, J. J. Akin, W. N. Anderson, D. Wang, and S. Pocock, "Transcatheter aortic-valve implantation for aortic stenosis in patients who cannot undergo surgery," *Engl. J. Med.*, vol. 363, no. 17, pp. 1597–1607, Oct. 2010.
- [6] N. Buzzatti, F. Maisano, A. Latib, M. Cioni, M. Taramasso, M. Mussardo, A. Colombo, and O. Alfieri, "Computed tomography-based evaluation of aortic annulus, prosthesis size and impact on early residual aortic regurgitation after transcatheter aortic valve implantation," *Eur. J. Cardio-Thoracic Surg.*, vol. 43, no. 1, pp. 43–51, Jan. 2013.
- [7] T. Schroeter, A. Linke, M. Haensig, D. R. Merk, M. A. Borger, F. W. Mohr, and G. Schuler, "Predictors of permanent pacemaker implantation after medtronic corevalve bioprosthetic implantation," *Europace*, vol. 14, no. 12, pp. 1759–1763, Dec. 2012.
- [8] M. Padala, E. L. Sarin, P. Willis, V. Babaliaros, P. Block, R. A. Guyton, and V. H. Thourani, "An engineering review of transcatheter aortic valve technologies," *Cardiovasc. Eng. Technol.*, vol. 1, no. 1, pp. 77–87, Mar. 2010.
- [9] Q. Wang, E. Sirois, and W. Sun, "Patient-specific modeling of biomechanical interaction in transcatheter aortic valve deployment," *J. Biomechan.*, vol. 45, no. 11, pp. 1965–1971, Jul. 2012.
- [10] J. Mummert, E. Sirois, and W. Sun, "Quantification of biomechanical interaction of transcatheter aortic valve stent deployed in porcine and ovine hearts," *Ann. Biomed. Eng.*, vol. 41, no. 3, pp. 577–586, Mar. 2013.
- [11] F. Auricchio, M. Conti, S. Morganti, and A. Reali, "Simulation of transcatheter aortic valve implantation: A patient-specific finite-element approach," *Comput. Methods Biomechan. Biomed. Eng.*, Feb. 13, 2013. [Epub ahead of print].
- [12] H. Zahedmanesh, H. van Oosterwyck, and C. Lally, "A multi-scale mechanobiological model of in-stent restenosis: Deciphering the role of matrix metalloproteinase and extracellular matrix changes," *Comput. Methods Biomechan. Biomed. Eng.*, Sep. 12, 2012. [Epub ahead of print].
- [13] D. Roy, C. Kauffmann, S. Delorme, S. Lerouge, G. Cloutier, and G. Soulez, "A literature review of the numerical analysis of abdominal aortic aneurysms treated with endovascular stent grafts," *Comput. Mathemat. Methods Med.*: 820389. Epub 2012 Sep. 6.
- [14] S. Morlacchi, C. Chiastri, D. Gastaldi, G. Pennati, G. Dubini, and F. Migliavacca, "Sequential structural and fluid dynamic numerical simulations of a stented bifurcated coronary artery," *J. Biomechan. Eng.*, vol. 133, no. 12, 121010, 11 pp., Dec. 29, 2011.
- [15] S. Schievano, C. Capelli, D. Cosentino, G. M. Bosi, and A. M. Taylor, "Finite-element analysis to study percutaneous heart valves," in *Proc. Finite Element Anal. Biomed. Appl. Ind. Devel.*, New York, NY, USA: InTech, 2011.
- [16] S. Tzamtzis, J. Viquerat, J. Yap, M. Mullen, and G. Burriesci, "Numerical analysis of the radial force produced by the medtronic-corevalve and Edwards-Sapien after transcatheter aortic valve implantation (TAVI)," *Med. Eng. Phys.*, vol. 35, no. 1, pp. 125–130, Jan. 2013.
- [17] G. J. Hall and E. P. Kasper, "Comparison of element technologies for modeling stent expansion," *J. Biomechan. Eng.*, vol. 128, no. 5, pp. 751–756, Oct. 2006.
- [18] A. Ganguly, J. Simons, A. Schneider, B. Keck, N. R. Bennett, R. J. Herfkens, S. M. Coogan, and R. Fahrig, "In-vivo imaging of femoral artery nitinol stents for deformation analysis," *J. Vasc. Intervent. Radiol.*, vol. 22, no. 2, pp. 244–249, Feb. 2011.
- [19] M. Gessat, L. Altwein, T. Frauenfelder, A. Plass, and V. Falk, "Cubic hermite Bezier spline based reconstruction of implanted aortic valve stents from CT images," in *Proc. IEEE Eng. Med. Biol. Soc. Conf.*, Aug.–Sep. 2011, pp. 2667–2670.
- [20] R. Hopf, M. Gessat, V. Falk, and E. Mazza, "Stent induced loading of the aortic valve complex," presented at the MICCAI Stent-Workshop, Nizza, France, 2012.
- [21] L. Petrini, F. Migliavacca, P. Massarotti, S. Schievano, G. Dubini, and F. Auricchio, "Computational studies of shape memory alloy behavior in biomedical applications," *J. Biomechan. Eng.*, vol. 127, no. 4, pp. 716–725, Aug. 2005.



Michael Gessat received the Graduate degree in informatics from the University of Karlsruhe, Germany, and the Ph.D. degree from the Institute of Computer Science, Universität Leipzig, Germany, in 2005 and 2010, respectively.

Since 2009, he has been with the University Hospital Zurich, Switzerland and the Swiss Federal Institute of Technology (ETH) Zurich, Switzerland as a Senior Scientist. His research interest includes computer assisted cardiovascular surgery.



Simon Harald Sündermann received the Graduate degree in medicine and the M.D. degree from Universität Leipzig, Germany, in 2007 and 2012.

From 2008 to 2009, he was a Trainee for Cardiac Surgery at the Heart Center Leipzig, Germany. Since 2009, he has been a trainee at the University-Hospital Zurich (USZ), Switzerland. He is part of an interdisciplinary project group between USZ and the Swiss Federal Institute of Technology (ETH) Zurich, Switzerland, focussing on computer assisted cardiac surgery.



membranes.

Raoul Hopf received the M.Sc. degree in mechanical engineering, focussing on continuum mechanics and dynamics of multibody and non-smooth systems, from the Swiss Federal Institute of Technology (ETH) Zurich, Switzerland, in 2011, and is currently working toward the Ph.D. degree at the Center of Mechanics, ETH Zurich.

He is working on a joint project with the University Hospital Zurich, Switzerland, on modeling stent mechanics. His research interest includes the mechanical behavior of biological



Sven Hirsch received the Graduate degree in physics from the Ruprecht-Karls University, Heidelberg, Germany and the Ph.D. degree in laser physics from the University of Düsseldorf, Germany, in 1998 and 2007, respectively.

He is currently with the Biomedical Simulation Group, the Computer Vision Laboratory, Swiss Federal Institute of Technology (ETH) Zurich, Switzerland. His research interests include physiological modeling of the cardiovascular system as well as image-based simulation of tumor growth.



Thesis at the Computer Vision Laboratory, Swiss Federal Institute of Technology (ETH) Zurich, Switzerland.

Thomas Pollok received the B.Sc. degree in computer science from the University of Applied Sciences, Karlsruhe, Germany in 2012 and is currently working toward the Master's degree in computer science at the Berlin Institute of Technology, Berlin, Germany.

During his studies, he intensively collaborated with the Fraunhofer IOSB in the field of image-based real-time systems.

Mr. Pollok received a scholarship in 2011 by the State of Baden-Württemberg to support his Bachelor



Edoardo Mazza received the Dr. sc. techn. degree from the Swiss Federal Institute of Technology (ETH) Zurich, Switzerland, in 1997.

He has been a Full Professor of Mechanics at the Institute of Mechanical Systems, ETH Zurich since January 1, 2010. After the Ph.D. degree, he has been working in industry for four years. In 2001, he was an Assistant Professor, in 2006 an Associate Professor of Mechanics at ETH Zurich. Since 2006, he has been leading the laboratory "Mechanics for modeling and simulation", the Swiss Federal Laboratories for Material Science and Technology (EMPA), Dubendorf, Switzerland.



Christoph Russ (S'13) received the Graduate degree in computational visualistics from the Otto-von-Guericke University, Magdeburg, Germany, in 2010, and is working toward the Ph.D. degree in the field of biomedical simulation for computer-assisted surgery planning from the Swiss Federal Institute of Technology (ETH) Zurich, Switzerland, in a joint project with the University Hospital Zurich, Switzerland.

He worked with the Australian E-Health Research Centre between 2007 and 2009, before he joined Siemens Corporate Research, Princeton, NJ, USA.



Gábor Székely (M'94) received the Graduate degree in chemical engineering, the Graduate degree in applied mathematics, and the Ph.D. degree in analytical chemistry from the Technical University of Budapest, Budapest, Hungary, in 1974, 1981, and 1985, respectively.

He is currently a Full Professor of Medical Image Analysis and Visualization at the Computer Vision Laboratory, Swiss Federal Institute of Technology (ETH) Zurich, Switzerland, where he is involved in the development of image analysis, visualization, and

simulation methods for computer support of medical diagnosis, therapy, training, and education.



He collaborated with the ETH Zurich in various projects.

Thomas Frauenfelder received the M.D. degree from the University of Zurich, Zurich, Switzerland, in 1999.

From 2002 to 2003, he was Research Fellow in the field of computational fluid dynamics. In 2009, he became an Associate Professor of the University of Zurich. Since 2011, he has been the vice director of the Institute of Diagnostic and Interventional Radiology at the University Hospital Zurich. His research interests include postprocessing in the field of radiological imaging, especially cardiovascular imaging.



He collaborated with the ETH Zurich in various projects.

Volkmar Falk received the Graduation degree in medicine and the M.D. degree from the University of Bonn in 1992 and 1993, respectively, and the Ph.D. degree from Universität Leipzig, Germany, in 1999.

In 2006, he was the Codirector of the Heart Center Leipzig, Germany and Member of the Medical Faculty of Universität Leipzig, Germany. He serves the European Association of Cardiothoracic Surgery as the Chairman of the Techno College. In 2009, he was the Director of the Division of Cardiovascular Surgery at University Hospital Zurich, Switzerland and a Full Professor for Cardiac Surgery at the University of Zurich, Switzerland.

2.6 Fusion von echokardiographischen und fluoroskopischen Bildern während MitraClip-Interventionen

Sündermann SH, Biaggi P, Grünenfelder J, Gessat M, Felix C, Bettex D, Falk V, Corti R. Safety and Feasibility of Novel Technology Fusing Echocardiography and Fluoroscopy Images during MitraClip Interventions. EuroIntervention 2014; 9(10): 1210-1216³⁸

[doi: 10.4244/EIJV9I10A203](https://doi.org/10.4244/EIJV9I10A203)

Nicht nur zur präoperativen Planung, sondern auch im Operationssaal ist für kathetergestützte Eingriffe eine hochwertige Bildgebung notwendig. Das MitraClip-Verfahren stellt eine komplexe Katheterintervention dar. Ein Clip wird am Rand des vorderen und hinteren Mitralklappensegels fixiert, durch welchen beide Segel aneinandergeheftet werden und ein sogenanntes *double orifice* entsteht. Dadurch kann eine Mitralklappeninsuffizienz reduziert bzw. eliminiert werden. Das Verfahren wird vor allem bei Hochrisikopatienten angewendet, um den Einsatz der Herz-Lungen-Maschine zu vermeiden. Die entscheidenden bildgebenden Verfahren sind die Fluoroskopie und die Echokardiographie. Beide bildgebenden Verfahren müssen vom Operateur mental fusioniert werden. Eine Software, der EchoNavigator der Firma Philips, ermöglicht die Fusion beider bildgebender Verfahren. Über eine Registrierung der Form der transösophagealen Echokardiographiesonde wird ein einheitliches Koordinatensystem geschaffen und das Echokardiographiebild in das Fluoroskopiebild fusioniert. In dieser Studie wurde die sichere Anwendbarkeit dieser Software während MitraClip-Eingriffen bei 21 Patienten untersucht. Es konnte gezeigt werden, dass bei der zweiten Hälfte der Patienten, bei welchen die EchoNavigator-Software verwendet wurde, ein Trend hin zur Reduktion der Strahlendosis und der Zeit für die Intervention bestand. Dies wurde im Sinne eines Durchlaufens einer *learning curve* interpretiert. Außerdem zeigte sich eine Reduktion der Zeit für die Intervention bei Patienten, bei denen mehr als zwei Clips implantiert wurden, also bei komplexeren Interventionen.

Zusammenfassend konnte gezeigt werden, dass die EchoNavigator-Software sicher angewendet werden und tendenziell eine Reduktion der Strahlendosis und der Zeit für die Intervention erreicht werden konnte.

Safety and feasibility of novel technology fusing echocardiography and fluoroscopy images during MitraClip interventions

Simon H. Sündermann^{1*}, MD; Patric Biaggi², MD; Jürg Grünenfelder¹, MD, PhD; Michael Gessat^{1,4}, PhD; Christian Felix³, MD; Dominique Bettex³, MD, PhD; Volkmar Falk¹, MD, PhD; Roberto Corti², MD, PhD

1. Division of Cardiovascular Surgery, University Hospital Zurich, Zurich, Switzerland; 2. Division of Cardiology, University Hospital Zurich, Zurich, Switzerland; 3. Computer Vision Laboratory, Swiss Federal Institute (ETH) Zurich, Zurich, Switzerland; 4. Institute of Anaesthesiology, University Hospital Zurich, Zurich, Switzerland

S. H. Sündermann and P. Biaggi contributed equally to this manuscript.

This paper also includes accompanying supplementary data published online at: http://www.pcronline.com/eurointervention/69th_issue/203

KEYWORDS

- EchoNavigator
- MitraClip
- mitral valve disease
- percutaneous mitral valve repair
- real-time fusion
- structural heart disease interventions

Abstract

Aims: The EchoNavigator (EN) software (Philips Healthcare, Best, The Netherlands) enables real-time fusion of echocardiography and fluoroscopy by co-registration of the echocardiography probe on the x-ray image. We aimed to evaluate the feasibility and safety of this novel software during MitraClip procedures.

Methods and results: Twenty-one patients were treated with the support of EchoNavigator software (EN+ patients). The primary (safety) endpoint was the total radiation dose. Secondary endpoints were fluoroscopy and total procedure time. The measurements were compared to those of 21 patients treated immediately before the installation of EchoNavigator (EN- patients). More MitraClips (45 vs. 36) were implanted in the EN+ group, mirroring more complex interventions in this group. In EN+ patients, radiation dose (Gy/cm²) was similar compared to EN- patients (146.5 ± 123.6 vs. 146.8 ± 134.1 , p=0.9). Total procedure time (minutes) was similar in the EN+ group compared to EN- patients (136.2 ± 50.2 vs. 125.7 ± 51.2 , p=0.5). The main benefit of the EchoNavigator is the automated real-time fusion of echocardiography and fluoroscopy, leading to easier catheter manipulation.

Conclusions: The use of EchoNavigator software was feasible and safe in all study patients. Further studies are necessary to confirm the benefits of using this software.

*Corresponding author: University Hospital Zurich, Division of Cardiovascular Surgery, Raemistrasse 100, CH-8091 Zurich, Switzerland. E-mail: simon.suendermann@usz.ch

Abbreviations

2-D	two-dimensional
3-D	three-dimensional
A2	middle part of the anterior mitral valve leaflet
DRR	digitally reconstructed radiograph
EN	EchoNavigator
EN-	group in whom EchoNavigator software was not used
EN+	group in whom EchoNavigator software was used
Gy	gray
MC	MitraClip
MR	mitral regurgitation
OR	operating theatre
P2	middle part of the posterior mitral valve leaflet
TEE	transoesophageal echocardiography

Introduction

MitraClip® (Abbott Vascular, Abbott Park, IL, USA) implantation is currently the only accepted alternative interventional treatment option for patients with mitral valve regurgitation (MR) who are at high risk for surgery¹. The procedure is an adaptation of the Alfieri stitch, but is performed with a catheter technique via femoral vein access and is a beating heart procedure. Alfieri and colleagues described a significant reduction of MR by producing a “double orifice” mitral valve with a stitch adapting the margins of A2 and P2 in severe degenerative disease². The MitraClip (MC) procedure was initially introduced for the treatment of degenerative mitral valve disease but was also rapidly adopted in functional disease. The procedure significantly reduces MR, immediately improves haemodynamic function³ and has demonstrated good short and midterm clinical results⁴⁻⁶. The crucial steps for a successful procedure are a precise transseptal puncture⁷ and the placement of the MitraClip at the aimed lesion site. Fluoroscopy and real-time 2-D and 3-D transoesophageal echocardiography (TEE) are the imaging modalities of choice during the procedure⁸. The images of both techniques are presented to the operator in parallel, and the operator needs to fuse the displayed pictures mentally in order to succeed with the procedure. To support the operator with this demanding task and potentially to reduce the procedure length and the radiation dose necessary during such procedures, Philips Healthcare (Best, The Netherlands) introduced EchoNavigator, a software tool that provides real-time image co-registration and fusion of the TEE and fluoroscopy images during the procedure.

The goal of this study was to evaluate the feasibility and safety of the software during MitraClip interventions.

Methods

We compared the procedural characteristics of the first 21 patients who underwent a MitraClip procedure assisted by the EchoNavigator software to the procedural data of the 21 patients treated immediately before the introduction of the software. The procedures in all 42 patients were performed in a standard way for MitraClip implantation in a hybrid operating theatre (hybrid OR) as described earlier³. The primary safety endpoint was the radiation dose during

MitraClip intervention supported by EchoNavigator. Secondary endpoints were fluoroscopy time, length of the overall procedural time and duration of the different procedural steps. The procedural steps were quantified as the time from femoral puncture to placement of the first, second, third and fourth clip. All patients gave written informed consent to be included in this prospective, non-randomised arm of the trial, and the study protocol was approved by the local institutional review board.

ECHONAVIGATOR

For this study, a prototype of the software was used. The EchoNavigator system synchronises and co-registers the echocardiography and fluoroscopy images in real time in hybrid ORs equipped with Philips hardware. Changes in angulation, rotation or position of the TEE probe are immediately registered and updated on fluoroscopy images. In addition, the software provides concordant views of TEE and fluoroscopy by presenting echocardiography images in the same anatomic alignment as the C-arm. Furthermore, if the C-arm is moved, echocardiography image information is updated with the same orientation (**Moving image 1**).

The key feature of EchoNavigator is the automated localisation of the echo probe in the fluoroscopy, providing real-time co-registration of the two image modalities. This happens in two steps, a detection phase and a tracking phase. The goal of the detection phase is to localise the probe in an x-ray image without using the results from previous images. A detection algorithm scans the entire x-ray frame for the possible presence of a TEE probe. This detection is based upon a technique using the edge models of the object of interest. The edge model for the EchoNavigator is computed from the boundaries of the digitally reconstructed radiograph (DRR) from a tomographic probe model of a TEE probe at a defined position (**Moving image 1**). The second phase is the tracking phase. In this phase the position of the probe is continuously updated, during both resting and rotating C-arm. Tracking describes the process of taking an estimate of the TEE probe pose as an input and refining it on the current x-ray image to produce an estimate of the current pose of the TEE probe.

The use of the EchoNavigator during MitraClip interventions is of particular interest during two procedural steps: puncture of the interatrial septum, and catheter steering for optimal clip placement. The optimal puncture site is defined by echocardiography, using the X-plane feature allowing simultaneous demonstration of two orthogonally orientated image planes. In agreement with the echocardiographer, the interventionalist marks this optimal puncture site using a tableside control pad by introducing a marker in the echocardiography image (**Figure 1A**). The marker is automatically updated on the fluoroscopy image (**Figure 1B**, **Figure 1C**, **Moving image 2**). Additionally the interventionalist can rotate and zoom an echocardiography image from the tableside independently from the echocardiographer (**Moving image 3**). By this means, the navigation of the transseptal puncture needle through the right atrium towards the optimal puncture site is facilitated and a targeted puncture enabled (**Figure 1C**). After successful septal puncture, the optimal clipping

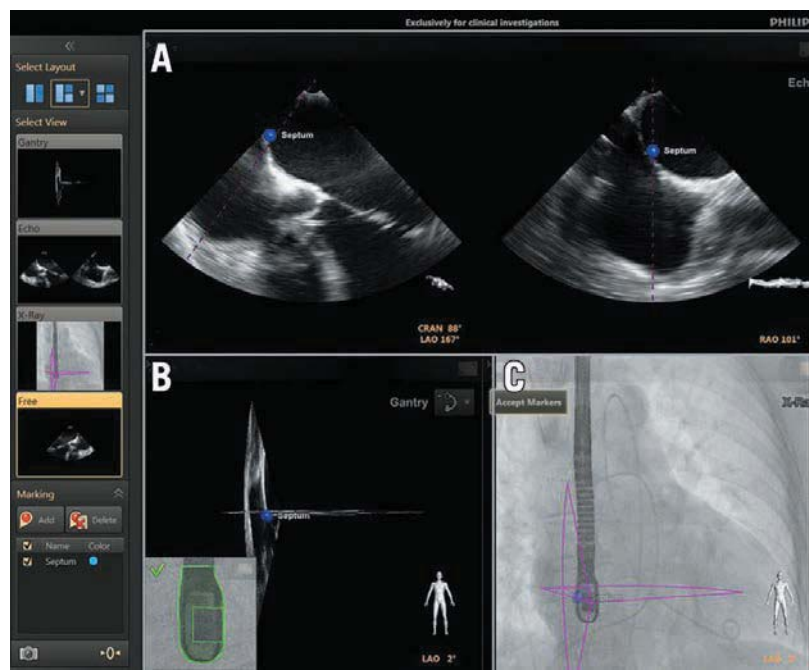


Figure 1. EchoNavigator view with: A) 2-D X-plane echocardiography image. The interatrial septum is marked with a blue dot. B) X-plane echo images with marker, oriented in the same way as the C-arm. The small inlay picture indicates that the TEE probe is registered correctly. C) Outlines of X-plane images together with the blue marker are fused with the fluoroscopy image.

site is defined by the interventionalist in a similar fashion by marking the lesion at the level of the mitral valve in the echocardiography images and using the fluoroscopy images to help catheter manipulation within the left atrium (**Figure 2A** and **Figure 2C**).

STATISTICAL ANALYSES

Continuous variables are expressed as mean plus standard deviation. Categorical data are given in proportions. The unpaired t-test was used for comparison of the two groups for continuous variables, and Fisher's exact test was used for binary variables. A p-value of less than 0.05 was considered statistically significant. Statistical analyses were performed using SPSS software (IBM SPSS Statistics version 20.0; SPSS Inc., Chicago, IL, USA).

Results

BASELINE CHARACTERISTICS

The baseline characteristics of the patient population are shown in **Table 1**. The mean age of the patients was 77 ± 9 years, and 38% of patients were female. At the time of intervention, 95% of patients had severe MR. In 52% of the cases, degenerative MR was the reason for the intervention. Five patients in the EN+ and two patients in the EN- group needed more than two clips. Since the majority of patients treated in Europe received only one or two clips⁹, additional analyses are given for these patients.

PRIMARY ENDPOINTS

The procedural data are shown in **Table 2**. Total radiation dose and fluoroscopy time did not differ significantly between the groups.

Table 1. Baseline characteristics.

N	Total 42	Total 21	with EchoNavigator	without EchoNavigator	p
		21	21	21	
Age (years)		77.2 ± 9.4	77.5 ± 8.7	77 ± 10	0.8
Female sex, n (%)	16 (38)	8 (38)	8 (38)	8 (38)	1
Degenerative MR, n (%)	22 (52)	11 (52)	11 (52)	11 (52)	1
Functional MR, n (%)	20 (48)	10 (48)	10 (48)	10 (48)	1
Grade of insufficiency	Moderate, n (%) Severe, n (%)	2 (5) 40 (95)	0 (0) 21 (100)	2 (10) 19 (90)	— 1

N: number of patients; MR: mitral valve regurgitation

In patients with one or two clips, a trend towards a reduction of radiation dose (~15%) and fluoroscopy time (~5%) was observed (**Figure 3**). Six out of the seven patients in whom more than two clips were implanted had advanced mitral valve prolapse, usually with multiple segments involved. This condition is therefore less suitable for MC treatment and thus these patients needed more complex procedures.

SECONDARY ENDPOINTS

While more clips were needed in the EchoNavigator group (45 vs. 36, $p=0.3$), the length of the interventions was similar for both groups. The higher the number of clips used, the shorter the time duration per clip when the EchoNavigator was used compared to the control group (**Figure 4**). When two clips were used the time until the placement of the second clip could be decreased by six minutes (7%) and, when

Table 2. Procedural data.

	Total (n=42)	with EchoNavigator (n=21)	without EchoNavigator (n=21)	p
Number of clips implanted, n (%)	81 (100%)	45 (56%)	36 (44%)	0.3
Patients with 1/2/3/4 clips (n)	12/23/5/2	4/12/3/2	8/11/2/0	—
Length (minutes) all patients	131±50.3	136.2±50.2	125.7±51.2	0.5
Length (minutes) patients ≤2 clips	112.7±26.8	113.9±29.9	111.8±24.9	0.8
Fluoroscopy time (minutes) all patients	31.4±15.8	32.3±16.8	30.6±15.3	0.8
Fluoroscopy time (minutes) patients ≤2 clips	25.1±7.1	23.9±8.1	26.1±6.4	0.4
Radiation dose (Gy/cm ²) all patients	146.7±127.4	146.5±123.6	146.8±134.1	1.0
Radiation dose (Gy/cm ²) patients ≤2 clips	112.8±73	102.1±65	119.8±78.9	0.5
Time to first clip (minutes)	53.6±15.8	52.4±17.6 (n=21)	53.7±14.0 (n=21)	0.8
Time to second clip (minutes)	85.7±27.7	83.2±27.4 (n=17)	88.9±29.0 (n=13)	0.6
Time to third clip (minutes)	152.86±47.5	134.2±23.2 (n=5)	199.5±72.8 (n=2)	0.4

The numbers in brackets indicate the number of patients who had implantation of one, two or three clips in the respective group. Gy: gray

three clips were used, a decrease in the length of the procedure of more than one hour (33%) was seen. A fourth clip was placed in only two patients with very advanced mitral valve prolapse in the EchoNavigator group, yet the time to placement of the fourth clip was shorter than the time for placement of three clips in the control group.

INFLUENCE OF LEARNING CURVE

A trend towards reduction of radiation dose, procedure length and fluoroscopy time was observed during the second half of patients in whom the EchoNavigator software was used, in those patients where one or two clips were used (**Figure 5**).

Discussion

Fluoroscopy and echocardiography are the imaging modalities of choice during MitraClip implantation. Echocardiography provides excellent imaging of the anatomical structures of the mitral valve and especially three-dimensional echocardiography is crucial for the orientation and precise guide steering during the procedure. However, image quality can be suboptimal due to shadowing by catheter overlays, and guidewires may at times not even be detected by echocardiography^{9,10}. Fluoroscopy on the other hand gives a two-dimensional view of the field of interest. In contrast to echocardiography it clearly visualises the catheter and its position and is therefore a necessary part of the procedure. Additionally, the clip itself is better visualised by fluoroscopy. The mental fusion of both image modalities is necessary but also challenging for the operator. Good communication between the operator and the echocardiographer is of great importance to facilitate this process. However, in a standard hybrid OR, the set-up can be unsupportive for easy and effective communication. The EchoNavigator software fuses echocardiography and fluoroscopy and holds the potential to facilitate this process.

This study aimed to evaluate the safety and feasibility of the EchoNavigator software by using a prototype of the programme during MitraClip implantation. As shown by our data, the software

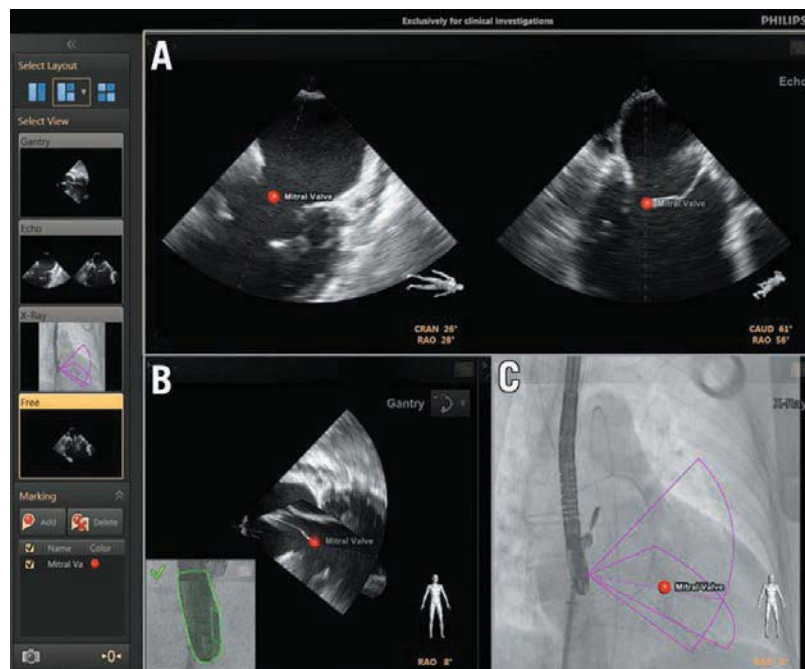


Figure 2. EchoNavigator view with: A) 2-D X-plane echocardiography image. The optimal mitral valve clipping site is highlighted with a red marker. B) X-plane echo images with marker, orientated in the same way as the C-arm. The small inlay picture indicates that the TEE probe is registered correctly. C) Outlines of X-plane images together with the red marker are fused with the fluoroscopy image.

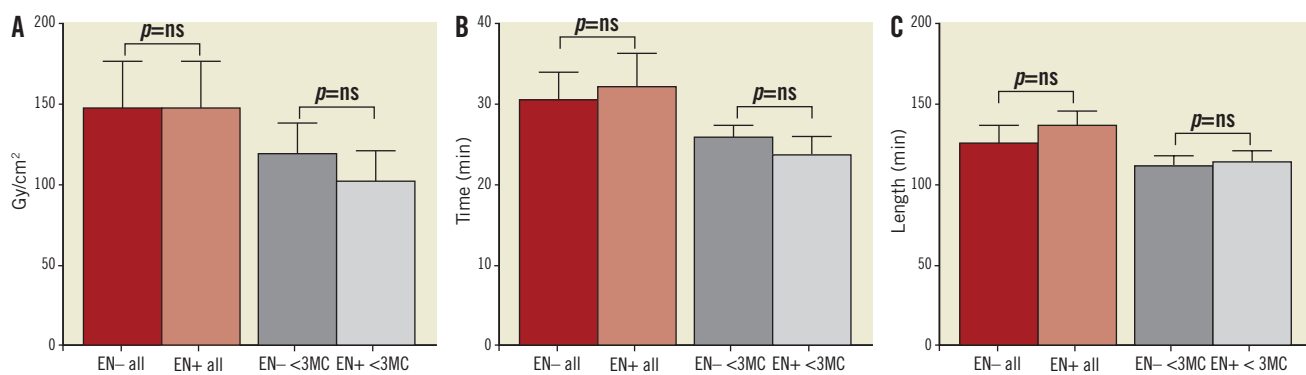


Figure 3. Primary endpoints. (A) Radiation dose in all patients (EN- all and EN+ all) and in those patients with one or two MCs (EN- \leq 2 MCs and EN+ \leq 2 MCs). (B) Fluoroscopy time in all patients (EN- all and EN+ all) and in those patients with one or two MCs (EN- \leq 2 MCs and EN+ \leq 2 MCs). (C) Procedure length in all patients (EN- all and EN+ all) and in those patients with one or two MCs (EN- \leq 2 MCs and EN+ \leq 2 MCs). EN-: control group before installation of EchoNavigator; EN+: with use of EchoNavigator; all: total patient population; \leq 2 MC: group of patients with only one or two MCs implanted; Time: fluoroscopy time; Length: procedure length from puncture to closure

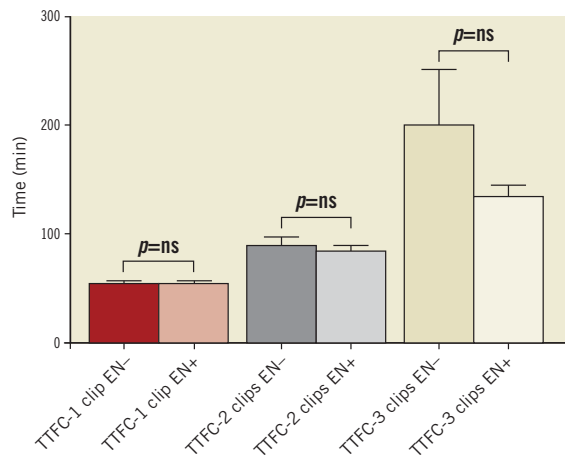


Figure 4. Milestones of the procedure. EN-: control group before installation of EchoNavigator; EN+: with use of EchoNavigator; TTFc: time needed until final clip was placed; 1 clip, 2 clips, 3 clips: number of clips used in the procedure; min: minutes

was successfully used in all of the first 21 cases planned and was supportive for the procedure. Despite the necessity of using fluoroscopy to co-register both image technologies, the primary safety endpoint (radiation dose), was similar in both groups. The differences in length of the procedure only showed a trend and did not reach statistical significance. The procedure time in the EN+ group was not remarkably higher compared to the EN- group, despite the fact that these data reflect our learning period using prototype software that was updated several times during the study until the currently used stable version was available. In addition, the patients in the EchoNavigator group needed more clips. Given these considerations, the trend to reduction of both radiation dose and intervention time is even more remarkable.

The mean length of the procedure was comparable in both groups, and the times are similar to other published series^{9,11}. Interestingly, the time until a final clip was placed was inversely correlated to the number of clips used. Despite the fact that more clips needed to be implanted in the EchoNavigator group

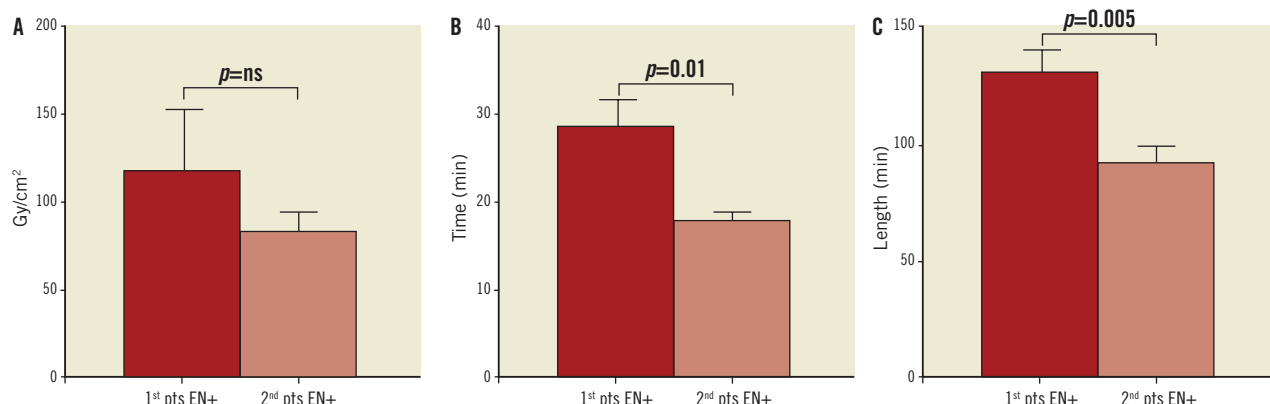


Figure 5. Results representing the learning curve in patients with one or two clips implanted. A) Radiation dose. B) Fluoroscopy time. C) Procedure length. EN+: with use of EchoNavigator; Time: fluoroscopy time; Length: procedure length from puncture to closure; 1st pts: first half of patients ($n=10$); 2nd pts: second half of patients ($n=10$).

(signalling more complex interventions), the total time needed for the procedure was not relevantly higher compared to the control group. The duration until a third clip was placed was much shorter in the EchoNavigator group compared to the control group. Multiple clips are needed mostly in severe degenerative mitral valve disease, which represent very challenging interventions. This shows that in complex procedures where more clips are used the imaging modality becomes even more important and the use of supporting software is beneficial. With increasing experience the software will not only facilitate difficult interventions in structural heart disease by providing a variety of new image projections to the operator, but also has the potential to reduce procedural time and radiation exposure. The goals of the development of further versions of the software are the implementation of catheter visualisation and the overlay of echocardiographic images for tissue visualisation.

Limitations

This study contains the usual limitations of all non-randomised studies. Sheer luck led to very similar patient groups, and thus comparison appears meaningful despite the small number of patients in each group. Furthermore, this study was designed to test the feasibility and safety of this new software and not to compare head to head the superiority of the software.

Caution is necessary when interpreting our data. The challenge in evaluating medical software during cardiac interventions lies in the complexity of the interventions. We determined factors that are relatively stable in order to measure the performance of the software. However, a lot of variables such as the quality of echocardiography images or anatomical alterations influence the length of an intervention and the need for additional fluoroscopy time. Therefore, we cannot exclude that non-measured factors may have influenced the results.

The EchoNavigator software is only available in combination with specific Philips hardware. However, many interventionalists use competitor hardware and software. Thus, unfortunately, our results only address those colleagues who use such a set-up.

Conclusion

In this non-randomised study, the use of the EchoNavigator was feasible and safe during MitraClip interventions, and tended to reduce the radiation dose and procedure time. A prospective, randomised trial with a larger sample size is needed to demonstrate efficacy of the software.

Funding

The Division of Cardiovascular Surgery at the University Hospital Zurich holds a research grant from Philips Healthcare (Best, The Netherlands).

Conflict of interest statement

R. Corti and P. Biaggi have received speakers' honoraria from Abbott Vascular, Brussels, Belgium, and Philips Healthcare, Best, The Netherlands. The other authors have no conflicts of interest to declare.

References

- Vahanian A, Alfieri O, Andreotti F, Antunes MJ, Barón-Esquivas G, Baumgartner H, Borger MA, Carrel TP, De Bonis M, Evangelista A, Falk V, Lung B, Lancellotti P, Pierard L, Price S, Schäfers HJ, Schuler G, Stepinska J, Swedberg K, Takkenberg J, Von Oppell UO, Windecker S, Zamorano JL, Zembala M; ESC Committee for Practice Guidelines (CPG); Joint Task Force on the Management of Valvular Heart Disease of the European Society of Cardiology (ESC); European Association for Cardio-Thoracic Surgery (EACTS). Guidelines on the management of valvular heart disease (version 2012): the Joint Task Force on the Management of Valvular Heart Disease of the European Society of Cardiology (ESC) and the European Association for Cardio-Thoracic Surgery (EACTS). *Eur J Cardiothorac Surg.* 2012;42:S1-44.
- Alfieri O, Maisano F, De Bonis M, Stefano PL, Torracca L, Oppizzi M, La Canna G. The double-orifice technique in mitral valve repair: a simple solution for complex problems. *J Thorac Cardiovasc Surg.* 2001;122:674-81.
- Gaemperli O, Moccetti M, Surder D, Biaggi P, Hurlmann D, Kretschmar O, Buehler I, Bettex D, Felix C, Lüscher TF, Falk V, Grünfelder J, Corti R. Acute haemodynamic changes after percutaneous mitral valve repair: relation to mid-term outcomes. *Heart.* 2012;98:126-32.
- Whitlow PL, Feldman T, Pedersen WR, Lim DS, Kipperman R, Smalling R, Bajwa T, Herrmann HC, Lasala J, Maddux JT, Tuzcu M, Kapadia S, Trento A, Siegel RJ, Foster E, Glower D, Mauri L, Kar S; EVEREST II Investigators. Acute and 12-month results with catheter-based mitral valve leaflet repair: the EVEREST II (Endovascular Valve Edge-to-Edge Repair) High Risk Study. *J Am Coll Cardiol.* 2012;59:130-9.
- Franzen O, van der Heyden J, Baldus S, Schlüter M, Schillinger W, Butter C, Hoffmann R, Corti R, Pedrazzini G, Swaans MJ, Neuss M, Rudolph V, Sürder D, Grünfelder J, Eulenburg C, Reichenspurner H, Meinertz T, Auricchio A. MitraClip® therapy in patients with end-stage systolic heart failure. *Eur J Heart Fail.* 2011;13:569-76.
- Sürder D, Pedrazzini G, Gaemperli O, Biaggi P, Felix C, Rufibach K, der Maur CA, Jeger R, Buser P, Kaufmann BA, Moccetti M, Hürliemann D, Bühlert I, Bettex D, Scherman J, Pasotti E, Faletra FF, Zuber M, Moccetti T, Lüscher TF, Erne P, Grünfelder J, Corti R. Predictors for efficacy of percutaneous mitral valve repair using the MitraClip system: the results of the MitraSwiss registry. *Heart.* 2013;99:1034-40.
- Maisano F, La Canna G, Latib A, Godino C, Denti P, Buzzatti N, Taramasso M, Cioni M, Giacomini A, Colombo A, Alfieri O. Transseptal access for MitraClip® procedures using surgical diathermy under echocardiographic guidance. *EuroIntervention.* 2012;8:579-86.
- Altio E, Becker M, Hamada S, Reith S, Marx N, Hoffmann R. Optimized guidance of percutaneous edge-to edge repair of the mitral valve using real-time 3-D transesophageal echocardiography. *Clin Res Cardiol.* 2011;100:675-81.
- Maisano F, Franzen O, Baldus S, Schäfer U, Hausleiter J, Butter C, Ussia GP, Sievert H, Richardt G, Widder JD, Moccetti T,

Schillinger W. Percutaneous mitral valve interventions in the real world: early and one year results from the ACCESS-EU, a prospective, multi-center, non-randomized post-approval study of the MitraClip® therapy in Europe. *J Am Coll Cardiol.* 2013;62:1052-61.

10. Silvestry FE, Rodriguez LL, Herrmann HC, Rohatgi S, Weiss SJ, Stewart WJ, Homma S, Goyal N, Pulerwitz T, Zunamon A, Hamilton A, Merlino J, Martin R, Krabill K, Block PC, Whitlow P, Tuzcu EM, Kapadia S, Gray WA, Reisman M, Wasserman H, Schwartz A, Foster E, Feldman T, Wiegers SE. Echocardiographic guidance and assessment of percutaneous repair for mitral regurgitation with the Evalve MitraClip: lessons learned from EVEREST I. *J Am Soc Echocardiogr.* 2007;20:1131-40.

11. Feldman T, Kar S, Rinaldi M, Fail P, Hermiller J, Smalling R, Whitlow PL, Gray W, Low R, Herrmann HC, Lim S, Foster E, Glower D; EVEREST Investigators. Percutaneous mitral repair with the MitraClip system: safety and midterm durability in the initial EVEREST (Endovascular Valve Edge-to-Edge REpair Study) cohort. *J Am Coll Cardiol.* 2009;54:686-94.

Online data supplement

Moving image 1. Registration of the TEE probe. The clip shows the EchoNavigator screen as seen in the OR. Upper screen shows a TEE view of the septum. Left lower screen shows the TEE screen of the EchoNavigator software. When the automated registration of

the TEE probe is successful, the small inlay image of the TEE probe head turns from red to green. The right lower picture shows the angio-screen of the EchoNavigator software with the outline of the ultrasound window.

Moving image 2. Tableside placement of a marker at the atrial septal wall. The clip shows the EchoNavigator screen as seen in the OR. Upper screen shows the regular TEE view. Lower left screen shows the TEE screen of the EchoNavigator software with registered TEE probe. The right lower picture shows the angio-screen of the EchoNavigator software with the outline of the ultrasound window. Yellow markers are placed from the tableside by the interventionist at the position of the septum in the TEE screen. The markers are automatically fused to the other screens. The marker is labelled afterwards by choosing a description from a list. At the end of the moving image, the X-plane view and the 3-D view of the software are demonstrated.

Moving image 3. Tableside control and rotation of 3-D TEE image. The clip shows the EchoNavigator screen as seen in the OR. Right upper screen shows a regular 3-D TEE. The left upper and lower screens show the 3-D TEE screen of the EchoNavigator software. The right lower screen shows the angio-screen of the EchoNavigator software with the outline of the 3-D ultrasound window. The interventionist rotates, zooms in and out and places a marker from the tableside in the left lower view.

2.7 Zweidimensionale und dreidimensionale transösophageale Echokardiographie im Großtiermodell

Sündermann SH, Cesarovic N, Falk V, Bettex D

Two- and Three-Dimensional Transoesophageal Echocardiography in Large Swine Used as Model for Transcatheter Heart Valve Therapies: Standard Planes and Values.
Interact Cardiovasc Thorac Surg 2016; 22(5): 580-586³⁹

[doi: 10.1093/icvts/ivv381](https://doi.org/10.1093/icvts/ivv381)

Voraussetzung für die Entwicklung von neuen kathetergestützten Verfahren zur Behandlung struktureller Herzerkrankungen ist die präklinische Testung im Großtiermodell. Das Schwein eignet sich durch die anatomische Ähnlichkeit des kardiovaskulären Systems hier besonders. Katheterinterventionen erweitern das Armamentarium der patientenspezifischen Behandlung beträchtlich, insbesondere für Hochrisikopatienten. Selbstverständlich sollten auch in der präklinischen Phase die Standardbildgebungsverfahren angewendet werden, die auch in der klinischen Phase zur Anwendung kommen. Die Echokardiographie spielt hier eine besondere Rolle. In der angefügten Publikation wurde für die TEE eine Standarduntersuchungsmethode inklusive Standardwerten für das Großtiermodell Schwein entwickelt. Bei 20 Schweinen, die in verschiedenen Versuchen zur präklinischen Untersuchung von Mitralklappenprothesen verwendet wurden, wurden vor dem Eingriff eine standardisierte TEE durchgeführt und die erhobenen Werte dokumentiert. Es konnte bei allen Tieren eine ausreichende Qualität der Bildgebung erzielt werden, so dass für alle Tiere alle im Protokoll vorgesehenen Werte erhoben werden konnten.

Zusammenfassend kann festgehalten werden, dass die TEE im Großtiermodell eine gut anwendbare Methode ist, um die präklinische Entwicklung kathetergestützter Therapieformen der strukturellen Herzerkrankung zu unterstützen und damit das Armamentarium patientenspezifischer Therapieformen weiter zu entwickeln.

Cite this article as: Sündermann SH, Cesarovic N, Falk V, Bettex D. Two- and three-dimensional transoesophageal echocardiography in large swine used as model for transcatheter heart valve therapies: standard planes and values. *Interact CardioVasc Thorac Surg* 2016;22:580–6.

Two- and three-dimensional transoesophageal echocardiography in large swine used as model for transcatheter heart valve therapies: standard planes and values

Simon H. Sündermann^{a,*}, Nikola Cesarovic^b, Volkmar Falk^a and Dominique Bettex^c

^a Department of Cardiothoracic and Vascular Surgery, Deutsches Herzzentrum Berlin, Berlin, Germany

^b Department of Surgical Research, University Hospital Zurich, University of Zurich, Zurich, Switzerland

^c Institute of Anesthesiology, University Hospital Zurich, University of Zurich, Zurich, Switzerland

* Corresponding author. Department of Cardiothoracic and Vascular Surgery, Deutsches Herzzentrum Berlin, Augustenburger Platz 1, 13353 Berlin, Germany.
Tel: +49-30-45932086; fax: +49-30-45932100; e-mail: suendermann@dhzb.de (S.H. Sündermann).

Received 14 July 2015; received in revised form 13 November 2015; accepted 26 November 2015

Abstract

OBJECTIVES: Swine models are widely used to develop new techniques and materials for the treatment of heart valve disease like aortic valve and mitral valve transcatheter interventions and to train physicians in these techniques. Transoesophageal echocardiography (TOE) is crucial in these models. We defined standard planes of 2D and 3D TOE in healthy pigs undergoing transcatheter heart valve interventions.

METHODS: Twenty healthy pigs (weight 56–106 kg) underwent different mitral and aortic valve interventions (transcatheter aortic valve implantations, implantations of a mitral band, bicuspidization of the aortic valve, trans-septal punctures). For image guidance of the procedures, an adult TOE probe was introduced under direct vision in the oesophagus. Before the procedure itself was performed, a standardized protocol was used to determine normal values for anatomical and functional echocardiographic parameters.

RESULTS: Positioning of the probe was possible in all animals and ideal when achieving a distance from the front teeth (incisors) of 40–60 cm. Anteflexion and lateroflexion of the probe was necessary to achieve optimal imaging quality. 2D visualization of all relevant cardiac structures was possible. The aortic annulus diameter was 24.1 ± 2.5 mm, the sinus of valsalva diameter was 30.6 ± 4 mm and the sinotubular junction diameter was 25.2 ± 4 mm. The ascending aorta had a diameter of 24 ± 4 mm and the descending aorta a diameter of 16 ± 5 mm. The mitral valve anterior-posterior diameter was 31.8 ± 4 mm and the commissure to commissure diameter was 40.5 ± 5 mm resulting in a mitral valve area of $10.7 \pm 1.5 \text{ cm}^2$. 3D visualization was possible for the aortic and the mitral valve. None of the animals showed any pathology except one that had a dilated left ventricle and moderate mitral valve insufficiency. Left and right ventricular dimensions and the anatomy of the aortic-, mitral-, tricuspid and pulmonary valve as well as of the aorta were comparable with those of the human anatomy.

CONCLUSIONS: 2D and 3D TOE can be routinely applied as image guidance in pigs used as a model for the development and training of new techniques to treat heart valve disease.

Keywords: Animal model • Transoesophageal echocardiography • Minimally invasive surgery • Transcatheter valve therapy

INTRODUCTION

Domestic pigs (*Sus Scrofa*) are used as an animal model for preclinical evaluation and investigation of new heart valve prostheses and therapies due to their similarities to the human physiology and anatomy of the heart and vessels, and their good availability [1–3]. Furthermore, good correlation between weight and sizes of the valvular annuli, short but well-defined ascending aorta and aortic arch curvature stronger than the ones found in cloven-footed animals have been described in pigs [4, 5]. These models are also widely used to train physicians in these new techniques. Important imaging modality for aortic valve and mitral valve interventions is transoesophageal echocardiography (TOE). The use of TOE in transcatheter aortic valve implantation (TAVI) procedures and transcatheter

mitral valve interventions (i.e. the MitraClip procedure) is extensively described in the literature [6–9]. For the use of TOE in large swine models, the literature is very limited [10]. For the development and the training of new transcatheter techniques in large swine models, TOE for image guidance of the procedure is crucial as well.

The aim of this study was to show the feasibility of TOE in swine to develop a TOE approach and establish standard values for a large swine animal model that can be used during the development and training of transcatheter heart valve therapies.

METHODS

The animal housing and experimental protocols were approved by the Cantonal Veterinary Department, Zurich, Switzerland, under

licence no. ZH 152/2013, and were in accordance with Swiss Animal Protection Law. Housing and experimental procedures were also conforming to the European Directive 2010/63/EU of the European Parliament and of the Council on the protection of animals used for scientific purposes and to the Guide for the Care and Use of Laboratory Animals (Institute of Laboratory Animal Resources, National Research Council, National Academy of Sciences, 2011).

The animals were included in different projects within the licence covering transcatheter aortic valve replacement with standard transcatheter heart valve prosthesis (i.e. Symetis ACURATE TA Aortic prosthesis) and transcatheter mitral valve repair techniques (Valtech Cardioband [11], Cardiosolutions Mitra-Spacer [12]).

TOE was part of the study protocols. The examinations were performed in the operating room before the interventions were started; no additional animals were needed for this study.

Twenty domestic pigs with a median weight of 92.5 kg (56–106 kg) were included in the study. All animals received premedication with ketamine (20 mg/kg), azaperone (1.5 mg/kg) and atropine (0.75 mg) intramuscularly. After the loss of postural reflexes, the animals were transported to the surgical preparation room. The anaesthesia was deepened by a bolus injection of propofol (1–2 mg/kg)

and the trachea of the animal was intubated. Anaesthesia was then maintained with 2–3% of isoflurane in 1 : 1 oxygen/air mixture (4–5 l/min). Amiodarone (2–3 mg/kg bolus i.v.) was administered to stabilize the heart rhythm. Animals were placed on the operating table in dorsal recumbence.

After the induction of anaesthesia, real-time 3D TOE Philips iE33 (Philips Medical Systems, Andover, MA, USA) was performed using a standard adult matrix array TOE probe X7-2t (Philips Medical Systems). The probe was covered with a latex coat that was floated with ultrasonic gel (Skintact, Leonhard Lang GmbH, Innsbruck, Austria) and was introduced under laryngoscopic sight, lifting the tongue and the lower jaw with the spatula. The TOE probe was introduced from the right side of the pig's pharynx to find the oesophagus below the trachea. For introduction, the probe was kept unblocked in neutral position.

Two-dimensional transoesophageal echocardiography

The examination was started at around 55 cm from the incisors. The exact depth of the probe, the flexion of the tip of the probe and the rotation of the transducer were adapted for optimal imaging. An issue of TOE in pigs is the anatomy of the bronchial system. The main bronchus is located between oesophagus and the heart (Fig. 1). Therefore, strong anteflexion and lateroflexion with the tip of the probe is needed to avoid the interferences with the bronchus. After anteflexion and lateroflexion of the tip of the probe and forward rotation of the transducer between 0 and 20° or 160 and 180° (Fig. 2), a modified four-chamber view was generated. Although the left cavities were well visualized in this view, the right heart structures, particularly the tricuspid valve and the right ventricle could be partially hidden behind the main bronchus. Systolic and diastolic wall thickness of the free walls of the left and the right ventricle as well as of the septal wall was measured. Further anteflexion and lateroflexion of the tip of the probe at this level allowed the visualization of a short-axis view of the aortic valve and an inflow-outflow view of the right ventricle (Fig. 3). To assess mitral valve function and anatomy in a two-chamber view, a rotation of the transducer angle to 40–60° was used and transmural Doppler obtained (Fig. 4). The probe was left at the same level in the oesophagus, and the transducer was rotated between 50 and 70° to achieve a mid-oesophageal long-axis view (Fig. 5). The diameters of the aortic annulus, sinus of Valsalva, sinotubular junction and ascending aorta were measured

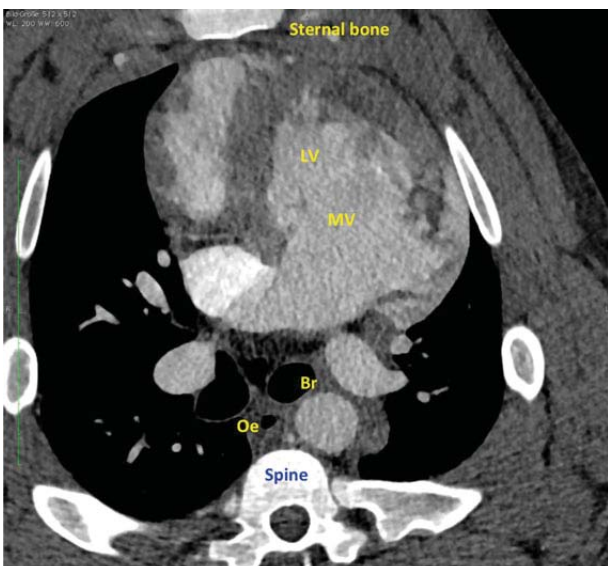


Figure 1: Computed tomography of n pig. MV: mitral valve; LV: left ventricle; Oe: oesophagus; Br: bronchus.

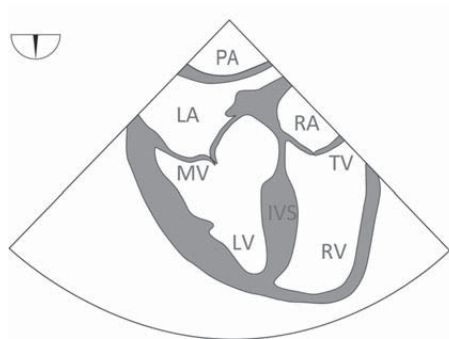


Figure 2: Four-chamber view. Left side shows a schematic. Right side shows an exemplary image. MV: mitral valve; TV: tricuspid valve; IVS: inter-ventricular septum; LV: left ventricle; RV: right ventricle; LA: left atrium; RA: right atrium; PA: pulmonary artery.

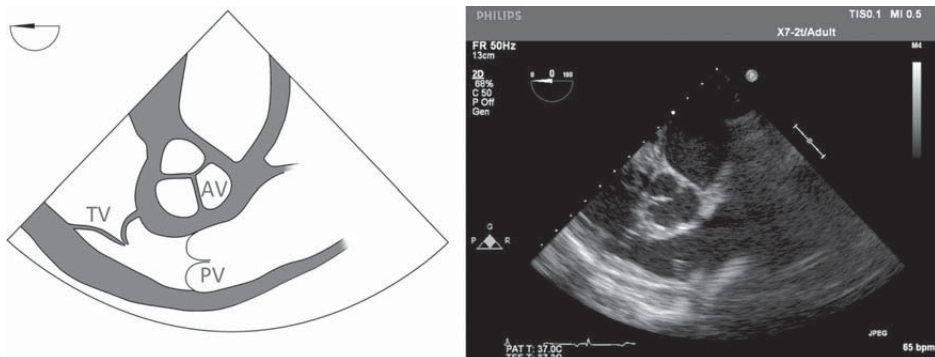


Figure 3: Aortic valve in SAX and right ventricular inflow-outflow view. AV: aortic valve; TV: tricuspid valve; PV: pulmonary valve; SAX: short-axis.

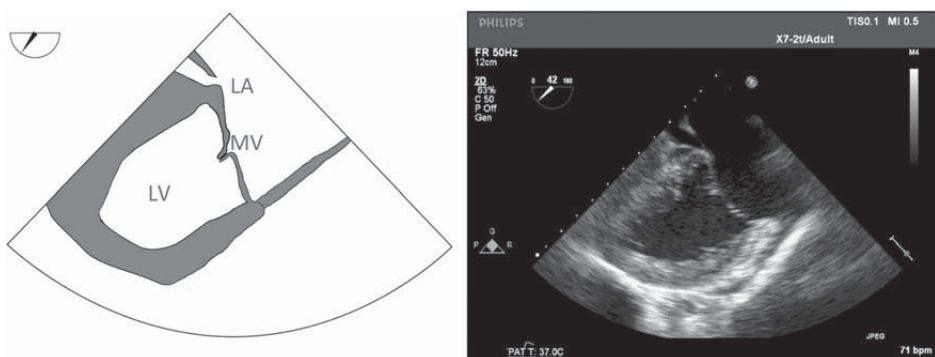


Figure 4: Mitral valve in a two-chamber view. MV: mitral valve; LV: left ventricle; LA: left atrium.

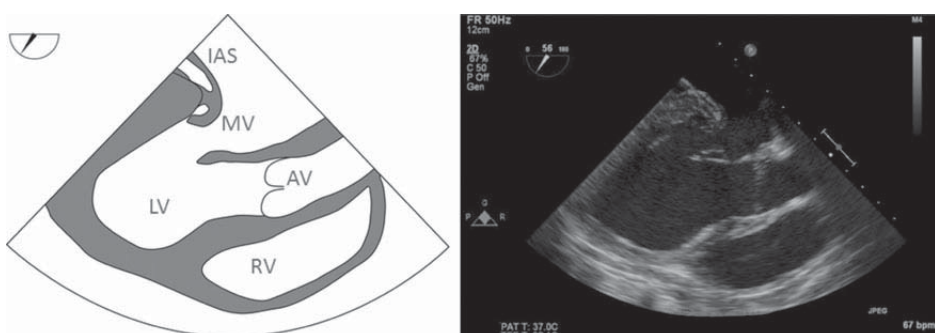


Figure 5: Mid-oesophageal LAX view. Left side shows a schematic. Right side shows an exemplary image. LAX: long-axis; IAS: interatrial septum; MV: mitral valve; AV: aortic valve; LV: left ventricle; RV: right ventricle.

in this view. The left ventricular mid-papillary end-systolic and end-diastolic diameters (LVESD and LVEDD) and the left ventricular end-systolic and end-diastolic volumes (LVESV and LVEDV) using Simpson's rule were assessed and the left ventricular ejection fraction (LVEF) was calculated. Cardiac output was obtained from the multiplication of the ejection volume and the heart rate. Using the 3D software X-Plane on the aortic valve in long-axis, a short-axis of the aortic valve was obtained, with the inflow-outflow view of the right ventricle. From this position, the probe was then pulled back of 10 cm and the transducer angle rotated between 0 and 60°. The aortic and the pulmonary valve could then be seen in long-axis view, parallel to each other and parallel to the probe. Small rotations of the probe were necessary to focus on each valve separately. In this position, Doppler echocardiography was performed to measure the peak and the mean gradient,

the peak and the mean jet velocity and the velocity time integral through the aortic and the pulmonary valve (Fig. 6).

Three-dimensional transoesophageal echocardiography

3D imaging of aortic, pulmonary and mitral valves was always possible; 3D imaging of the tricuspid valve was generally more difficult to obtain because of its anterior position and the extremely fine quality of its leaflets. Main focus was laid on the aortic and the mitral valve. Examples are shown in Videos 1 and 2. 3D views of the mitral and the aortic valve were obtained from the long-axis bidimensional imaging (rotation of the probe between 50 and 70° as shown in Fig. 5). For 3D measurement of the mitral valve

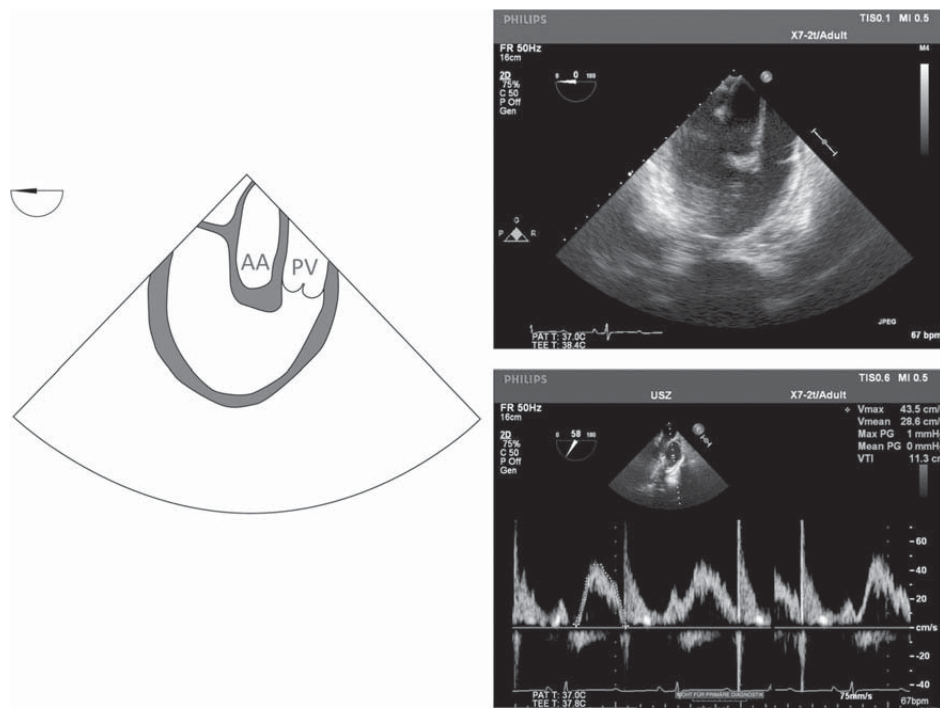
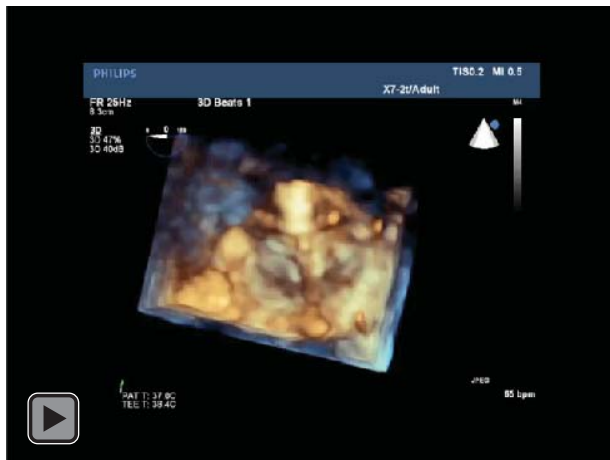


Figure 6: Aorta and pulmonary valve shown in parallel. Left image shows a schematic. Right image shows an exemplary TOE image and the Doppler measurement in the pulmonary valve. AA: ascending aorta; PV: pulmonary valve; TOE: transoesophageal echocardiography.



Video 1: 3D Transoesophageal echocardiography of the aortic valve.

opening area, we used the 3D quantification software (3DQ-QLab) by Philips Medical Systems. 3DQ is widely used for quantification in 3D. The mitral valve was displayed in three orthogonally orientated planes and the plane in which the measurement was performed was orientated perpendicularly to the valve leaflets. An example of these measurements is shown in Fig. 7.

Statistics

All variables were tested for normal distribution with the Kolmogorow-Smirnow and the Shapiro-Wilk test. If normal distribution was present, the mean with standard deviation was calculated. In all other cases, the median with the range was calculated. To test the correlation of weight and cardiac dimensions, Pearson's



Video 2: 3D Transoesophageal echocardiography of the mitral valve.

R was calculated. A P-value of <0.05 was defined as high enough to decline the null hypothesis.

RESULTS

Insertion of the TOE probe was possible in all animals. The depth of insertion from the front teeth (incisors) row varied from 40 to 60 cm. The mean depth for visualization of the aortic, the mitral and the tricuspid valves was 53 ± 5 cm. To visualize the pulmonary valve, the probe had to be pulled back ~ 10 cm to a mean depth of 45 ± 4 cm (range from 35 to 55 cm). Mean heart rate during the examinations was 67 ± 8 beats per minute. Except in one animal, which had a dilated left ventricle with consecutive mitral valve insufficiency, no pathologies were found. Values for left ventricular dimensions and

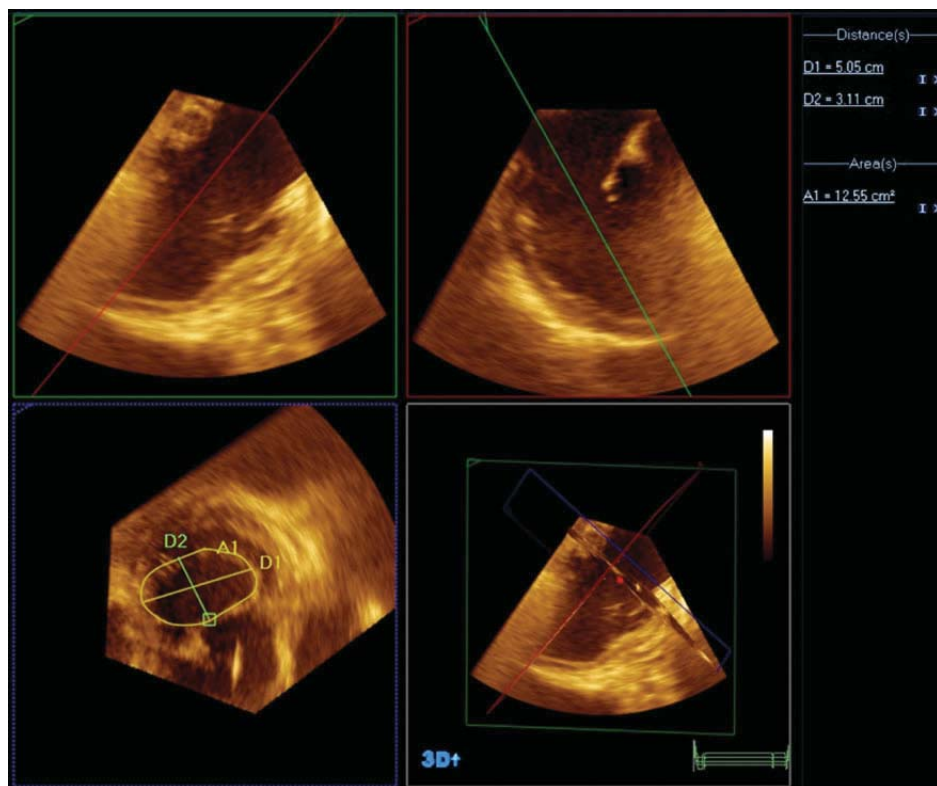


Figure 7: Measurement of the mitral valve dimensions with Philips' QLab. D1: commissure-to-commissure diameter; D2: antero-posterior diameter; A1: mitral valve area.

function, aortic root and aortic dimensions as well as functional parameters for the aortic and the mitral valve are presented in Table 1. With more experience, the pulmonary valve was assessed as well. Results are available for 13 animals.

There was a significant correlation of body weight with the diameters of the aortic annulus ($R = 0.6$; $P < 0.01$), left ventricular outflow tract ($R = 0.7$; $P < 0.001$), sinus of Valsalva ($R = 0.6$; $P < 0.01$) and sinotubular junction ($R = 0.7$; $P < 0.001$). Animals with a body weight of 56–65 kg had annulus diameters of 20–24 mm. All animals with a body weight of >100 kg had annulus diameters of at least 25 mm (up to 30 mm) except one animal with an annulus diameter of 24.4 mm. There was also a correlation of the body weight with the mitral valve annulus area ($R = 0.6$; $P < 0.01$), the antero-posterior ($R = 0.5$; $P < 0.05$) and inter-commissural diameters ($R = 0.7$; $P < 0.001$) of the mitral valve. Animals with a body weight of >95 kg had a mitral valve annulus area of $>10.5 \text{ cm}^2$.

DISCUSSION

In this study, we demonstrate feasibility, show landmark data and suggest a method, closely resembling actual TOE standard in humans that can be used as the imaging modality in large porcine model for preclinical testing and training of transcatheter heart valve therapies.

2D and 3D TOE in experimental, closed chest porcine models is feasible. To the best of our knowledge, there is only one study available that systematically describes transoesophageal echocardiographic findings in pigs [11]. At this time, 3D echocardiography was not yet available. In that publication, TOE and intracardiac ultrasound were used to describe cardiac dimensions. Left ventricular diameters and

wall thickness were comparable with those of our findings. In contrast, end-systolic and end-diastolic volumes were found to be lower in our study. Consequently, we also found a lower stroke volume but the same LVEF. We used Simpson's rules to measure the ventricular volumes whereas the biplane area-length formula was used previously by Ren *et al.* The use of the modified Simpson's rules to assess left ventricle volume has been shown to be reliable in humans [15]. The ventricular volume might be underestimated because of the foreshortening of the apex in TOE.

Ascending and descending aortic dimensions were similar in both studies. Aortic root dimensions as well as mitral valve dimensions were not published previously in [11]. However, these parameters are important nowadays for the planning of animal experiments. Porcine models play an important role in the development of transcatheter heart valve therapies. The first implantation of a valve in a stent for closed chest aortic valve implantation in a pig model was described in 1992 [16]. In 2002, the first human case of a balloon expandable stent-valve implantation was described [17]. The first human implantation of a CoreValve prosthesis was performed in 2004 [18] after extensive testing in a porcine model [19]. Since then, TAVI grew rapidly and numerous new prostheses appeared on the market. In this setting, acute porcine experiments played and still play an important role. One major topic is the development of new prostheses. Another main issue is the need for training of the physicians performing the procedures. Many companies request an animal training before the first human implantations for new implanters.

After the rise of TAVI, the mitral valve is the next target for transcatheter therapies. Different devices are under preclinical and clinical testing. Among others, a transcatheter mitral annuloplasty band has been developed and tested heavily in a porcine model [11].

Table 1: Echocardiographic findings in pigs

	Study values pig (<i>n</i> = 20)	Normal values human
Heart rate (bpm)	67 ± 8 [55–81]	
Left ventricular dimensions and function		1.
LVESD (mm)	34 ± 4 [27–41]	22–35 ^a
LVEDD (mm)	49.6 ± 4.7 [39–59]	38–52 ^a
LVESV (ml)	37.1 ± 10 [22–62]	14–42 ^a
LVEDV (ml)	88.4 ± 21.5 [61–147]	46–106 ^a
LVEF (%)	58.1 ± 7.4 [47–71]	≥55 ^a
BV (ml)	51.9 ± 15 [30–85]	
CO (ml/min)	3421 ± 815.7 [2040–5346]	
CI (ml/min/kg)	43.4 ± 11.5 [19–65]	
IVS wall thickness syst. (mm)	15.5 ± 0.7 [10–21]	6–9 ^a
IVS wall thickness diast. (mm)	10.9 [7–13]	6–9 ^a
Aortic root and aorta		
Aortic annulus diameter (mm)	24.1 ± 2.5 [20–30]	20–31 ^b
Sinus of Valsalva diameter (mm)	30.6 ± 4 [24–39]	29–45 ^b
Sinotubular junction diameter (mm)	25.2 ± 4 [20–33]	22–36 ^b
Ascending aorta diameter (mm)	24 ± 4 [19–33]	22–36 ^b
Descending aorta diameter (mm)	16 ± 5	20–30 ^b
Max. jet velocity aortic valve (m/s)	0.75 ± 0.2 [44–128]	
Mean jet velocity aortic valve (m/s)	0.5 ± 0.1 [19–87]	
Max. gradient aortic valve (mmHg)	2 [1–6]	
Mean gradient aortic valve (mmHg)	1 [0–4]	
Mitral valve		
Mitral valve diameter ap (mm)	31.8 ± 4 [25–38]	
Mitral valve diameter cc (mm)	40.5 ± 5 [32–51]	
Mitral valve area (cm ²)	10.7 ± 1.5 [8–13]	
Max. jet velocity mitral valve (cm/s)	57.6 ± 12 [39–83]	
Mean jet velocity mitral valve (cm/s)	29.4 ± 5.5 [20–41]	
Max. gradient mitral valve (mmHg)	1 [1–3]	
Mean gradient mitral valve (mmHg)	0 [0–1]	
Pulmonary valve		
Max. jet velocity pulmonary valve (cm/s)	45 ± 8	
Mean jet velocity pulmonary valve (cm/s)	30 ± 5	
Max. gradient pulmonary valve (mmHg)	0 [0–1]	
Mean gradient pulmonary valve (mmHg)	0 [0–1]	
RV wall thickness systole	8.5 ± 2.1	
RV wall thickness diastole	4.6 ± 1.7	

LVESD: left ventricular end-systolic diameter; LVEDD: left ventricular end-diastolic diameter; LVESV: left ventricular end-systolic volume; LVEDV: left ventricular end-diastolic volume; LVEF: left ventricular ejection fraction; BV: beating volume; CO: cardiac output; CI: cardiac index; IVS: inter-ventricular septum; syst.: in systole; diast.: in diastole; Max.: maximum; ap: anterior-posterior; cc: commissure-to-commissure. RV: right ventricular. All animals and the animal with the pathologic mitral valve are included in Table 1.

^aLang et al. [13].

^bEvangelista et al. [14].

Transcatheter mitral valve replacement is on the rise. For these therapies, preclinical testing [20, 21] and training are crucial as well. Especially for these new mitral valve therapies, echocardiography is indispensable and has to be started in the preclinical phase. The advantage of TOE in pig models is that, compared with human anatomy, several similarities can be found: the aortic valve is tricuspid and the aortic root dimensions are comparable with the human anatomy as well as cardiac chamber dimensions and the mitral valve anatomy. The mitral valve has an anterior and a posterior leaflet and the annulus has a similar shape. These findings underline that 2D and 3D TOE in animal experiments with pigs represents a useful tool for preclinical testing of transcatheter valve therapies under 'human-like' conditions. Beating heart mitral valve repair procedures, TAVI, as well as atrial and ventricular septal defect device closure all rely on limited intraprocedural visualization that could be enhanced with this guide.

In the present study, we demonstrate feasibility, show landmark data and suggest a method, closely resembling actual TOE

standard in humans that can be used in large porcine model for preclinical testing of devices and training of clinicians.

Conflict of interest: none declared.

REFERENCES

- [1] <http://pubs.nal.usda.gov/sites/pubs.nal.usda.gov/files/srb94-01.html> (27 November 2015, date last accessed).
- [2] Gallegos RP, Nockel PJ, Rivard AL, Bianco RW. The current state of in-vivo pre-clinical animal models for heart valve evaluation. *J Heart Valve Dis* 2005;14:423–32.
- [3] Kleine P, Abdel-Rahman U, Klesius AA, Scherer M, Simon A, Moritz A. Comparison of hemodynamic performance of Medtronic Hall 21 mm versus St. Jude Medical 23 mm prostheses in pigs. *J Heart Valve Dis* 2002;11:857–63.
- [4] Allan JS, Rose GA, Choo JK, Arn JS, Vesga L, Mawulawde K et al. Morphometric analysis of miniature swine hearts as potential human xenografts. *Xenotransplantation* 2001;8:90–3.

- [5] How T. Advances in Hemodynamics and Hemorheology. Elsevier Science, Philadelphia, 1996, 328.
- [6] Patel PA, Fassi J, Thompson A, Augoustides JG. Transcatheter aortic valve replacement—part 3: the central role of perioperative transesophageal echocardiography. *J Cardiothorac Vasc Anesth* 2012;26:698–710.
- [7] Zamorano JL, Badano LP, Bruce C, Chan KL, Gonçalves A, Hahn RT et al. EAE/ASE recommendations for the use of echocardiography in new transcatheter interventions for valvular heart disease. *Eur Heart J* 2011;32:2189–214.
- [8] Biaggi P, Felix C, Gruner C, Herzog BA, Hohlfeld S, Gaemperli O et al. Assessment of mitral valve area during percutaneous mitral valve repair using the MitraClip system: comparison of different echocardiographic methods. *Circ Cardiovasc Imaging* 2013;6:1032–40.
- [9] Flachskampf FA, Wouters PF, Edvardsen T, Evangelista A, Habib G, Hoffman P et al. Recommendations for transoesophageal echocardiography: EACVI update 2014. *Eur Heart J Cardiovasc Imaging* 2014;15:353–65.
- [10] Ren JF, Schwartzman D, Lighty GW Jr, Menz V, Michele JJ, Li KS et al. Multiplane transesophageal and intracardiac echocardiography in large swine: imaging technique, normal values, and research applications. *Echocardiography* 1997;14:135–48.
- [11] Maisano F, Vanermen H, Seeburger J, Mack M, Falk V, Denti P et al. Access transcatheter mitral annuloplasty with a sutureless and adjustable device: preclinical experience. *Eur J Cardiothorac Surg* 2012;42:524–9.
- [12] Svensson LG, Ye J, Piemonte TC, Kirker-Head C, Leon MB, Webb JG. Mitral valve regurgitation and left ventricular dysfunction treatment with an intravalvular spacer. *J Card Surg* 2015;30:53–4.
- [13] Lang RM, Bierig M, Devereux RB, Flachskampf FA, Foster E, Pellikka PA et al. Recommendations for chamber quantification. *Eur J Echocardiogr* 2006;7:79–108.
- [14] Evangelista A, Flachskampf FA, Erbel R, Antonini-Canterin F, Vlachopoulos C, Rocchi G et al. Echocardiography in aortic diseases: EAE recommendations for clinical practice. *Eur J Echocardiogr* 2010;11:645–58.
- [15] Tortoledo FA, Quiaones MA, Fernandez GC, Waggoner AD, Winters WL. Quantification of left ventricular volumes by two-dimensional echocardiography: simplified and accurate approach. *Circulation* 1983;67:579–84.
- [16] Andersen HR, Knudsen LL, Hasenkam JM. Transluminal implantation of artificial heart valves: description of a new expandable aortic valve and initial results with implantation by catheter technique in closed chest pigs. *Eur Heart J* 1992;13:704–8.
- [17] Cribier A, Eltchaninoff H, Bash A, Borenstein N, Tron C, Bauer F et al. Percutaneous transcatheter implantation of an aortic valve prosthesis for calcific aortic stenosis: first human case description. *Circulation* 2002;106:3006–8.
- [18] Grube E, Laborde JC, Zickmann B, Gerckens U, Felderhoff T, Sauren B et al. First report on a human percutaneous transluminal implantation of a self-expanding valve prosthesis for interventional treatment of aortic valve stenosis. *Catheter Cardiovasc Interv* 2005;66:465–9.
- [19] Ferrari M, Figulla HR, Schlosser M, Tenner I, Frerichs I, Damm C et al. Transarterial aortic valve replacement with a self-expanding stent in pigs. *Heart* 2004;90:1326–31.
- [20] Banai S, Verheyen S, Cheung A, Schwartz M, Marko A, Lane R et al. Transapical mitral implantation of the Tiara bioprosthesis: pre-clinical results. *JACC Cardiovasc Interv* 2014;7:154–62.
- [21] Iino K, Boldt J, Lozonschi L, Metzner A, Schoettler J, Petzina R et al. Off-pump transapical mitral valve replacement: evaluation after one month. *Eur J Cardiothorac Surg* 2012;41:512–7.

3 Diskussion

In den ersten beiden der vorliegenden Studien wurden CT-Bilddaten verwendet, um die dreidimensionale Anatomie der Mitralklappe darzustellen. In 2.1 konnte gezeigt werden, dass die Bildqualität ausreicht, um exakte Modelle des Mitralklappenannulus in Form eines patientenspezifischen Annuloplastieringes zu generieren und zu produzieren. Eine ähnliche Methode wurde 2010 von Díaz Lantada und Kollegen beschrieben⁴⁰. In dieser Studie wurde in einem CAD-CAM-Verfahren (*Computer Aided Design and Computer Aided Manufacturing*) ein Annuloplastierung aus Epoxidharz durch Stereolithographie produziert. Dieser Ring war jedoch nie für die Implantation vorgesehen, allein schon aus dem Grund, dass das verwendete Material nicht biokompatibel ist. Es gelang jedoch der *Proof of concept*. Im Gegensatz zu dieser Studie waren die Ringe, die in der hier aufgeführten Studie verwendet wurden, aus einer biokompatiblen Titanlegierung. Außerdem wurden Löcher für die Nähte zur Annaht des Ringes am nativen Annulus im Ring ausgespart, so dass der Ring fixiert werden konnte. Dies wurde dann im Schwein auch erfolgreich getan. Somit gelang es zu zeigen, dass die Produktion und Implantation von patientenspezifischen Annuloplastieringen möglich ist. Limitierend bei der Studie war, dass die Ringe gesunden Schweinen implantiert wurden. Außerdem entsprachen sie genau der Form des potentiell pathologisch veränderten Annulus. Um therapeutisch eingesetzt zu werden müsste ein Ring produziert werden, welcher zu einer wirklichen Annuloplastie, also Veränderung der Annulusform und -größe führt, wie dies mit den kommerziell erhältlichen Ringen angestrebt wird⁴¹. Für die Zukunft wäre anzustreben, für eine bestimmte Pathologie der Mitralklappe eine Therapiesimulation durchzuführen und anhand dieser die ideale Form des Annuloplastierings zu ermitteln. Verschiedene Projekte in diese Richtung sind geplant.

Abgesehen von der Produktion patientenspezifischer Annuloplastieringe wird die CT in den letzten Jahren mehr und mehr auch für die bildgebende Darstellung der Mitralklappe angewendet. Eine Studie zur Anwendung der *Multi-Slice CT* (MSCT) der Mitralklappe stammt von Willmann und Kollegen aus dem Jahr 2002⁴². Es konnte gezeigt werden, dass eine 95%–100%ige Übereinstimmung der Befunde bzgl. Verdickung der Segel und Kalzifikation in echokardiographischen Daten und CT-Daten durch zwei Probanden bestand. Somit konnte gezeigt werden, dass die Bildqualität der MSCT ausreicht, um anatomische Details der Mitralklappe und der dazugehörigen Strukturen zu visualisieren und pathologische Veränderungen festzustellen. Allerdings handelt es sich hierbei nur um eine grobe Beurteilung der Mitralklappe. Anatomische Merkmale der Klappe wie Annulusfläche oder Annulusdurchmesser wurden nicht gemessen. In einer Studie von Messika-Zeitoun und Kollegen

wurde 2006 die Öffnungsfläche der Mitralklappe bei Patienten mit Mitralklappenstenose in der MSCT ausgemessen⁴³. Drei Untersucher werteten die Daten aus, zwei erfahrene Untersucher und ein unerfahrener Radiologie-Assistent. Die Ergebnisse wurden mit den Ergebnissen der echokardiographischen Ausmessung verglichen. Es zeigten sich weder zwischen den erfahrenen und unerfahrenen Untersuchern noch im Vergleich zur Echokardiographie signifikante Unterschiede bzgl. der ausgemessenen Mitralklappenöffnungsflächen. Daher wurde zusammengefasst, dass die MSCT reproduzierbar und ohne großen Zeitaufwand zur Bestimmung des Schweregrades der Mitralklappenstenose verwendet werden kann und zum Repertoire der Untersuchungstechniken der Mitralklappe hinzugefügt werden sollte. In den folgenden Jahren entwickelte sich die CT auch technisch weiter vom 16-Zeilen-Scanner wie in der eben erwähnten Studie hin zu *Dual-Source*-Scannern mit 128 Sektionen in aktuellen Studien^{44,33}. Die aktuell mögliche räumliche Auflösung von ca. 0,5 mm ermöglicht eine präzise Darstellung der Mitralklappe. Zahlreiche Studien haben sich mit der CT-basierten Darstellung sowohl der nativen Anatomie⁴⁵ als auch verschiedener pathologischer Konstellationen⁴⁶ beschäftigt; Ghersin und Kollegen haben beispielsweise die anatomische Relation der Koronararterie zur Mitralklappe in der CT untersucht⁴⁷. Untersucht wurden 70 Patienten, darunter 40, welche als gesunde Kontrollgruppe eingeschlossen wurden. Es zeigte sich eine relevante Nähe insbesondere des Ramus circumflexus zum Mitralklappenannulus etwas lateral des linken Trigonums. Bei einem Drittel der Patienten lag der Abstand sogar bei unter 5 mm. Diese Information kann z. B. vor chirurgischen Eingriffen an der Mitralklappe relevant sein, bei welchen eine Ringannuloplastie durchgeführt wird, da in dieser Region bei der Nahtanlage zur Fixierung des Annuloplastierings besondere Vorsicht geboten ist.

Mehrere Studien haben gezeigt, dass eine beträchtliche Varianz der Anatomie bei verschiedenen Pathologien der Mitralklappe besteht⁴⁸. Beispielsweise untersuchten Gordic und Kollegen in der CT Mitralklappenannulusparameter bei Gesunden und bei Patienten mit verschiedenen Ausprägungen einer funktionellen Mitralklappeninsuffizienz⁴⁹. Es zeigten sich signifikante Unterschiede bzgl. Fläche des septo-lateralen Durchmessers und Umfang des posterioren Abschnitts des Mitralklappenannulus sowohl zwischen Patienten ohne valvuläre Herzerkrankung und Patienten mit funktioneller Mitralklappeninsuffizienz als auch zwischen Patienten mit moderater und schwerer Mitralklappeninsuffizienz. Keine Unterschiede zeigten sich hingegen sowohl für den Umfang des anterioren Anteils des Mitralklappenannulus als auch für den Abstand von Kommissur zu Kommissur. Die Ergebnisse zeigen, dass eine genaue präoperative Evaluation der Anatomie der Mitralklappe durch die CT möglich und bei der Planung von Eingriffen relevant ist.

Auch zur Darstellung der degenerativen Mitralklappeninsuffizienz mittels CT wurden Studien durchgeführt. Ghosh und Kollegen untersuchten die Genauigkeit der Darstellung der Mitralklappen bei Patienten mit Mitralklappenprolaps im Vergleich zur Echokardiographie⁵⁰. Bei 63 Patienten, bei welchen eine Mitralklappenoperation durchgeführt wurde, wurden präoperativ CTs durchgeführt. Es zeigte sich, dass ein Prolaps im CT genauso gut zu erkennen ist wie in der Echokardiographie. Allerdings war die Identifikation der Lokalisation des prolabierte Segments deutlich niedriger als in der Echokardiographie.

Insbesondere im Bereich der kathetergestützten Behandlung der Mitralklappenerkrankung hat die CT in den letzten Jahren deutlich an Bedeutung gewonnen. In 2.2 wird eine Studie angeführt, in welcher ein CT-Protokoll für die präoperative Planung eines kathetergestützten Systems zur Mitralklappenannuloplastie entwickelt und evaluiert wurde. Die Entwicklung fand in der präklinischen Phase am Großtiermodell statt, ließ sich aber direkt in die klinische Anwendung übertragen⁵¹. Bei den ersten kathetergestützten Systemen zur Behandlung der Mitralklappeninsuffizienz handelte es sich um Devices, welche wegen der Nähe zum Mitralklappenannulus in den Koronarsinus implantiert wurden, um über diesen eine Veränderung der Annulusgeometrie herbeizuführen. Wie in der unter 2.2 angeführten Studie ist für die Planung dieser Eingriffe die CT ebenfalls entscheidend, da der Koronarsinus große Varianzen bzgl. der Lage zum Mitralklappenannulus aufweist^{52,53}. Beispielsweise untersuchten Choure und Kollegen 25 Patienten ohne Mitralklappeninsuffizienz und 11 Patienten mit schwerer Mitralklappeninsuffizienz bei Prolaps der Mitralklappe⁵⁴. Es zeigte sich eine große anatomische Varianz. Insbesondere lag der Koronarsinus bei Patienten mit Mitralklappeninsuffizienz weiter vom Annulus entfernt als bei Patienten ohne Mitralklappenpathologie, was für die Therapie ungünstig ist. Es wurde zusammengefasst, dass diese interindividuellen Varianzen bei der präprozeduralen Planung unbedingt berücksichtigt werden sollte.

In den letzten Jahren hat eine rasante Entwicklung von Prothesen stattgefunden, welche kathetergestützt in Mitralposition implantiert werden können. Diese Therapieform wird vorerst nur bei Hochrisikopatienten eingesetzt werden, welche nicht für einen chirurgischen Eingriff qualifizieren. Grund hierfür ist, dass es sich um eine neuartige Therapieform handelt, für die noch keinerlei Langzeitergebnisse vorliegen. Auch für die Transkatheter-Mitralklappenimplantation (TMVI) ist die CT eine wichtige Modalität, da die Implantation der Prothese bildgestützt und nicht unter direkter Sicht erfolgt. Daher ist eine präprozedurale Planung der Prothesenart und -größe entscheidend. Die CT wurde in verschiedenen Publikationen als geeignete Bildmodalität vorgeschlagen. Von Blanke und Kollegen wurde die

CT verwendet, um die Annulusform und -größe im Zusammenhang mit TMVI zu untersuchen⁵⁵. In ihrer Arbeit schlagen sie vor, die anatomische dreidimensionale Sattelform des Mitralklappenannulus zu Gunsten des zweidimensionalen, D-förmigen Annulus unter Aussparung des Horns des anterioren Mitralklappenannulus für die Planung von TMVI-Prozeduren zu verwenden, da dies zwar nicht anatomisch korrekt, für die Positionierung aber relevanter ist. Thériault-Lauzier und Kollegen beschreiben eine systematische Methodologie zur Ausmessung für TMVI-relevante Parameter im Bereich der Mitralklappe im Zusammenhang mit TMVI²⁶. Zwei unabhängige Untersucher führten die Messungen durch. Es konnte gezeigt werden, dass die CT alle Ausmessungen von für TMVI relevanten Strukturen ermöglichte und dass eine gute InterobserverReproduzierbarkeit bestand. In einer zweiten Studie der gleichen Gruppe²⁷ wurde spezifisch eine Gruppe von Patienten mit funktioneller Mitralklappeninsuffizienz evaluiert. Dies entspricht dem Patientengut, welches am ehesten für eine TMVI in Frage kommt. Es konnte gezeigt werden, dass sich die Anatomie des Mitalannulus während des Herzzyklus bei diesen Patienten kaum verändert, also beispielsweise der Annulusdurchmesser während des Herzzyklus relativ konstant bleibt. Beide Studien unterstreichen den Stellenwert der CT bei der patientenspezifischen Therapieplanung von kathetergestützten Eingriffen an der Mitralklappe.

3.1 Verwendung von CT-Bilddaten zur Simulation von kathetergestützten Aortenklappenimplantationen

Verschiedene Modelle zur computerbasierten Simulation von Herzklappen existieren⁵⁶. Vor allem Finite Elemente Modelle (FEM) wurden in den letzten Jahren für die Simulation von TAVI-Prozeduren exploriert. In dieser Habilitationsschrift wurden in den in 2.3, 2.4 und 2.5 aufgeführten Studien diese Modelle verwendet, um verschiedene Aspekte der TAVI-Prozedur zu simulieren und zu untersuchen. Insbesondere wurde auch ein spezieller Fokus auf die Korrelation mechanischer Komponenten und deren klinische Relevanz hinsichtlich typischer Komplikationen wie paravalvuläre Lecks und Schrittmacher-Neuimplantationen gelegt.

In der unter 2.3 aufgeführten Studie wurde untersucht, ob die virtuelle Implantation von TAVI-Prothesen in patientenspezifische Aortenmodelle zur Planung von TAVI-Eingriffen vorteilhaft ist. Es zeigte sich, dass bei einem überwiegenden Teil der Patienten, bei welchen in der retrospektiven Planung mit der patientenspezifischen Planungssoftware eine kleinere Prothese gewählt worden wäre, eine Schrittmacher-Neuimplantation notwendig war. Umgekehrt zeigte sich bei einem Großteil der Patienten, bei welchen retrospektiv eine größere Prothese geplant

worden wäre, ein paravalvuläres Leck. Somit konnte gezeigt werden, dass die Verwendung von Planungshilfen, welche eine virtuelle Implantation von TAVI-Prothesen ermöglichen, durchaus zur besseren, individuellen Planung beitragen können. Soweit uns bekannt ist ist dies die einzige Studie, welche sich mit der Evaluation einer solchen Software im klinischen Alltag bisher beschäftigt hat. Einschränkend ist zu erwähnen, dass es sich hier um eine rein visuelle Planung der Prozedur gehandelt hat. Mechanische Eigenschaften des Stents wie z. B. Verformung wurden nicht berücksichtigt, sondern nur die Größe der Prothese. Mit einem mehr mechanischen Ansatz beschäftigen sich die unter 2.4 und 2.5 aufgeführten Arbeiten. In 2.4. wurden sogenannte Stent-Maps generiert, welche eine zweidimensionale Darstellung des TAVI-Stents erlauben. Verschiedene Parameter des Stents und der Anatomie wie z. B. Stent-Form, Radialkräfte als Heat-Map, Kalzifikationen und Anatomie der Aortenwurzel sind darin dargestellt. Von 32 Patienten wurde eine solche Stent-Map erstellt. Der Vorteil einer solchen Darstellung ist die komprimierte Darstellung vieler Informationen in einem Bild. Dadurch ist beispielsweise eine bessere Vergleichbarkeit zwischen vielen Patienten möglich und die Grundlage für weitere Projekte gegeben, in großem Umfang Muster zu analysieren, die z. B. für die Ausprägung paravalvulärer Lecks typisch sein könnten. Solche Muster könnten dann in computersimulierten Eingriffen identifiziert und daraufhin eine Änderung der Therapiestrategie in Betracht gezogen werden. Im Gegensatz zu der in dieser Studie verwendeten zweidimensionalen Darstellung wurde in 2.5 die aus CT-Daten rekonstruierte Deformation des Klappenprothesen-Stents verwendet, um Rückschlüsse auf die Radialkräfte des Stents in der Aortenwurzel zu ziehen. Bei 18 Patienten wurde eine solche Analyse durchgeführt. Es zeigte sich eine gute Korrelation zwischen am Stent auftretenden Maxima an Radialkräften und dem Vorhandensein von Kalk-Clustern in diesen Bereichen. Über die Deformation ließen sich für alle Stents die Radialkräfte berechnen. Dieser Ansatz kann als Grundlage für weitere Studien dienen, um ein besseres Verständnis der bei TAVI-Eingriffen wirksamen mechanischen Prozesse und deren Auswirkung auf das Ergebnis des Eingriffs zu erhalten. Ähnliche Ansätze wurden auch in anderen Studien zur Simulation von TAVI-Eingriffen verwendet. Sun und Kollegen untersuchten in einem Simulationsmodell die Auswirkung von elliptischen Deformationen der TAVI-Prothese⁵⁷. Sie konnten zeigen, dass bei einer stark elliptischen Prothese eine höhere Wahrscheinlichkeit für das Auftreten eines paravalvulären Lecks besteht als bei runden Prothesen. Dies wurde durch die Kombination von FEMs und *Computational Fluid Dynamics* simuliert. In dieser Studie wurde allerdings keine Validierung am Patienten durchgeführt. Wang und Kollegen beschreiben ein FEM zur Simulation der Interaktion zwischen Stent und umgebendem Gewebe während Transkatheter-Aortenklappenimplantationen⁵⁸. CT-Daten eines Patienten wurden zur 3D-

Modellierung der Aortenwurzel verwendet. An diesen Daten wurde, im Gegensatz zu der in 2.4 aufgeführten Studie, in welcher nur selbstexpandierende Prothesen verwendet wurden, die Implantation einer ballonexpandierenden Prothese simuliert. Es wurden also nicht nur die Eigenschaften des Stents mit in die Simulation einbezogen, sondern auch das Verhalten der Prothese während der Dilatation durch den Ballon. Verschiedene Parameter wie z. B. die Kontaktkräfte zwischen Stent und Aortenwurzel und die Stresskräfte am Stent wurden simuliert. Es zeigten sich Maxima der Kräfte im Bereich der Kalzifikationen, wie es auch in der unter 2.4 aufgeführten Arbeit gezeigt werden konnte. Schlussfolgerung war, dass die Simulation eine verbesserte Planung von TAVI-Eingriffen ermöglicht. Auch Sturla und Kollegen beschäftigten sich mit verschiedenen Formen der Kalzifikation der Aortenklappentaschen im Zusammenhang mit der Simulation von TAVI-Prozeduren mit ballonexpandierenden Prothesen⁵⁹. Sie simulierten TAVI-Implantationen in drei Aortenwurzeln mit unterschiedlich ausgeprägter Kalzifikation. Auch sie konnten zeigen, dass im Bereich von Kalzifikationen die vom Stent ausgeübten Kräfte auf die Aortenwurzel sehr hoch sind. Außerdem zeigte sich ein unterschiedliches Risiko bzgl. des Auftretens eines paravalvulären Lecks bei verschiedenen Kalzifikationsmustern. Die Limitation dieser Studie lag wiederum darin, dass im Gegensatz zu der unter 2.4 aufgeführten Studie keine Patientendaten verwendet wurden, sondern die Aortenwurzel eine idealisierte Form hatte und nicht aus realen CT-Daten rekonstruiert wurde. Es ist jedoch hervorzuheben, dass zahlreiche mechanische Parameter simuliert werden konnten, die Auswirkungen auf das Ergebnis der Prozedur haben können. Dies erweitert das Spektrum an Methoden der Simulation von TAVI-Prozeduren. Morganti und Kollegen verwendeten in zwei Fällen Patientendaten und simulierten die Implantation einer ballonexpandierenden Prothese⁶⁰. In dieser Studie wurde die komplette Implantation der Klappe in die rekonstruierten Aortenwurzeln simuliert. Es zeigte sich ebenfalls wie in den vorher beschriebenen Studien und wie in der unter 2.4 aufgeführten Studie Maxima an Kontaktkräften zwischen Stent und Aortenwand im Bereich von Kalzifikationen der Aortenwurzel. Es wurden außerdem weitere Parameter wie Änderung von Form des Stents in der Aortenwurzel und Risiko von Auftreten paravalvulärer Lecks erhoben. Um die Simulationsergebnisse zu validieren wurden die Ergebnisse mit klinischen Untersuchungen verglichen, welche im Rahmen der Interventionen durchgeführt wurden. Es zeigten sich gute Übereinstimmungen zwischen den simulierten Werten und den in vivo gemessenen Daten. In der Diskussion wird als Limitation aufgeführt, dass die Ergebnisse der Simulation, welche unter Verwendung von präoperativen Bilddaten durchgeföhrt werden, idealerweise durch postoperative CT-Bilddaten validiert werden sollten und nicht durch echokardiographische Daten wie in ihrer Studie. In der unter 2.5 aufgeführten Studie wurden postoperative Bilddaten

nach TAVI verwendet. Es wurden keine Simulationsergebnisse validiert, jedoch wurden Methoden entwickelt, um den Stent aus den postoperativen Bilddaten zu extrahieren, was insbesondere im Bereich starker Kalzifikationen schwierig ist, da die Dichtewerte von Stent und Kalzifikationen im CT sehr ähnlich sind. Es konnte gezeigt werden, dass die Methode zur automatischen Extraktion des Stents funktioniert inklusive der Separation von Kalzifikationen. Dies wurde validiert, indem die Ergebnisse mit den Ergebnissen einer manuellen Stent-Extraktion durch Probanden verglichen wurde. Es zeigte sich eine sehr gute Übereinstimmung der identifizierten Stent-Landmarken. Anhand der Deformation des Stents gelang es, die Radialkräfte zwischen Stent und Aortenwand zu berechnen. Es wurde in dieser Studie im Gegensatz zu⁵⁸⁻⁶⁰ die selbstexpandierende Corevalve-Prothese untersucht. Die Expansion des Stents beruht auf der Eigenschaft des Nitinols, nach Deformation in die ursprüngliche Form zurück zu kehren. Dies unterscheidet sich mechanisch grundsätzlich von der Expansion durch einen Ballon. Außerdem wurde eine deutlich höhere Anzahl an Patienten als in anderen Studien untersucht. Insgesamt wurden 18 Patienten analysiert. Somit wurde durch diese Studie das Spektrum an Simulationen von TAVI-Prozeduren erweitert. Durch die höhere Anzahl an Patienten sind die Ergebnisse klinisch relevanter da gezeigt werden konnte, dass die Methode auch reproduzierbar angewendet werden kann. Limitierend gegenüber den anderen Studien ist die alleinige Simulation des Stent-Verhaltens. Das Verhalten der Prothesenklappe wurde vernachlässigt, da die Komplikationen paravalvuläres Leck und Schrittmacher-Neuimplantation eher auf das Stent-Verhalten und nicht auf die Klappe zurückzuführen sind.

3.2 Verwendung der transösophagealen Echokardiographie bei bildfusionierenden Techniken und zur Entwicklung neuer, patientenspezifischer Therapieverfahren

Die unter 2.6 aufgeführte Studie untersucht die sichere Anwendung der EchoNavigator-Software während MitraClip-Eingriffen. Bei 21 Patienten konnte diese gezeigt werden, ebenfalls ein Trend zur Reduktion der Strahlendosis insbesondere bei komplexeren Eingriffen im Vergleich zur Durchführung der Mitraclip-Implantation ohne die Software. Dies ist die erste und einzige Studie, welche dies zeigen konnte. Balzer und Kollegen beschrieben ihre Erfahrungen mit der EchoNavigator-Software im Zusammenhang mit MitraClip-Implantationen, beschrieben jedoch nur die Nützlichkeit der Anwendung ohne Parameter zu messen, welche die Vorteile messbar machen⁶¹. In anderen Studien wurde die Anwendung der EchoNavigator-Software im Zusammenhang mit der interventionellen Behandlung von kongenitalen Vitien und Verschluss des linken Vorhoftrohrs untersucht. Gafoor und Kollegen beschreiben die Anwendung der EchoNavigator-Software während der kathetergestützten Implantation von Verschlussystemen des linken Vorhoftrohrs⁶². Allerdings handelt es sich bei dieser Publikation auch um eine Beschreibung der Anwendung ohne Erhebung von Daten. Jungen und Kollegen untersuchten die Anwendung der EchoNavigator-Software während der Implantation eines Amplatzer Devices zum Verschluss des linken Vorhoftrohrs und verglichen die Ergebnisse mit Fällen, bei denen die EchoNavigator-Software nicht verwendet wurde⁶³. Es konnte gezeigt werden, dass sich die angewendete Strahlendosis um mehr als die Hälfte reduzierte. Die Eingriffszeit an sich verlängerte sich nicht. Somit konnte auch in dieser Studie der Nutzen der Software gezeigt werden. Jone und Kollegen untersuchten die Anwendung der EchoNavigator-Software während der Behandlung von angeborenen atrioseptalen Defekten bei Kindern⁶⁴. Auch in dieser Studie konnte eine signifikante Reduktion der Strahlendosis bei gleicher Prozedurlänge gezeigt werden. Eine Beurteilung durch die Anwendung fiel zu 81% mit „überlegen“ aus. Nur 19% bewerteten die Anwendung mit „kein zusätzlicher Nutzen“.

Eine andere Form der Bildfusion ist das sogenannte *Overlay* von aus CT-Daten oder Rotationsangiographien rekonstruierten anatomischen Strukturen wie zum Beispiel der Aortenwurzel, die dann während der Prozedur über das Fluoroskopiebild gelegt werden^{65,66}. Eine Limitation dieses Verfahrens ist die statische Qualität von CT-Daten im Gegensatz zur bewegten Bildgebung in der Fluoroskopie. Erstens muss eine korrekte Überlagerung der Bilddaten stattfinden, das heißt, es muss für beide Bilddatensätze ein gemeinsames Koordinatensystem definiert werden. Zweitens muss eine Bewegungskompensation gewährleistet sein, so dass die

Überlagerung sich entsprechend der veränderten Positionen der anatomischen Strukturen während des Herzzyklus entsprechend mit bewegt. Dies ist aktuell noch nicht gut gelöst. Es gibt jedoch verschiedene Ansätze, welche bestimmte Strukturen als Fixpunkte definieren und dann entsprechend der Bewegung dieser Fixpunkte die Position des überlagerten Bildes anpassen. Hier ist allerdings noch Raum für weitere Verbesserungen. In einer Studie von van Miegham und Kollegen wurde die Fusionierung von CT-Bildern und Fluoroskopie beschrieben⁴⁴. In präoperativ angefertigten CTs wurden mit einer speziell dafür entwickelten Software spezifische Landmarken der geplanten Intervention markiert und in einer Simulation der Angiographie dargestellt. Diese Simulation wurde dann während der Implantation verwendet, um sich in der live-Fluoroskopie zu orientieren. Auch dies stellte sich als hilfreich für die Therapiedurchführung heraus.

Ein wichtiger Bestandteil der Entwicklung patientenspezifischer Therapieverfahren ist die Entwicklung und Testung im Großtiermodell. Alle neuen Therapieformen wie z. B. neu entwickelte Herzklappenprothesen müssen zunächst im Großtiermodell getestet werden, um die sichere Anwendbarkeit nachzuweisen. Häufig wird das Schwein hierfür verwendet, da die Anatomie und Physiologie des Menschen sehr ähnlich ist^{67,68}. Wie schon in den oben aufgeführten Publikationen herausgestellt wurde ist die Bildgebung bei minimalinvasiven und kathetergestützten Verfahren essentiell. Auch in der Entwicklung neuer Therapieformen müssen in den präklinischen Untersuchungen die bildgebenden Verfahren angewendet werden, welche dann auch später bei der humanen Implantation verwendet werden. Die TEE ist häufig wichtiger Bestandteil der Prozeduren. Allerdings gibt es zur TEE im Schwein nur wenige Untersuchungen. Daher wurde in der unter 2.7 aufgeführten Studie eine Standard-TEE-Untersuchung im Schwein beschrieben und Standardwerte präsentiert. Bei 20 Schweinen wurden vor der Durchführung des eigentlichen Experiments systematisch TEEs durchgeführt und Standardwerte entsprechend eines Studienprotokolls erhoben. Es zeigte sich, dass sowohl 2D- als auch 3D-Darstellungen aller Herzklappen und weiterer relevanter Strukturen möglich sind und somit die TEE als Standarduntersuchungsmethode bei präklinischen Versuchen verwendet werden kann. Bisher sind nur wenige Studien zur TEE im Schwein erschienen. Ren und Kollegen beschrieben ihre Methode der TEE und der intrakardialen Echokardiographie beim Schwein und ebenfalls Standardwerte⁶⁹. Diese Studie ist schon 1997 publiziert worden. 3D-TEE war zu dieser Zeit noch nicht verfügbar, heute gehört sie zum Standard jeder echokardiographischen Untersuchung. Ansonsten zeigten sich gute Übereinstimmungen der gemessenen Werte mit unserer Studie. Allerdings wurden beispielsweise die Dimensionen der Aortenklappe und der Mitralklappe von

Ren und Kollegen nicht beschrieben. Diese Werte sind aber heutzutage bei der steigenden Zahl an neuen Therapieformen zur Behandlung von Aortenklappen und Mitralklappenerkrankungen sehr wichtig. Hutchinson und Kollegen verglichen die intrakardiale Echokardiographie, englisch *Intracardiac Echocardiography* (ICE) und die TEE im Schwein bei kathetergestütztem Verschluss des linken Vorhofohrs⁷⁰. Es konnte gezeigt werden, dass ICE und TEE gleichwertig in der Identifikation eines Thrombus im linken Vorhofohr vor einem solchen Eingriff sind. Die Untersuchung wurde bei 5 Schweinen durchgeführt. Abgesehen von der niedrigeren Anzahl an Tieren wurde auch nur fokussiert die Darstellung des linken Vorhofohrs untersucht. Weitere Daten wurden nicht erhoben. Auch zur transthorakalen Echokardiographie ist eine schematische Untersuchungstechnik beschrieben⁷¹. Auch hier konnte gezeigt werden, dass die Darstellung gewisser Strukturen möglich ist. In der unter 2.7 aufgeführten Studie gelang die umfangreichere Darstellung der kardialen Strukturen durch die TEE, die demnach zur kardialen Bildgebung im Schwein besser geeignet zu sein scheint. In den letzten Jahren bestätigte sich der Stellenwert der TEE als bildgebende Standardmethode bei präklinischen Untersuchungen. In mehrere Studien, in welchen die kathetergestützte Implantation von Mitralklappen- und Aortenklappenprothesen präklinisch untersucht wurden, ist die TEE als wichtige bildgebende Modalität während der Implantation beschrieben⁷²⁻⁷⁴. Für diese und zukünftige Arbeiten kann die in der unter 2.7 aufgeführte standardisierte TEE-Untersuchungsmethode als Leitlinie genutzt werden.

4 Zusammenfassung

Für die Therapie von Erkrankungen der Mitralklappe und der Aortenklappe wurden in den letzten Jahren zahlreiche neue Therapieformen entwickelt. Nach wie vor ist der chirurgische Eingriff für die meisten Patienten der Goldstandard. Jedoch wurden insbesondere für Hochrisikopatienten neue, weniger invasive Therapieformen entwickelt. Minimalinvasive Operationstechniken und kathetergestützte Verfahren, welche ohne den Einsatz der Herz-Lungen-Maschine durchgeführt werden können, erweitern heute das Armamentarium an möglichen Interventionen. Für diese Therapieformen ist für die Planung und die Durchführung der Therapie eine hoch entwickelte Bildgebung essentiell, da häufig keine direkte Sicht auf das Operationsfeld möglich ist. Die CT und die Echokardiographie haben sich hierfür als wichtigste Modalität herausgestellt. Die hohe räumliche und zeitliche Auflösung dieser beiden Verfahren ermöglichen auch den Einsatz zur Weiterentwicklung hin zu patientenspezifischen Therapieansätzen und zur Simulation von Prozeduren.

Die Darstellung der Mitralklappe in der Computertomographie hat erst in den letzten Jahren an Relevanz gewonnen, vor allem im Zusammenhang mit kathetergestützten Therapieformen zur Behandlung von Mitralklappenerkrankungen. In einer Studie konnten wir den Nutzen der CT zur Planung der kathetergestützten Implantation eines Mitralklappenannuloplastiebandes zeigen. In einer weiteren Studie wurde die CT zur Modellierung und Produktion eines patientenspezifischen Mitralklappenannuloplastierings verwendet, welcher erfolgreich im Tiermodell implantiert werden konnte. Beide Studien zeigen die hohe Wertigkeit der CT bei der Darstellung der Mitralklappe und deren Verwendung zur Entwicklung von patientenspezifischen Therapien der Mitralklappenerkrankungen.

Im Bereich der Behandlung von Aortenklappenerkrankungen, insbesondere bei minimalinvasiven Therapieformen, ist die CT seit langer Zeit als Standardbildgebungsverfahren anerkannt. In 3 der in dieser Habilitationsschrift aufgeführten Studien wurde die CT zur Simulation und patientenspezifischen Planung von Transkatheter-Aortenklappeneingriffen verwendet. Es gelang zu zeigen, dass es möglich ist, die Daten zur Rekonstruktion und Modellierung relevanter anatomischer Strukturen zu verwenden. Insbesondere die Darstellung des Stents ist in postoperativen CTs durch das Vorhandensein von Verkalkungen schwierig. Es konnte eine Methode entwickelt werden, die eine exakte Rekonstruktion des Stents ermöglichte. Anhand der Deformation des extrahierten Stents konnten Rückschlüsse auf die mechanischen Interaktionen mit dem umgebenden Gewebe gewonnen werden. Dadurch entstanden nicht nur Erkenntnisse zur Mechanik von TAVI-Prozeduren, sondern auch die Identifikation von

Faktoren, welche das Auftreten von Komplikationen wie paravalvuläre Lecks und Schrittmacher-Neuimplantationen begünstigen könnten. Auch eine Anwendung zur patientenspezifischen Therapieplanung durch die Implantation von virtuellen Stents in aus CT-Daten rekonstruierten Aortenwurzelmodellen wurde entwickelt. Es konnte gezeigt werden, dass die Verwendung dieser Anwendung vorteilhaft bei der Therapieplanung sein kann und somit das Repertoire an vorhanden Planungsanwendungen erweitert.

Weitere Studien beschäftigen sich mit der Verwendung der transösophagealen Echokardiographie. In einer Studie wurde die Fusion von Echokardiographie und Fluoroskopie während MitraClip-Eingriffen als vorteilhaft identifiziert im Gegensatz zur isolierten Verwendung der jeweiligen Bildgebung. In einer anderen Studie wurde eine Standarduntersuchungsmethode zur transösophagealen Echokardiographie beim Schwein etabliert, um die Weiterentwicklung patientenspezifischer Therapieverfahren zu vereinfachen.

In allen Studien konnte gezeigt werden, dass Standardbildgebungsverfahren in der Entwicklung von patientenspezifischen Therapieformen und der Simulation von Therapien verwendet werden können. Die gewonnenen Erkenntnisse werden in Zukunft weiter an Relevanz gewinnen, da eine Ausweitung der Anwendung minimalinvasiver und kathetergestützter Verfahren auch auf Patienten mit mittlerem und niedrigem Operationsrisiko zu erwarten ist.

Die Weiterentwicklung und Ausweitung dieser Methoden wird das Ziel zukünftiger Studien sein.

5 Literatur

1. Iung B, Baron G, Butchart EG, Delahaye F, Gohlke-Bärwolf C, Levang OW, Tornos P, Vanoverschelde J-L, Vermeer F, Boersma E, Ravaud P, Vahanian A. A prospective survey of patients with valvular heart disease in Europe: The Euro Heart Survey on Valvular Heart Disease. *Eur Heart J.* 2003;24(13):1231-1243.
2. Nkomo VT, Gardin JM, Skelton TN, Gottdiener JS, et al. Burden of valvular heart diseases: a population-based study. *Lancet.* 2006;368(9540):1005-1011.
3. Freed LA, Levy D, Levine RA, Larson MG, Evans JC, Fuller DL, Lehman B, Benjamin EJ. Prevalence and clinical outcome of mitral-valve prolapse. *N Engl J Med.* 1999;341(1):1-7.
4. Smith CR, Leon MB, Mack MJ, Miller DC, Moses JW, Svensson LG, Tuzcu EM, Webb JG, Fontana GP, Makkar RR, Williams M, Dewey T, Kapadia S, Babaliaros V, Thourani VH, Corso P, Pichard AD, Bavaria JE, Herrmann HC, Akin JJ, Anderson WN, Wang D, Pocock SJ, PARTNER Trial Investigators. Transcatheter versus surgical aortic-valve replacement in high-risk patients. *N Engl J Med.* 2011;364(23):2187-2198.
5. Mack MJ, Leon MB, Smith CR, Miller DC, Moses JW, Tuzcu EM, Webb JG, Douglas PS, Anderson WN, Blackstone EH, Kodali SK, Makkar RR, Fontana GP, Kapadia S, Bavaria J, Hahn RT, Thourani VH, Babaliaros V, Pichard A, Herrmann HC, Brown DL, Williams M, Akin J, Davidson MJ, Svensson LG, PARTNER 1 trial investigators. 5-year outcomes of transcatheter aortic valve replacement or surgical aortic valve replacement for high surgical risk patients with aortic stenosis (PARTNER 1): a randomised controlled trial. *Lancet.* 2015;385(9986):2477-2484.
6. Leon MB, Smith CR, Mack MJ, Makkar RR, Svensson LG, Kodali SK, Thourani VH, Tuzcu EM, Miller DC, Herrmann HC, Doshi D, Cohen DJ, Pichard AD, Kapadia S, Dewey T, Babaliaros V, Szeto WY, Williams MR, Kereiakes D, Zajarias A, Greason KL, Whisenant BK, Hodson RW, Moses JW, Trento A, Brown DL, Fearon WF, Pibarot P, Hahn RT, Jaber WA, Anderson WN, Alu MC, Webb JG, PARTNER 2 Investigators. Transcatheter or Surgical Aortic-Valve Replacement in Intermediate-Risk Patients. *N Engl J Med.* 2016;374(17):1609-1620.
7. Authors/Task Force Members, Alfieri O, Andreotti F, Antunes MJ, Barón-Esquivias G, Baumgartner H, Borger MA, Carrel TP, De Bonis M, Evangelista A, Falk V, Iung B, Lancellotti P, Pierard L, Price S, Schäfers H-J, Schuler G, Stepinska J, Swedberg K, Takkenberg J, Oppell Von UO, Zamorano JL, Zembala M, ESC Committee for Practice Guidelines (CPG), Bax JJ, Ceconi C, Dean V, Deaton C, Fagard R, Funck-Brentano C, Hasdai D, Hoes A, Kirchhof P, Knuuti J, Kolh P, McDonagh T, Moulin C, Reiner Z, Sechtem U, Sirnes PA, Tendera M, Torbicki A, Vahanian A, Windecker S, Document Reviewers:, Popescu BA, Segesser von L, Badano LP, Bunc M, Claeys MJ, Drinkovic N, Filippatos G, Habib G, Kappetein AP, Kassab R, Lip GYH, Moat N, Nickenig G, Otto CM, Pepper J, Piazza N, Pieper PG, Rosenhek R, Shuka N, Schwammenthal E, Schwitter J, Mas PT, Trindade PT, Walther T. Guidelines on the management of valvular heart disease (version 2012): The Joint Task Force on the Management of Valvular Heart Disease of the European Society of Cardiology (ESC) and the European Association for Cardio-Thoracic Surgery (EACTS). *Eur Heart J.* 2012;33(19):2451-2496.

8. Sündermann SH, Sromicki J, Rodriguez Cetina Biefer H, Seifert B, Holubec T, Falk V, Jacobs S. Mitral valve surgery: right lateral minithoracotomy or sternotomy? A systematic review and meta-analysis. *J Thorac Cardiovasc Surg.* 2014;148(5):1989–1995.
9. Feldman T, Kar S, Elmariah S, Smart SC, Trento A, Siegel RJ, Apruzzese P, Fail P, Rinaldi MJ, Smalling RW, Hermiller JB, Heimansohn D, Gray WA, Grayburn PA, Mack MJ, Lim DS, Ailawadi G, Herrmann HC, Acker MA, Silvestry FE, Foster E, Wang A, Glower DD, Mauri L, EVEREST II Investigators. Randomized Comparison of Percutaneous Repair and Surgery for Mitral Regurgitation: 5-Year Results of EVEREST II. *J Am Coll Cardiol.* 2015;66(25):2844-2854.
10. Maisano F, Alfieri O, Banai S, Buchbinder M, Colombo A, Falk V, Feldman T, Franzen O, Herrmann H, Kar S, Kuck KH, Lutter G, Mack M, Nickenig G, Piazza N, Reisman M, Ruiz CE, Schofer J, Søndergaard L, Stone GW, Taramasso M, Thomas M, Vahanian A, Webb J, Windecker S, Leon MB. The future of transcatheter mitral valve interventions: competitive or complementary role of repair vs. replacement? *Eur Heart J.* 2015;36(26):1651-1659.
11. Kalender WA. *Computertomographie*. 2. überarb. u. erw. Aufl. Erlangen: Publicis, 2006.
12. Sagel SS, Weiss ES, Gillard RG, Hounsfield GN, Jost GT, Stanley RJ, Ter-Pogossian MM. Gated computed tomography of the human heart. *Invest Radiol.* 1977;12(6):563-566.
13. Harell GS, Guthaner DF, Breiman RS, Morehouse CC, Seppi EJ, Marshall WH, Wexler L. Stop-action cardiac computed tomography. *Radiology.* 1977;123(2):515-517.
14. Guthaner DF, Wexler L, Harell G. CT demonstration of cardiac structures. *AJR Am J Roentgenol.* 1979;133(1):75-81.
15. Stoliński J, Plicner D, Grudzień G, Kruszec P, Fijorek K, Musiał R, Andres J. Computed Tomography Helps to Plan Minimally Invasive Aortic Valve Replacement Operations. *Ann Thorac Surg.* 2016;101(5):1745-1752.
16. Heuts S, Maessen JG, Sardari Nia P. Preoperative planning of left-sided valve surgery with 3D computed tomography reconstruction models: sternotomy or a minimally invasive approach? *Interact Cardiovasc Thorac Surg.* 2016;22(5):587-593.
17. Plass A, Scheffel H, Alkadhi H, Kaufmann P, Genoni M, Falk V, Grünenfelder J. Aortic Valve Replacement Through a Minimally Invasive Approach: Preoperative Planning, Surgical Technique, and Outcome. *Ann Thorac Surg.* 2009;88(6):1851-1856.
18. Achenbach S, Delgado V, Hausleiter J, Schoenhagen P, Min JK, Leipsic JA. SCCT expert consensus document on computed tomography imaging before transcatheter aortic valve implantation (TAVI)/transcatheter aortic valve replacement (TAVR). *J Cardiovasc Comput Tomogr.* 2012;6(6):366-380.
19. Hell M, Marwan M, Gaede L, Achenbach S. Software innovations in computed tomography for structural heart disease interventions. *EuroIntervention.* 2016;12(X):X68-X74.

20. Kempfert J, Van Linden A, Lehmkuhl L, Rastan AJ, Holzhey D, Blumenstein J, Mohr FW, Walther T. Aortic annulus sizing: echocardiographic versus computed tomography derived measurements in comparison with direct surgical sizing. *Eur J Cardiothorac Surg*. 2012;42(4):627-633.
21. Lehmkuhl L, Foldyna B, Haensig M, Aspern von K, Lücke C, Andres C, Grothoff M, Riese F, Nitzsche S, Holzhey D, Linke A, Mohr FW, Gutberlet M. Role of Preprocedural Computed Tomography in Transcatheter Aortic Valve Implantation. *Rofo*. 2013;184(10):941-949.
22. Foldyna B, Hänsig M, Lücke C, Holzhey D, Andres C, Grothoff M, Linke A, Mohr FW, Gutberlet M, Lehmkuhl L. Access path angle in transapical aortic valve replacement: risk factor for paravalvular leakage. *Ann Thorac Surg*. 2014;98(5):1572-1578.
23. Authors/Task Force Members, Vahanian A, Alfieri O, Andreotti F, Antunes MJ, Baron-Esquivas G, Borger MA, Carrel TP, De Bonis M, Evangelista A, Falk V, Iung B, Lancellotti P, Pierard L, Price S, Schafers HJ, Schuler G, Stepinska J, Swedberg K, Takkenberg J, Oppell von UO, Windecker S, Zamorano JL, Zembala M, ESC Committee for Practice Guidelines (CPG), Bax JJ, Baumgartner H, Ceconi C, Dean V, Deaton C, Fagard R, Funck-Brentano C, Hasdai D, Hoes A, Kirchhof P, Knuuti J, Kolh P, McDonagh T, Moulin C, Reiner Z, Sechtem U, Sirnes PA, Tendera M, Torbicki A, Document Reviewers:, Popescu BA, Segesser Von L, Badano LP, Bunc M, Claeys MJ, Drinkovic N, Filippatos G, Habib G, Kappetein AP, Kassab R, Lip GYH, Moat N, Nickenig G, Otto CM, Pepper J, Piazza N, Pieper PG, Rosenhek R, Shuka N, Schwammthal E, Schwitter J, Mas PT, Trindade PT, Walther T. Guidelines on the management of valvular heart disease (version 2012): The Joint Task Force on the Management of Valvular Heart Disease of the European Society of Cardiology (ESC) and the European Association for Cardio-Thoracic Surgery (EACTS). *Eur J Cardiothorac Surg*. 2012;42(4):S1-S44.
24. Rosu C, Bouchard D, Pellerin M, Lebon J-S, Jeanmart H. Preoperative vascular imaging for predicting intraoperative modification of peripheral arterial cannulation during minimally invasive mitral valve surgery. *Innovations (Phila)*. 2015;10(1):39-43.
25. Manenti A, Giuliani E, Colasanto D. Computed tomography AIDS minimally invasive mitral valve surgery. *Tex Heart Inst J*. 2013;40(2):211.
26. Thériault-Lauzier P, Mylotte D, Dorfmeister M, Spaziano M, Andalib A, Mamane S, Chetrit M, Blanke P, Cecere R, Buithieu J, Martucci G, Tchetche D, Modine T, van Mieghem N, Lange R, Windecker S, Bilodeau L, Leipsic J, Piazza N. Quantitative multi-slice computed tomography assessment of the mitral valvular complex for transcatheter mitral valve interventions part 1: systematic measurement methodology and inter-observer variability. *EuroIntervention*. 2016;12(8):e1011-e1020.
27. Thériault-Lauzier PP, Dorfmeister M, Mylotte D, Andalib A, Spaziano M, Blanke P, Martucci G, Lange R, Leipsic J, Bilodeau L, Piazza N. Quantitative multi-slice computed tomography assessment of the mitral valvular complex for transcatheter mitral valve interventions part 2: geometrical measurements in patients with functional mitral regurgitation. *EuroIntervention*. 2016;12(8):e1021-e1030.

28. Blanke P, Dvir D, Cheung A, Ye J, Levine RA, Precious B, Berger A, Stub D, Hague C, Murphy D, Thompson C, Munt B, Moss R, Boone R, Wood D, Pache G, Webb J, Leipsic J. A simplified D-shaped model of the mitral annulus to facilitate CT-based sizing before transcatheter mitral valve implantation. *J Cardiovasc Comput Tomogr.* 2014;8(6):459-467.
29. Wang H, Hanna JM, Ganapathi A, Keenan JE, Hurwitz LM, Vavalle JP, Kiefer TL, Wang A, Harrison JK, Hughes GC. Comparison of aortic annulus size by transesophageal echocardiography and computed tomography angiography with direct surgical measurement. *Am J Cardiol* 2015;115(11):1568-1573.
30. Debonnaire P, Delgado V, Bax JJ, Marsan NA. Tools & Techniques - Clinical: 3D transoesophageal echocardiography for selecting and guiding in percutaneous mitral valve repair using MitraClip®. *EuroIntervention.* 2014;10(7):884-886.
31. Capelli C, Bosi GM, Cerri E, Nordmeyer J, Odenwald T, Bonhoeffer P, Migliavacca F, Taylor AM, Schievano S. Patient-specific simulations of transcatheter aortic valve stent implantation. *Med Biol Eng Comput.* 2012;50(2):183-192.
32. Sündermann SH, Gessat M, Cesarovic N, Frauenfelder T, Biaggi P, Bettex D, Falk V, Jacobs S. Implantation of personalized, biocompatible mitral annuloplasty rings: feasibility study in an animal model. *Interact Cardiovasc Thorac Surg.* 2013;16(4):417-422.
33. Sündermann SH, Gordic S, Manka R, Cesarovic N, Falk V, Maisano F, Alkadhi H. Computed tomography for planning and postoperative imaging of transvenous mitral annuloplasty: first experience in an animal model. *Int J Cardiovasc Imaging.* 2015;31(1):135-142.
34. Maisano F, Vanermen H, Seeburger J, Mack M, Falk V, Denti P, Taramasso M, Alfieri O. Direct access transcatheter mitral annuloplasty with a sutureless and adjustable device: preclinical experience. *Eur J Cardiothorac Surg.* April 2012.
35. Sündermann SH, Gessat M, Maier W, Kempfert J, Frauenfelder T, Nguyen TDL, Maisano F, Falk V. Simulated Prosthesis Overlay for Patient-Specific Planning of Transcatheter Aortic Valve Implantation Procedures. *Innovations (Phila).* 2015;10(5):314-322.
36. Born S, Sündermann SH, Russ C, Hopf R, Ruiz CE, Falk V, Gessat M. Stent Maps – Comparative Visualization for the Prediction of Adverse Events of Transcatheter Aortic Valve Implantations. *IEEE Trans Vis Comput Graph.* 2014;20(12):2704-2713.
37. Gessat M, Hopf R, Pollok T, Russ C, Frauenfelder T, Sündermann SH, Hirsch S, Mazza E, Székely G, Falk V. Image-based mechanical analysis of stent deformation: concept and exemplary implementation for aortic valve stents. *IEEE Trans Biomed Eng.* 2014;61(1):4-15.
38. Sündermann SH, Biaggi P, Grünenfelder J, Gessat M, Felix C, Bettex D, Falk V, Corti R. Safety and feasibility of novel technology fusing echocardiography and fluoroscopy images during MitraClip interventions. *EuroIntervention.* 2014;9(10):1210-1216.
39. Sündermann SH, Cesarovic N, Falk V, Bettex D. Two- and three-dimensional transoesophageal echocardiography in large swine used as model for transcatheter heart valve therapies: standard planes and values. *Interact Cardiovasc Thorac Surg.* 2016;22(5):580-586.

40. Díaz Lantada A, Valle-Fernández RD, Morgado PL, Muñoz-García J, Muñoz Sanz JL, Munoz-Guijosa JM, Otero JE. Development of personalized annuloplasty rings: combination of CT images and CAD-CAM tools. *Ann Biomed Eng.* 2010;38(2):280-290.
41. Khamooshian A, Buijsrogge MP, de Heer F, Gründeman PF. Mitral Valve Annuloplasty Rings. *Innovations (Phila)* 2014;9(6):399-415.
42. Willmann JK, Kobza R, Roos JE, Lachat M, Jenni R, Hilfiker PR, Lüscher TF, Marincek B, Weishaupt D. ECG-gated multi-detector row CT for assessment of mitral valve disease: initial experience. *Eur Radiol.* 2002;12(11):2662-2669.
43. Messika-Zeitoun D, Serfaty J-M, Laissy J-P, Berhili M, Brochet E, Iung B, Vahanian A. Assessment of the mitral valve area in patients with mitral stenosis by multislice computed tomography. *J Am Coll Cardiol.* 2006;48(2):411-413.
44. van Mieghem NM, Rodríguez-Olivares R, Ren BC, van Gils L, Maugenest A, Geleijnse ML, Budde RPJ, Vogelaar J, Verstraeten L, de Jaegere PP. Computed tomography optimised fluoroscopy guidance for transcatheter mitral therapies. *EuroIntervention.* 2016;11(12):1428-1431.
45. Debonnaire P, Palmen M, Marsan NA, Delgado V. Contemporary imaging of normal mitral valve anatomy and function. *Curr Opin Cardiol.* 2012;27(5):455-464.
46. Chheda S. Evaluation of the mitral and aortic valves with cardiac CT angiography. *J Thorac Imaging.* 2010;25(1):76-85.
47. Ghersin N, Abadi S, Sabbag A, Lamash Y, Anderson RH, Wolfson H, Lessick J. The three-dimensional geometric relationship between the mitral valvar annulus and the coronary arteries as seen from the perspective of the cardiac surgeon using cardiac computed tomography. *Eur J Cardiothorac Surg.* 2013;44(6):1123-1130.
48. Morris MF, Maleszewski JJ, Suri RM, Burkhardt HM, Foley TA, Bonnichsen CR, Anavekar NS, Young PM, Williamson EE, Glockner JF, Araoz PA. CT and MR imaging of the mitral valve: radiologic-pathologic correlation. *Radiographics.* 2010;30(6):1603-1620.
49. Gordic S, Nguyen-Kim TDL, Manka R, Sündermann S, Frauenfelder T, Maisano F, Falk V, Alkadhi H. Sizing the mitral annulus in healthy subjects and patients with mitral regurgitation: 2D versus 3D measurements from cardiac CT. *Int J Cardiovasc Imaging.* 2014;30(2):389-398.
50. Ghosh N, Al-Shehri H, Chan K, Mesana T, Chan V, Chen L, Yam Y, Chow BJW. Characterization of mitral valve prolapse with cardiac computed tomography: comparison to echocardiographic and intraoperative findings. *Int J Cardiovasc Imaging.* 2012;28(4):855-863.
51. Maisano F, Taramasso M, Nickenig G, Hammerstingl C, Vahanian A, Messika-Zeitoun D, Baldus S, Huntgeburth M, Alfieri O, Colombo A, La Canna G, Agricola E, Zuber M, Tanner FC, Topilsky Y, Kreidel F, Kuck K-H. Cardioband, a transcatheter surgical-like direct mitral valve annuloplasty system: early results of the feasibility trial. *Eur Heart J.* 2016;37(10):817-825.

52. Gopal A, Budoff MJ, Shavelle DM. Use of cardiac computed tomography prior to percutaneous coronary sinus device placement for the treatment of mitral regurgitation. *JACC Cardiovasc Interv.* 2011;4(5):593; author reply 593–4.
53. Tops LF, Van de Veire NR, Schuijf JD, de Roos A, van der Wall EE, Schalij MJ, Bax JJ. Noninvasive evaluation of coronary sinus anatomy and its relation to the mitral valve annulus: implications for percutaneous mitral annuloplasty. *Circulation.* 2007;115(11):1426-1432.
54. Choure AJ, Garcia MJ, Hesse B, Sevensema M, Maly G, Greenberg NL, Borzi L, Ellis S, Tuzcu EM, Kapadia SR. In vivo analysis of the anatomical relationship of coronary sinus to mitral annulus and left circumflex coronary artery using cardiac multidetector computed tomography: implications for percutaneous coronary sinus mitral annuloplasty. *J Am Coll Cardiol.* 2006;48(10):1938-1945.
55. Blanke P, Dvir D, Cheung A, Levine RA, Thompson C, Webb JG, Leipsic J. Mitral Annular Evaluation With CT in the Context of Transcatheter Mitral Valve Replacement. *JACC Cardiovascular Imaging.* 2015;8(5):612-615.
56. Votta E, Le TB, Stevanella M, Fusini L, Caiani EG, Redaelli A, Sotiropoulos F. Toward patient-specific simulations of cardiac valves: state-of-the-art and future directions. *J Biomech.* 2013;46(2):217-228.
57. Sun W, Li K, Sirois E. Simulated elliptical bioprosthetic valve deformation Implications for asymmetric transcatheter valve deployment. *J of Biomech.* 2010;43(16):3085-3090.
58. Wang Q, Sirois E, Sun W. Patient-specific modeling of biomechanical interaction in transcatheter aortic valve deployment. *Biomech.* 2012;45(11):1965-1971.
59. Sturla F, Ronzoni M, Vitali M, Dimasi A, Vismara R, Preston-Maher G, Burriesci G, Votta E, Redaelli A. Impact of different aortic valve calcification patterns on the outcome of transcatheter aortic valve implantation: A finite element study. *J Biomech.* 2016;49(12):2520-2530.
60. Morganti S, Conti M, Aiello M, Valentini A, Mazzola A, Reali A, Auricchio F. Simulation of transcatheter aortic valve implantation through patient-specific finite element analysis: Two clinical cases. *J Biomech.* 2014;47(11):2547-2555.
61. Balzer J, Zeus T, Hellhammer K, Veulemans V, Eschenhagen S, Kehmeier E, Meyer C, Rassaf T, Kelm M. Initial clinical experience using the EchoNavigator(®)-system during structural heart disease interventions. *World J Cardiol.* 2015;7(9):562-570.
62. Gafoor S, Schulz P, Heuer L, Matic P, Franke J, Bertog S, Reinartz M, Vaskelyte L, Hofmann I, Sievert H. Use of EchoNavigator, a novel echocardiography-fluoroscopy overlay system, for transseptal puncture and left atrial appendage occlusion. *J Interv Cardiol.* 2015;28(2):215-217.
63. Jungen C, Zeus T, Balzer J, Eickholt C, Petersen M, Kehmeier E, Veulemans V, Kelm M, Willems S, Meyer C. Left Atrial Appendage Closure Guided by Integrated Echocardiography and Fluoroscopy Imaging Reduces Radiation Exposure. Andò G, ed. *PLoS ONE.* 2015;10(10):e0140386.

64. Jone P-N, Ross MM, Bracken JA, Mulvahill MJ, Di Maria MV, Fagan TE. Feasibility and Safety of Using a Fused Echocardiography/Fluoroscopy Imaging System in Patients with Congenital Heart Disease. *J Am Soc Echocardiogr.* 2016;29(6):513-521.
65. Kempfert J, Noettling A, John M, Rastan A, Mohr FW, Walther T. Automatically segmented DynaCT: enhanced imaging during transcatheter aortic valve implantation. *J Am Coll Cardiol.* 2011;58(25):e211.
66. Vaitkus PT, Wang DD, Greenbaum A, Guerrero M, O'Neill W. Assessment of a novel software tool in the selection of aortic valve prosthesis size for transcatheter aortic valve replacement. *J Invasive Cardiol.* 2014;26(7):328-332.
67. Gallegos RP, Nockel PJ, Rivard AL, Bianco RW. The current state of in-vivo pre-clinical animal models for heart valve evaluation. *J Heart Valve Dis.* 2005;14(3):423-432.
68. Suzuki Y, Yeung AC, Ikeno F. The representative porcine model for human cardiovascular disease. *J Biomed Biotechnol.* 2011;2011(3728):195483–10.
69. Ren JF, Schwartzman D, Lighty GW, Menz V, Michele JJ, Li KS, Dillon SM, Marchlinski FE, Segal BL. Multiplane Transesophageal and Intracardiac Echocardiography in Large Swine: Imaging Technique, Normal Values, and Research Applications. *Echocardiography.* 1997;14(2):135-148.
70. Hutchinson MD, Jacobson JT, Michele JJ, Silvestry FE, Callans DJ. A comparison of intracardiac and transesophageal echocardiography to detect left atrial appendage thrombus in a swine model. *J Interv Card Electrophysiol.* 2010;27(1):3-7.
71. Kerut EK, Valina CM, Luka T, Pinkernell K, Delafontaine P, Alt EU. Technique and imaging for transthoracic echocardiography of the laboratory pig. *Echocardiography.* 2004;21(5):439-442.
72. Pokorny S, Dai H, Bähr T, Huenges K, Marczynski-Bühlow M, Morlock MM, Cremer J, Lutter G. Transapical mitral valved stent implantation: comparison between circular and D-shaped design. *EuroIntervention.* 2014;10(3):372-380.
73. Wendt D, Pasa S, Kahlert P, Delaloye S, Al-Rashid F, Price V, Jánosi R-A, Borenstein N, Behr L, Konorza T, Erbel R, Jakob H, Thielmann M. A new self-expandable transcatheter aortic valve for transapical implantation: feasibility in acute and chronic animal experiments. *Scand Cardiovasc J.* 2013;47(3):145-153.
74. Banai S, Jolicœur EM, Schwartz M, Garceau P, Biner S, Tanguay JF, Cartier R, Verheyen S, White CJ, Edelman E. Tiara: a novel catheter-based mitral valve bioprosthesis: initial experiments and short-term pre-clinical results. *J Am Coll Cardiol.* 2012;60(15):1430-1431.

Anmerkung

Die in der Arbeit verwendeten Publikationen wurden mit freundlicher Genehmigung der Verlage veröffentlicht. Dies sind im Einzelnen:

- 2.1 Implantation of Personalized, Biocompatible Mitral Annuloplasty Rings: Feasibility Study in an Animal Model,
mit freundlicher Genehmigung von Oxford University Press.
- 2.2 Computed Tomography for Planning and Postoperative Imaging of Transvenous Mitral Annuloplasty: First Experience in an Animal Model,
mit freundlicher Genehmigung von Springer.
- 2.3 Simulated Prosthesis Overlay for Patient-Specific Planning of Transcatheter Aortic Valve Implantation Procedures,
mit freundlicher Genehmigung von Wolters Kluwer Health, Lippincott Williams & Wilkins.
- 2.4 Stent Maps – Comparative Visualization for the Prediction of Adverse Events of Transcatheter Aortic Valve Implantations,
mit freundlicher Genehmigung von IEEE.
- 2.5 Image-Based Mechanical Analysis of Stent Deformation: Concept and Exemplar Implementation for Aortic Valve Stents,
mit freundlicher Genehmigung von IEEE.
- 2.6 Safety and Feasibility of Novel Technology Fusing Echocardiography and Fluoroscopy Images during MitraClip Interventions,
mit freundlicher Genehmigung von Europa Digital & Publishing.
- 2.7 Two- and Three-Dimensional Transthoracic Echocardiography in large Swine used as Model for Transcatheter Heart Valve Therapies: Standard Planes and Values,
mit freundlicher Genehmigung von Oxford University Press.

6 Danksagung

Zuallererst möchte ich Herrn Professor Dr. med. Volkmar Falk, Ärztlicher Direktor des Deutschen Herzzentrums Berlin und Direktor der Klinik für Herz-, Thorax- und Gefäßchirurgie, herzlich danken. Fast ab Beginn meiner klinischen und wissenschaftlichen Laufbahn mein Chef und Mentor, erst in Zürich, dann in Berlin, hat er mich unermüdlich bei meiner klinischen Ausbildung und wissenschaftlichen Tätigkeit unterstützt und natürlich maßgeblich zu meiner Habilitation beigetragen. Danke Chef!

Danken möchte ich auch Herrn Professor Mohr, Direktor der Klinik für Herzchirurgie des Herzzentrums Leipzig, meinem ersten Chef. Er und die Kollegen in Leipzig haben mich vom Fach Herzchirurgie so überzeugt, dass ich dabeibleiben bin, obwohl ich eigentlich vorhatte, Kardiologe zu werden. Ich habe es nicht bereut.

Ein besonderer Dank gilt den Kolleginnen und Kollegen der Klinik für Herz- und Gefäßchirurgie des UniversitätsSpitals Zürich und den Kollegen der ETH Zürich. In der Zeit in Zürich ist ein Großteil der wissenschaftlichen Arbeiten entstanden, die zu dieser Habilitation geführt haben. Besonders hervorheben möchte ich an dieser Stelle meine ehemaligen Kollegen und immer noch Freunde Dr. med. Héctor Rodriguez und Prof. Dr. med. Max Emmert, PhD, die immer entscheidend zum Durchhalten und Weiterkommen beigetragen haben. Einen herzlichen Dank auch an Dr. Michael Gessat und Dr. Silvia Born, Ingenieure der ETH Zürich. Die Kooperation mit ihnen ist Basis meiner wissenschaftlichen Arbeit. Die Zusammenarbeit war großartig! Meinen besten Dank auch an PD Dr. med. vet. Niko Cesarovic, Veterinär und Workaholic am USZ. Auch diese Zusammenarbeit war und ist immer noch äußerst fruchtbar.

Vielen Dank natürlich auch an alle, die bei den Projekten mitgearbeitet haben und die mich in der Klinik unterstützt haben, in Leipzig, Zürich und jetzt auch in Berlin. Die Auflistung all dieser großartigen Kolleginnen und Kollegen würde den Rahmen dieser Danksagung völlig sprengen. Ich hoffe, jeder der gemeint ist, fühlt sich angesprochen!

Zuletzt und am meisten danke ich meiner Familie von ganzem Herzen – Meine Eltern, mein Bruder, meine Frau Claudia und inzwischen auch unser Sohn Henry, der kleine Sonnenschein, sind die Hauptmotivation hinter allem!

7 Erklärung

§ 4 Abs. 3 (k) der HabOMed der Charité

Hiermit erkläre ich, dass

- weder früher noch gleichzeitig ein Habilitationsverfahren durchgeführt oder angemeldet wurde,
- die vorgelegte Habilitationsschrift ohne fremde Hilfe verfasst, die beschriebenen Ergebnisse selbst gewonnen sowie die verwendeten Hilfsmittel, die Zusammenarbeit mit anderen Wissenschaftlern/Wissenschaftlerinnen und mit technischen Hilfskräften sowie die verwendete Literatur vollständig in der Habilitationsschrift angegeben wurden,
- mir die geltende Habilitationsordnung bekannt ist.

Ich erkläre ferner, dass mir die Satzung der Charité – Universitätsmedizin Berlin zur Sicherung Guter Wissenschaftlicher Praxis bekannt ist und ich mich zur Einhaltung dieser Satzung verpflichte.

.....
Datum

.....
Unterschrift